Numerical Simulation of Droplet Deformation Using Spectral Element Method

Yu Zheng [1]

Supervised by

Professor T.N. Phillips and Professor P.J. Bowen

September 27, 2007

[1]School of Engineering and School of Mathematics, Cardiff University, CF24 3AA, United Kingdom

ProQuest LLC
789 East Eisenhower Parkway
P.O. Box 1346
Ann Arbor, MI 48106-1346

Form: PGR_Submission_200701

NOTICE OF SUBMISSION OF THESIS FORM: POSTGRADUATE RESEARCH

APPENDIX 1:
Specimen layout for Thesis Summary and Declaration/Statements page to be included in a Thesis

DECLARATION

This work has not previously been accepted in substance for any degree and is not concurrently submitted in candidature for any degree.

Signed ..... (candidate) Date ...Sept. 28, 2007

STATEMENT 1

This thesis is being submitted in partial fulfillment of the requirements for the degree of ...PhD.....(insert MCh, MD, MPhil, PhD etc, as appropriate)

Signed ..... (candidate) Date ...Sept. 28, 2007

STATEMENT 2

This thesis is the result of my own independent work/investigation, except where otherwise stated. Other sources are acknowledged by explicit references.

Signed ..... (candidate) Date ...Sept. 28, 2007

STATEMENT 3

I hereby give consent for my thesis, if accepted, to be available for photocopying and for inter-library loan, and for the title and summary to be made available to outside organisations.

Signed ..... (candidate) Date ...Sept. 28, 2007

STATEMENT 4: PREVIOUSLY APPROVED BAR ON ACCESS

I hereby give consent for my thesis, if accepted, to be available for photocopying and for inter-library loans **after expiry of a bar on access previously approved by the Graduate Development Committee.**

Signed ..... (candidate) Date .....

Acknowledgments

The work of this thesis arose out of a successfully completed EPSRC project (GR/R25682). I would like to thank my supervisors Tim Phillips and Phil Bowen, the main investigators of the project, for many insightful discussions and the guidance as well as the solid support leading to this thesis, and for their encouragement and granting me their strength through the writing of this thesis.

I would like to thank my wife Wenjing especially for being very supportive and patient during the period for this study, her support was of great importance for me to fulfill the writing of this thesis.

Abstract

Spectral element methods are developed for solving two-phase flow problems of relevance to the power generation industry. In particular, an algorithm is presented for predicting the deformation of a Newtonian droplet accelerating from rest in a gas flow field. The dimensionless governing equations are written in terms of four dimensionless groups: Reynolds number, Weber number, and the viscosity and density ratios of the two fluids. The arbitrary Lagrangian-Eulerian (ALE) formulation is used to account for the movement of the mesh. Spectral element approximations are used to ensure a high degree of spatial accuracy. The computational domain is decomposed into two regions, one of which remains fixed in time while the other, located in the vicinity of the droplet, is allowed to deform within the ALE framework. Transfinite mapping techniques are used to map the physical elements onto the computational element. Edges of elements on the free surface are described using an isoparametric mapping and blended into the elemental mapping. Surface tension is treated implicitly and naturally within the weak formulation of the problem. In addition to the movement of the mesh, the computation associated with each time step comprises an explicit treatment of the convection term and an implicit treatment of the linear terms. The generalized Stokes problem generated in the latter is solved using a nested preconditioned conjugate gradient method. The initial code development and the accuracy of the spectral element approximation is validated for the problem of flow over a solid sphere confined in a cylinder or in a uniform ambience. The problem of gas flow over a Newtonian droplet with different fluid properties is then investigated and the effects of changes in the values

of the dimensionless groups on the deformation of the droplet is analysed. Finally, the Cross law is introduced to model the viscosity of non-Newtonian fluids and the problem of gas flow over a blood drop is simulated.

Contents

List of Figures

List of Tables

Chapter 1

Introduction

1.1 Background of the Study

This thesis concerns the utilisation and development of potentially very efficient numerical techniques for droplet deformation in fluid dynamics problems that can be applied, for example, to the problems in efficient fuel consumption, atmospheric pollutant reduction and industrial safety such as risk and hazard mitigation.

Notwithstanding the rapid growth in computer memory and speed over the recent 30 years, there are still areas of fluid dynamics where development is considerably inhibited due to the computational requirements of traditional numerical techniques employed such as the finite volume or finite element methods developed to solve the mathematically modelled governing equations. However, it is the success of computer hardware that has made Direct Numerical Simulation (DNS) of some industrial problems possible, and DNS has found a wide range of applications for turbulent flows in the power generation industry from automotive to gas turbine, to power-generating burner/furnace system (Luo 1999) in the past 10 or more years. In the

meantime, DNS of two-phase liquid-droplet flow fields was utilised in the applications in direct injection (DI) gasoline, diesel or biofuel engines (Comer et al. 2005), gas turbines, hazard quantification and mitigation (Comer et al. 1999, Bowen et al. 1997), and process industries in which it forms the primary focus. Although there are difficulties to be overcome to simulate the droplet deformation in turbulent flows, the techniques developed from the current research (with laminar flows) will be taken as a precursor to it and may also be beneficial to some further studies such as turbulent combustion and flame propagation through sprays (Civi, 1994).

For most industrial applications of DNS of flows involving droplet deformation, for example, the engine combustion as mentioned above, it is still only feasible to study one or two droplets at a time due to the broad range of length scales associated with the problem ranging from the diameter of droplet to the dimensions of the whole flow field such as the combustor itself. Hence, the exchange process between the bulk gas flow and the local movement as well as the deformation of droplet must be studied independently in order to provide a submodel for spray combustion. On the other hand, in computer models of two-phase droplet systems for direct injection combustion, the fuel sprays are usually modelled as a collection of parcels of identical droplets. Obviously, it is impossible to trace all the droplets in a parcel for their deformation with current numerical techniques. Therefore, most spray dynamics such as secondary breakup and coalescence have to be modelled generally by empirically-based submodels relating appropriate non-dimensionalised variables. For instance, the early spray development is usually divided into several processes during atomisation process (Faeth 1996, Bowen and Shirvill 1994), commencing with the so-called primary atomisation regimes, where irregular fluid particles are sheared from the core, and secondary atomisa-

tion, where these particles sub-divide into a finer spray. Due to the excessive computational overhead, the secondary atomisation process is usually characterised in terms of relevant empirical dimensionless relationships, which are embedded as sub-grid models within the global computational fluid dynamics (CFD) scheme (Comer 2005). The main driver for sub-grid modelling is the enormous computational expense of attempting more fundamental approaches. In parallel, sophisticated CFD models have been used to derive the interface exchange coefficients (drag coefficients, energy exchange rate and etc.) between a liquid propellant droplet and the surrounding hot combustion gas products, and the information derived from those CFD codes for droplet behaviour have been compiled and used to establish more accurate physical submodels for spray combustion. However, as most of these studies are based on a perfect spherically shaped droplet, which implies a very large interfacial surface tension, the accuracy of these sub-grid models is greatest when the Weber number is much less than one since the droplet deviates from its spherical shape when the Weber number increases. For Weber numbers greater than one, the droplet may break into smaller drops. To improve the modelling of these phenomena it is necessary to simulate accurately isolated droplets in order to provide quantitative information.

Another practical example of secondary breakup of liquid droplets, in which the sub-grid modelling can be applied, is provided by safety problems in the petrol chemical sector when considering mitigation of accidental explosions using relatively coarse water sprays (Ali 1995, Johns and Thomas 1993, Catlin at el. 1993). Water sprays (deluge) are readily available offshore due to their requirement for fire protection. However, their effectiveness for explosion suppression is governed by whether the explosion itself creates a flow field ahead of the flow sufficient to induce secondary breakup of primary

spray. Secondary breakup is believed to result in a very fine macro-mist, which evaporates over a length scale comparable to the flame thickness, i.e. sufficiently quick to allow suppression or even possibly quenching of the reaction. Previous studies either apply similar Weber/Reynolds number correlation to the engine problem, or introduce the Eotvos number to account for the accelerating flow associated with an explosion.

There are other industrial applications related to the analysis of droplet deformation. For instance, the extension of single droplet studies to chemical reaction (flames) propagating through vapour-gas air mixtures. The relevance and academic interest here may be illustrated by consideration of the DI engine problem again, where ignition occurs in such two-phase hybrid mixtures. Most of the previous numerical research in this area has been undertaken by Sirignano, Aggarwal and co-workers (Continillo and Sirignano 1991, Aggarwal and Sirignano 1985, Seth et al. 1980). Added interest is provided by there being very little validation data (Bowen and Cameron 1999, Cameron 1999) existing for this problem when resident droplet sizes are within the so-called droplet 'transition' range (5-15 microns), so numerical simulation plays a more important role. Phenomenological models indicate that enhanced burning rates may be achieved within fuel droplets of this size, where diffusion and premixed burning occurs simultaneously.

The principal challenge in the numerical simulation of interaction between two immiscible fluids is the ability to track the interface between the fluids, which is arbitrarily-shaped and moving. There are two standard approaches that can be employed for tracking the location and shape of the surface between the two fluids: the Lagrangian and Eulerian approaches.

The former approach is also called predominantly Lagrangian method (Har-

low and Welch 1965, Vicelli 1969, Chen et al. 1995), in which the numerical grid is configured to conform to the shape of the interface and adapts continually to it, so that the interface is maintained as a discontinuity and its evolution is explicitly tracked. Another characteristic of the method is that the computational mesh moves with the same velocity as that of the local fluid. This seems to be the most natural way of tracking the interface since then it is always located at well-defined positions on the mesh, and boundary conditions can be applied at the exact location of the interface as they are known explicitly at each instant. However, as the grid adapts the interface, mesh rearrangement and motion terms have to be incorporated. When the interface begins to distort, it is necessary to perform some remeshing of the computational domain, which may require the solution of another differential equation (Thompson et al. 1985), as the resulting grid on which the field variables are computed may be too skewed and unevenly distributed for the field solver to maintain accuracy. Lagrangian methods have so far experienced difficulty in handling topological changes, mainly due to the breakdown of the structured mesh rearrangement and the need for redistribution of the field information in the vicinity of the interface for unstructured grid domain constructions (Wang and McLay 1986). For example, a two-dimensional Lagrangian model has been developed by Fyfe et al. (1987 and 1988) to simulate the deformation of a 2D incompressible droplet under different conditions. A triangular grid was used to track the interface more accurately. However, the scheme was difficult to extend to three dimensions because of the complications of implementing efficient reconnection algorithms.

On the other hand, the Eulerian approach (Hirt and Nichols 1981, Liang et al. 1988, Ashgriz and Poo 1991) usually employs a fixed grid formulation, and the interface between the two fluids is not explicitly tracked but

reconstructed from the properties of appropriate field variables such as phase fractions. This is also called the volume tracking scheme. Eulerian methods do not have the problems caused by distortions, but may need elaborate procedures to deduce the interface location based on the volume fraction information, and uncertainty corresponding to one mesh cell is unavoidable. Furthermore, modelling or the solution of additional equations is required to obtain information regarding fluid phase fractions or other functions yielding information in the two-phase regions. Another shortcoming of the methods is that the boundary conditions are manipulated to appear in the governing transport equations (Brackbill et al. 1992), which leads to smearing of boundary information. The main advantage of Eulerian method is its fixed grid, because of which there is no need for mesh rearrangement and field interpolation. However, in Eulerian schemes mergers and fragmentations are taken care of automatically, merely by updating values of the phase fraction field. Hence, when the interface is arbitrarily shaped, the detailed physical and geometrical features involved during the interfacial movement and deformation may not be fully resolved and improved accuracy in desired regions is difficult to obtain due to the smearing of information as mentioned above.

The shortcomings of pure Lagrangian and Eulerian descriptions prompted the development of what are known as arbitrary Lagrangian-Eulerian (ALE) techniques. These methods utilize the advantages of both the Lagrangian and Eulerian formulations whilst at the same time avoiding their drawbacks. The idea of ALE may be traced back to the mark-and-cell method (Chan and Street 1970, Daly 1969 and Vicelli 1969) and earlier work by Noh (1964), but it was first proposed in the finite difference context by Hirt et al. in 1974. In the 1980s the method was developed for finite element applications by

Donea et al. (1982) and Belytschko et al. (1980) for their studies of fluid structure problems. The ALE approach is based on the arbitrary movement of the reference frame (the grid within the computational domain), i.e. the reference system is not fixed a priori in space or associated with the fluid. It may be considered as a computational reference system that can be chosen quite arbitrarily and is continually changing in order to allow for the precise description of moving interfaces and ensure the integrity of the mesh over time.

Alternative methods for performing numerical simulations of problems involving a computational domain that is evolving in time include, for example, the space-time finite element method developed by Hughes and Hulbert (1988), and Tezduyar et al. (1992, 1992). In this approach all the spatial as well as temporal co-ordinates are discretized using finite element approximations. The deformation of the spatial domain in time is reflected through the deformation of the mesh in the temporal co-ordinates. An advantage of this approach is its generality. It is possible to view the ALE finite element method as a special case of the space-time method (Behr and Tezduyar 1994).

There are other methods for tracing the moving objectives or boundaries, which may not be included into the above categories. For instance, the distributed Lagrangian multiplier (DLM) particle mover was developed by Glowinski et al. (1999) to simulate fluid-solid systems. The basic idea of the DLM particle mover is to extend a problem defined on a time dependent geometrically complex domain to a stationary, larger but simpler domain known as the ficticious domain. On this fictitious domain, the constraints of rigid body motion of the particles are enforced using a distributed Lagrange mul-

tiplier, which represents the additional body force required to maintain the rigid body motion inside the particle. Another radically different approach is based on the lattice Boltzmann method (LBM). Unlike conventional numerical schemes based on discretization of macroscopic continuum equations, LBM is based on microscopic models and mesoscopic kinetic equations. The idea underlying LBM is to construct simplified kinetic theory models that incorporate the essential physics of the microscopic and mesoscopic processes so that the macroscopic-averaged properties obey the desired macroscopic equations. A full account of LBM may be found in the monograph of Succi (2001).

The development of the ALE technique to simulate the motion of particles in fluids is due to Hu and co-workers (1992, 1996). They performed a 'molecular dynamics' simulation of flowing 'big' particles based on macroscopic equations for both solid and liquid, in which the unsteady solid-liquid two-phase flows are modelled using the Navier-Stokes equations for the liquid and Newton's equations of motion for the particles. A finite element scheme was developed for the solution of those equations for both Newtonian and viscoelastic fluids in two and three-dimensional geometries. A clear outline for the standard procedure of ALE algorithms for DNS of particles was also given in their work, and especially a combined weak formulation incorporating both the fluid and particle equations of motion was introduced (Hu et al. 2001). The advantage of this approach is that the hydrodynamic forces and moments on the particles do not need to be computed explicitly, thus contributing to a more stable scheme.

In recent years, there have been quite a number of applications of ALE techniques to fluid-structure problems and various coating problems, i.e. free

boundary problems, whilst comparably fewer numerical models for droplet deformation were developed in spite of the similarity between the two kinds of problems. A numerical simulation based on an ALE algorithm for droplet deformation in convective flows was developed by researchers of Tennessee University in early 1990s (Deng and Jeng, 1992). Since both gas and liquid phases are assumed to be inviscid in this work, the surface tension force acting on the interface separating the drop and gas flows plays a more important role. A two-dimensional predictor-corrector finite difference scheme was constructed to solve the governing Navier-Stokes equations. Again due to the inviscid fluids assumption, the oscillation of a spheroidal drop in a vacuum environment is simulated and the deformation of a spherical water droplet is tested for a wide range of Reynolds number and Weber number, which represents the ratio of external aerodynamic force to the surface tension force. Furthermore, a rough comparison between experimental work (Norton 1990) and computational results is made and the similarities in the shapes of the deformed drops are obtained.

An implementation of ALE within the the spectral element context was originally proposed by Ho and Patera (1990, 1991). They used the technique to simulate free surface flows, in which the spectral element approximation introduces high-order accuracy into the spacial discretization.

Helenbrook and Edwards (2000), and Helenbrook (2001) developed a spectral element formulation with the ALE methodology for axisymmetric two-fluid flows, and, as an application of their numerical model, the deformation of a hexane drop in ambient gas flows, with the highest Reynolds to be 112, was simulated. The advantage of this approach is that the spectral elements provide a high degree of accuracy while an unstructured mesh is used to

allow problems with highly deformed interfaces to be discretized and properly calculated using its geometric flexibility. Another unique feature of this formulation is a fully implicit time advancement algorithm which is made possible by the development of a spectral-multigrid iteration scheme. Some accurate results have been shown from this work for the initial deformation of an originally spherical droplet for a range of Weber number values with the highest $We = 4$. The highest polynomial order for the discretization of the spectral elements is four, so that the unstructured mesh for this simulation is not far away from that used by lower-order finite element schemes.

Spectral element methods possess several advantages over lower-order methods of discretization, such as finite volume or finite element methods, when solving problems with complex geometry that is deforming in time. Although for a given number of degrees of freedom spectral element methods are more expensive than their lower-order counterparts, far fewer degrees of freedom are required to obtain a prescribed accuracy when spectral elements are used. In addition, the high-order basis functions that are used in spectral elements can sustain greater deformation with less deterioration in accuracy than if lower-order elements are used, and in the mean time provide more natural geometrical approximations for the deforming shapes of the droplets that are being tracked. Furthermore, if linear transformations are used to map the spectral elements onto the parent element then the ratio of the work done to perform the mesh movement relative to the work done to resolve the flow is significantly decreased. And during the mesh movement, the mesh structure can be controlled to a reasonable configuration for the calculation of next time step only by the positions of the vertices of the spectral elements, while part of these vertices can be arbitrarily moved under an ALE algorithm. With low order methods such as linear finite element schemes there is one to

one correspondence between flow variables and mesh variables, whereas for spectral elements the resolution of the flow can be increased without increasing the effort in moving the mesh.

Apart from the numerical modelling and simulation, various experimental measurements have been done for droplet deformations in different fluids and flow conditions, but data are usually available for specific configurations. However, the deformation of liquid droplets and associated breakup may be classified in a number of modes of fragmentation. Pilch and Erdman (1987) presented a triangular relationship built on the concept of a critical Weber number, breakup time data and velocity history data for prediction of the size of stable fragments. Their work is based on a collection of these three kinds of data on acceleration-induced deforming and fragmenting of liquid drops from the literature, which presents a consistent basis. After about a decade, another analysis of experimental data on the critical conditions of drop breakup by aerodynamic forces was given by Shraiber et al. (1996), who explained the possible causes of divergence among data on the critical Weber number obtained by different authors. In both articles the various fragmentations of liquid drops are divided into a number of modes such as vibrational mode, bag mode, transitional mode etc., which provide a general category for correlated numerical predictions to compare. Due to industrial requirements, the data for deforming drops in combustion environments are usually measured in high speed gas flows, for instance one may cite the work by Joseph et al. (1999) and by Berthoumier et al. (1999). However, deformation of viscous droplets may only be tracked numerically in low speed flows for most computing environments in research or industrial applications. Therefore, both numerical prediction and experimental verification are recommended to be carried out in one laboratory work, like the research done

by Wannaborworn et al. (2002), Feigl et al. (2003) and by Wu et al. (2004), for accurate comparisons.

1.2 Aim of the Thesis

With current commercial engine codes employing CFD techniques, numerical simulations of droplet-gas interactions are most accurate when the drop Weber number is less than one, as mentioned in last section. As the Weber number increases the drop deviates from a spherical shape, this increasing drag, causing a reduction in the accuracy of the numerical predictions and leading to breakup. Since modelling these phenomena requires the accurate simulation of an isolated liquid drop in the atomization process, the purpose of this study is to utilise highly efficient numerical techniques to solve the important free-boundary two-fluid problem of droplet deformation with low Reynolds number and critical Weber number – the precursor to droplet breakup. The focus will be on the accuracy of tracking the moving interface between the drop and the ambient gas flow, and the ability of the numerical algorithms employed to handle the complex droplet surface that evolves in the process of deformation.

An arbitrary Lagrangian-Eulerian algorithm is chosen to track the drop surface explicitly, in which the mesh velocity is incorporated into the weak formulation of the governing equations so that there is no requirement to perform on interpolation of the field variables when remeshing is needed. The velocity at mesh nodes may be chosen arbitrarily to assure that the system of algebraic equations for next instant in time can be solved accurately and efficiently.

The widely used spectral element method is applied to the spatial approx-

imation of the Navier-Stokes equations with quadrilateral spectral elements used to construct the computational domain and conform the free surface. High order polynomials are adopted to ensure both accurate solution for the flow field and natural shape of the droplet. In addition, with spectral element methods the mesh velocity is easily controlled only by the vertices of the skeleton spectral elements. A higher order temporal discretization is also adopted to generate a more stable solver for the governing equations.

Another important numerical technique employed in the solution procedure is mixed mapping method. In this part of the calculation, each spectral element is mapped onto the reference square $[-1, 1]^2$ using a transfinite mapping scheme or, in the case of elements with a side adjacent to the interface, a hybrid transfinite/isoparametric mapping. The linear transfinite mapping makes the transformation efficient, whereas in the isoparametric mapping the order of the polynomials is the same as that in the expansion bases of the spectral elements, which guaranties an accurate shape for the interface when the polynomial order used is high.

1.3 Software Development

All the results presented in this thesis have been generated using newly developed software, which was programmed from scratch. A few subroutines performing some basic functions, such as the generation of Gauss-Lobatto points by Dr Marc Gerritsma, former research associate at Aberystwyth, are used in the code. A program to solve the Stokes equations for simulating two-dimensional flow past a cylinder, developed in Prof. T. N. Phillips' group at Aberystwyth, was referenced during the programming. The spectral element Stokes solver was tested and coded with the iterative preconditional

conjugate gradient (PCG) method in Cartesian coordinates. Iterative solvers provide the possibility of tackling large problems as they do not claim much memory associated to the storage of discrete spectral element operators. The new code was programmed in cylindrical polar coordinates on a two and half dimensions axisymmetric basis, in which all the development such as the ALE scheme manipulation, the two-fluid Navier-Stokes resolution, the blending mapping onto complex geometries and etc. are based on a newly developed Stokes solver using the PCG method for carrying out the simulation of channel flows past a solid sphere.

To create potentially sophisticated interfacial geometry and the meshes used for the computations, the facility to use Gambit is included. This has made the new code flexible in terms of geometric construction. Gambit is a meshing software provided by the commercial CFD code Fluent.

All the programs have been written in Fortran and implemented on Unix and Linux platforms. The code is compiled using the Fortran compiler f90 and may be compiled by g77 if slightly modified.

1.4 Arrangement of the Chapters

The following is the description for the contents of this thesis.

In chapter 2, the non-dimensional governing equations for gas flows past a single droplet are derived from the point of view of dispersed two-phase flows. A variational formulation of the governing equations is also given and consideration is given to the incorporation of surface tension at the interface between the two fluids, as well as the mesh velocity, within the weak formalation. The weak formulation plays the role of a bridge between the theoretical

equations and finite element or spectral element approximations.

Details of the chosen spectral element method, such as nodal type parametric polynomial interpolations and how the method works together with the hybrid transfinite/isoparametric mapping, are written in chapter 3. Based on this, the spatial discretization and a semi-discretized algebraic system of the governing equations are derived. The temporal discretization schemes and the PCG algorithm that solves the discretized equations are given in chapter 4. This involves presenting the operators that need to be inverted and how the iterative method is manipulated for the inversion. Also in this chapter, simulations of flow past a sphere and a comparison with the literature are shown for the purpose of code validation.

Details of the ALE scheme are described in chapter 5. A dimensionless form of the two-fluid Navier-Stokes equations with explicitly parameterized Weber number, density ratio and viscosity ratio for the convenience of result analysis is also given. In chapter 6, the problem of gas flows over single Newtonian droplet is investigated, the effects of changes in the values of the dimensionless parameters on the deformation of the droplet are analysed, and various results are presented.

Some numerical simulations of gas flows over non-Newtonian drops are shown in chapter 7 and the conclusions to the work presented in this thesis as well as suggestions for future work are given in chapter 8.

Chapter 2

Governing Equations and Variational Formulation

2.1 Introduction

Except for injection and atomization flows, there are many other similar flows in industrial activities such as oil droplets driven by water in transport pipe lines, boiling water flows in nuclear reactors, sprays in cooling towers, etc. Such flows are called dispersed bubbly two-phase or multiphase flow. No matter that the main, or say, the continuous fluid is liquid, gas or air, the common characteristic of these flows is that the discrete gas bubbles or liquid droplets flow as inclusions driven by a continuous fluid. So that the field equations, e.g. the Navier-Stokes equations, still govern within an area only containing one of the fluid phases in the flows. Nevertheless, to solve those equations one has to define interfacial boundary conditions and deal with complex moving geometries, which is almost impossible for most flow situations. Therefore, various averaging methods (e.g. Ishii 1975, Drew 1983) were developed to avoid searching for individual interfacial interactions be-

tween fluid phases and to solve averaged macroscopic flow fields. Nowadays many two-phase flow problems are solved with the methods in this category, the drawback of which is that only averaged flow properties can be known. Due to the aim of the work for this thesis is to trace a deforming drop in a gas flow, the interfacial condition is comparably simpler and can be modelled physically, and the two-phase equations will be degenerated and solved for accurate flow fields.

In this chapter, a set of conservation equations for dispersed two-phase flow are given at first, then the simplification of those equations for the numerical simulation of single droplet deforming in a gas flow is discussed and the non-dimensionalised governing equations of the problem in cylindrical polar coordinates are derived. Finally the weak formulation of the governing equations including the interfacial tension modelling is derived.

2.2 Instantaneous Equations for Dispersed Two Phase Flows

The fundamental physical laws which govern the behaviour of droplets, bubbles or other particles in a fluid are the principles of conservation of mass, momentum and the first law of thermodynamics. Application of these laws to an infinitesimal element of material, or control volume, can be used to construct a set of governing equations for the continuity of mass, momentum and energy of the system, which are given as follows (Ishii 1975, Drew 1983). The energy equation is not included as the present work is concerned with isothermal flows, i.e. temperature is assumed to be constant. From a spatial averaging procedure we have

Mass conservation equation for continuous phase

$$\frac{\partial(\alpha_c\,\rho_c)}{\partial t} + \nabla\cdot(\alpha_c\,\rho_c\,\mathbf{u}_c) = r_c \tag{2.1}$$

where ρ_c and $\mathbf{u}_c$ are the density and velocity, respectively, of the continuous phase, α_c is the volume fraction of the continuum in the infinitesimal element and r_c is the total increase in mass for the continuous phase per unit volume of the mixture due to the droplet phase transfer.

Mass conservation equation for droplet phase

$$\frac{\partial(\alpha_d\,\rho_d)}{\partial t} + \nabla\cdot(\alpha_d\,\rho_d\,\mathbf{u}_d) = r_d \tag{2.2}$$

where ρ_d and $\mathbf{u}_d$ are the density and velocity of the droplet phase, α_d is the volume fraction and r_d is total mass increase of the droplet phase.

If gravity is ignored and it is assumed that no mass transfer occurs between the two phases, then we have:

Momentum conservation equation (continuous phase)

$$\frac{\partial(\alpha_c\,\rho_c\mathbf{u}_c)}{\partial t} + \nabla\cdot(\alpha_c\,\rho_c\,\mathbf{u}_c\,\mathbf{u}_c\,) = -\alpha_c\,\nabla p + \nabla\cdot(\alpha_c\tau_c) + M_c \tag{2.3}$$

where τ_c is the viscous stress tensor, M_c is the interfacial force on the continuous phase which can be calculated by including one or more of the interaction forces (e.g. drag force or the Saffman lift force etc. (Ishii 1975)).

Momentum conservation equation (droplet phase)

$$\frac{\partial(\alpha_d\,\rho_d\mathbf{u}_d\,)}{\partial t} + \nabla\cdot(\alpha_d\,\rho_d\,\mathbf{u}_d\,\mathbf{u}_d\,) = -\alpha_d\,\nabla p + \nabla\cdot(\alpha_d\tau_d) + M_d. \tag{2.4}$$

Here, τ_d is the viscous stress tensor for droplets, M_d is the interfacial force on the droplet phase due to the continuum, and

$$M_d = -M_c \tag{2.5}$$

The above are so-called instantaneous equations in the literature for dispersed two-phase flow and are based on the assumption that both phases behave as a continuum microscopically, whilst only the carrier fluid physically behaves as a continuum macroscopically. If the flow is laminar the key to solving these equations is to model M, the interfacial force.

2.3 Governing Equations for Gas Flow Over a Single Droplet

As the research in this thesis is to trace the deformation of a single droplet in a gas flow, the equations discussed in Section 2.2 may be simplified. If the geometry of the domain for the calculation is set up as shown in Fig. 2.1 we may divide it into two separate sub-domains by the interface between the two phases.

Therefore, in the region of continuous gas flow, $\alpha_c = 1, \alpha_d = 0$, in the other part filled by the droplet, $\alpha_c = 0, \alpha_d = 1$; and the interfacial force M only contributes in the interface between those two sub-domains. Thus, the simplified equations are:

Continuity equations

$$\frac{\partial \rho_k}{\partial t} + \nabla \cdot (\rho_k \, \mathbf{u}_k) = 0, \tag{2.6}$$

where k = c and d to represent gas continuum and droplet, so that these are two equations governing the flow within the two sub-domains respectively. Due to the contribution of the mesh used in solving the equations, there is no phase transfer existing, i.e. $r_c = r_d = 0$.

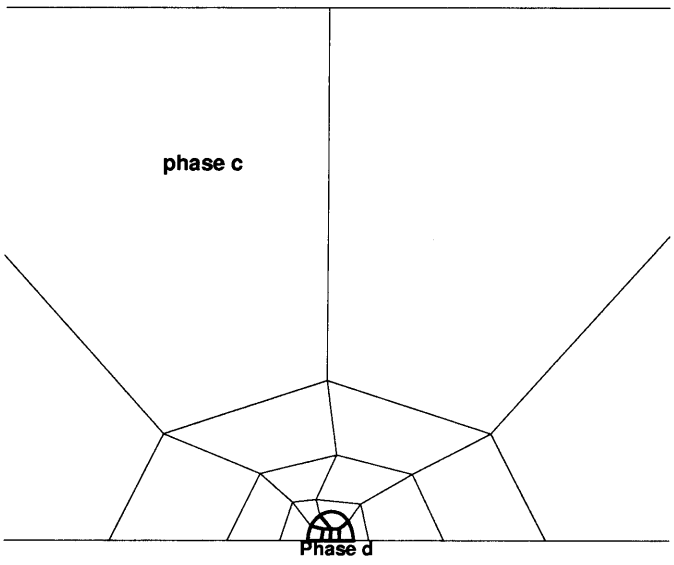

Figure 2.1: Two-fluid domain for the computation of droplet deformation.

The momentum equations

$$\frac{\partial(\rho_k \mathbf{u}_k)}{\partial t} + \nabla \cdot (\rho_k \mathbf{u}_k \mathbf{u}_k) = -\nabla p + \nabla \cdot (\alpha_k \tau_k) + M_k. \tag{2.7}$$

Similarly here k = c or d to represent the two phases, the body force is ignored and the interfacial force M_k is only nonzero on the interface.

For the convenience of numerical discretization we write equations (2.6) and (2.7) in scalar forms as follows. Considering the flows that we simulate are viscous and incompressible as the speed of the fluids is under the sub-sonic level, then we have

The continuity equation

$$\frac{\partial u_k}{\partial x} + \frac{\partial v_k}{\partial y} = 0 \tag{2.8}$$

The u-momentum equation

$$\begin{aligned} &\frac{\partial u_k}{\partial t} + u_k \frac{\partial u_k}{\partial x} + v_k \frac{\partial u_k}{\partial y} \\ &= -\frac{1}{\rho_k}\frac{\partial p}{\partial x} + \frac{1}{\rho_k}\frac{\partial}{\partial x}\left\{2\mu_k \frac{\partial u_k}{\partial x} + \mu_k\left(\frac{\partial u_k}{\partial y} + \frac{\partial v_k}{\partial x}\right)\right\} + M_k^u \\ &= -\frac{1}{\rho_k}\frac{\partial p}{\partial x} + \frac{\mu_k}{\rho_k}\left(\frac{\partial^2 u_k}{\partial x^2} + \frac{\partial^2 u_k}{\partial y^2}\right) + M_k^u. \end{aligned} \tag{2.9}$$

The v-momentum equation

$$\begin{aligned} &\frac{\partial v_k}{\partial t} + u_k \frac{\partial v_k}{\partial x} + v_k \frac{\partial v_k}{\partial y} \\ &= -\frac{1}{\rho_k}\frac{\partial p}{\partial y} + \frac{1}{\rho_k}\frac{\partial}{\partial y}\left\{\mu_k\left(\frac{\partial v_k}{\partial x} + \frac{\partial u_k}{\partial y}\right) + 2\mu_k \frac{\partial v_k}{\partial y}\right\} + M_k^v \\ &= -\frac{1}{\rho_k}\frac{\partial p}{\partial y} + \frac{\mu_k}{\rho_k}\left(\frac{\partial^2 v_k}{\partial x^2} + \frac{\partial^2 v_k}{\partial y^2}\right) + M_k^v \end{aligned} \tag{2.10}$$

and

$$M_c = -M_d,$$

Here only the two-dimensional formulation is given for simplicity, u_k, v_k are the components of $\mathbf{u}_k$, and μ_k is the kinematic viscosity of the droplet or gas. It is noted that although p represents the pressure field for whole domain, there is a pressure jump on the interface, which means that pressure is discontinuous at the interface because of surface tension.

Since the current generation of computers may not be efficient enough to solve three-dimensional flow problems using spectral element methods, an axisymmetric assumption is made for the problems to be solved in this thesis. Therefore, it is more convenient for the calculations to be carried out if we transform the above equations into cylindrical polar coordinates as follows

The continuity equation

$$\frac{\partial u_k}{\partial z} + \frac{\partial v_k}{\partial r} + \frac{v_k}{r} = 0. \tag{2.11}$$

The u-momentum equation

$$\begin{aligned} &\frac{\partial u_k}{\partial t} + u_k \frac{\partial u_k}{\partial z} + v_k \frac{\partial u_k}{\partial r} \\ &= -\frac{1}{\rho_k} \frac{\partial p}{\partial z} + \frac{\mu_k}{\rho_k} \left(\frac{\partial^2 u_k}{\partial z^2} + \frac{\partial^2 u_k}{\partial r^2} + \frac{1}{r} \frac{\partial u_k}{\partial r} \right) + M_k^u. \end{aligned} \tag{2.12}$$

The v-momentum equation

$$\begin{aligned} &\frac{\partial v_k}{\partial t} + u_k \frac{\partial v_k}{\partial z} + v_k \frac{\partial v_k}{\partial r} \\ &= -\frac{1}{\rho_k} \frac{\partial p}{\partial r} + \frac{\mu_k}{\rho_k} \left(\frac{\partial^2 v_k}{\partial z^2} + \frac{\partial^2 v_k}{\partial r^2} + \frac{1}{r} \frac{\partial v_k}{\partial r} - \frac{v_k}{r^2} \right) + M_k^v, \end{aligned} \tag{2.13}$$

where z is the coordinate along the symmetry axis and r is the radial coordinate. Actually, the above equations are the form of governing equations to be solved for the moving droplet problem in our work.

2.4 Non-dimensionalization of the Governing Equations

Since the parameters representing the flow problems may differ by several orders of magnitude, e.g. ρ/μ may be about 10^7 or higher, the governing equations are solved in their non-dimensional form. The scales chosen for the non-dimensionalization are as follows

- The velocity scale: U, usually it is the maximum inflow velocity.
- The length scale: L may be the diameter of the initial droplet or a solid sphere, or the radius of a cylindrical channel (domain for the computation).
- The pressure scale: $\rho\, U^2$, here ρ is either the density of the gas or the droplet depending on which phase the equations govern.
- The time scale: L/U is a dependent scale.

If we define $z^* = \dfrac{z}{L}$, $r^* = \dfrac{r}{L}$, $u^* = \dfrac{u}{U}$, $v^* = \dfrac{v}{U}$, $t^* = \dfrac{t}{L/U}$, $p^* = \dfrac{p}{\rho\, U^2}$ in equation (2.11)-(2.13) and apply the chain rule we have

$$\frac{\partial^2 u_k}{\partial z^2} + \frac{\partial^2 u_k}{\partial r^2} = \frac{\partial}{\partial z}\left(\frac{\partial u_k}{\partial u_k^*}\frac{\partial u_k^*}{\partial z^*}\frac{\partial z^*}{\partial z}\right) + \frac{\partial}{\partial r}\left(\frac{\partial v_k}{\partial v_k^*}\frac{\partial v_k^*}{\partial r^*}\frac{\partial r^*}{\partial r}\right)$$

$$= \frac{L}{U^2}\left(\frac{\partial^2 u_k^*}{\partial z^{*2}} + \frac{\partial^2 v_k^*}{\partial r^{*2}}\right)$$

etc., and withdraw superscript stars, then the governing equations become

The continuity

$$\frac{\partial u_k}{\partial z} + \frac{\partial v_k}{\partial r} + \frac{v_k}{r} = 0 \tag{2.14}$$

The u-momentum

$$\begin{aligned} &\frac{\partial u_k}{\partial t} + u_k \frac{\partial u_k}{\partial z} + v_k \frac{\partial u_k}{\partial r} \\ &= -\frac{\partial p}{\partial z} + \frac{1}{Re}\left(\frac{\partial^2 u_k}{\partial z^2} + \frac{\partial^2 u_k}{\partial r^2} + \frac{1}{r}\frac{\partial u_k}{\partial r}\right) + M_k^u \end{aligned} \tag{2.15}$$

The v-momentum

$$\begin{aligned} &\frac{\partial v_k}{\partial t} + u_k \frac{\partial v_k}{\partial z} + v_k \frac{\partial v_k}{\partial r} \\ &= -\frac{\partial p}{\partial r} + \frac{1}{Re}\left(\frac{\partial^2 v_k}{\partial z^2} + \frac{\partial^2 v_k}{\partial r^2} + \frac{1}{r}\frac{\partial v_k}{\partial r} - \frac{v_k}{r^2}\right) + M_k^v \end{aligned} \tag{2.16}$$

where

$$Re = \frac{\rho U L}{\mu}$$

is the Reynolds number of the flow and in the new scale system M_k is different in value from its previous version, i.e.

$$M_k^* = \frac{L}{\rho_k U^2} M_k$$

One should keep this in mind when it needs to be modelled. Obviously, equations (2.14)-(2.16) are the non-dimensional form of equations (2.11)-(2.13).

2.5 Boundary Conditions

In this thesis, the numerical simulation of droplet deformation in a gas flow usually starts from a well developed steady channel flow or an ambient flow over a solid sphere (the initial shape of the drop), which has been calculated at the beginning as an initial condition for the moving boundary problem. The boundary conditions are usually set as in the following:

- Velocity 1

  The axial component of velocity u with parabolic profile such as

  $$u = 1 - \frac{r^2}{h^2}$$

  is applied to the inlet and the outlet of the channel, here h is the radius of the channel. The radial component of the velocity v at the inlet and outlet is set to be zero.

  For the solid wall of a channel, the boundary condition is no slip, which means

  $$u = v = 0$$

  at the wall. Since the flow is assumed to be laminar, and furthermore it is assumed that the droplet deforms axisymmetrically, which is reasonable as long as the effect from gravitation is ignored, the flow field is symmetric around the central line ($r = 0$), so that we have

  $$v = 0, \frac{\partial u}{\partial r} = 0$$

  on the symmetry axis. Note that u is free here.

- Velocity 2

  Uniform inflow and outflow velocity is also used ($v = 0, u = 1$ for non-dimensional calculations) to trace a moving and deforming drop in a combustion chamber, the slip-wall condition for the outer boundary of the computation domain is applied correspondingly and symmetry conditions are still applied on the axis (see Fig. 2.1).

- Pressure

The spectral element method used to solve the conservative equations in this thesis solves the pressure on a lower order of polynomial space. Therefore, there is no need for pressure boundary condition to be imposed. The mean level of pressure is determined within the spectral element discretization.

2.6 Variational Formulation

2.6.1 The Weak Formulation of the Governing Equations

The governing equations discussed in previous sections will be solved using a spectral element method which is based on a weak formulation of the problem. The domain for the calculation with a moving boundary is divided into two subdomains using the interface to separate the different fluids, no matter how it deforms. Keeping this in mind, we drop the subscript k and taking inner product of equations (2.14)-(2.16) with test functions $\vec{\varphi}$ and q respectively, then we have

$$\int_{\Omega(t)} \left\{ \frac{\partial u}{\partial t} + u \frac{\partial u}{\partial z} + v \frac{\partial u}{\partial r} \right\} \varphi_z \, dV =$$

$$- \int_{\Omega(t)} \frac{\partial p}{\partial z} \varphi_z \, dV + \frac{1}{Re} \int_{\Omega(t)} \left\{ \frac{\partial^2 u}{\partial z^2} + \frac{\partial^2 u}{\partial r^2} + \frac{1}{r} \frac{\partial u}{\partial r} \right\} \varphi_z \, dV \qquad (2.17)$$

$$+ \int_{\Omega(t)} M_k^u \, \varphi_z \, dV,$$

$$\int_{\Omega(t)} \left\{ \frac{\partial v}{\partial t} + u \frac{\partial v}{\partial z} + v \frac{\partial v}{\partial r} \right\} \varphi_r \, dV =$$

$$- \int_{\Omega(t)} \frac{\partial p}{\partial r} \varphi_r \, dV + \frac{1}{Re} \int_{\Omega(t)} \left\{ \frac{\partial^2 v}{\partial z^2} + \frac{\partial^2 v}{\partial r^2} + \frac{1}{r} \frac{\partial v}{\partial r} - \frac{v}{r^2} \right\} \varphi_r \, dV \qquad (2.18)$$

$$+ \int_{\Omega(t)} M^v \, \varphi_r \, dV,$$

and

$$\int_{\Omega(t)} \left\{ \frac{\partial u}{\partial z} + \frac{\partial v}{\partial r} + \frac{v}{r^2} \right\} q \, dV \; = \; 0, \tag{2.19}$$

where $\vec{\varphi} = (\varphi_z, \varphi_z)$ and q are the velocity and pressure test functions. The domain of computation $\Omega(t)$, which consists of two adjacent non-overlapping domains $\Omega_c(t)$ and $\Omega_d(t)$ occupied by continuous phase and the droplet respectively, is a function of time since the location of the interface between the two fluids evolves in time as the droplet deforms. Therefore, on $\Omega(t)$ we have a continuous velocity field and a pressure field that is only discontinuous at the interface, caused by a pressure jump due to the interfacial tension.

Although the same velocity scale U and the length scale L are used for both fluids in all the flows simulated, the Reynolds numbers Re^c and Re^d are not the same because of the different viscosities and densities of the two fluids. The weighted integral of the drag M may be calculated using integration-by-parts (Ishii, 1975)

$$\int_{\Omega(t)} M^{u_i} \varphi_i \, dV \; = \; - \int_{\Omega(t)} \frac{\partial M^{u_i}}{\partial x_i} \frac{\varphi_i^2}{2} \, dV \; + \int_{\partial\Omega(t)} M^{u_i} \frac{\varphi_i^2}{2} \, ds$$

Here $\partial\Omega(t)$ denotes the element edge, $\varphi_i = \varphi_r$ *or* φ_z, $x_i = z$ *or* r and $u_i = u$ *or* v are to represent two-dimensional axisymmetric components of the test function, the coordinates and the velocity. Since M is only evaluated at the interface, the first term in the right hand side of the above equation is zero. To solve the variational form of the governing equations using spectral element methods $\Omega(t)$ needs to be divided into a number of spectral elements $\Omega_i(t)$ $(i = 1, \cdots, N)$. In this way, $\int_{\partial\Omega(t)} M_k^{u_i} \frac{\varphi_i^2}{2} ds$ is repeated by the integrations on adjacent elements, and the contributions cancel each other because of $M_c^{u_i} = -M_d^{u_i}$ (Ishii, 1975). However, for the element edges on the interface a pressure jump needs to be accounted for because of existence of surface tension (the interface is always located along element boundaries in mapping). Therefore,

$\int_{\partial\Omega(t)} M^{u_i} \frac{\varphi_i^2}{2}\, ds$ may be removed from equations (2.17) and (2.18) for the gas phase after performing direct summation, whereas a term of the form: $\int_{\partial\Omega(t)} \sigma\, \kappa\, n_z \varphi_z\, ds$ remains in the weak form of the momentum equations for the droplet phase (Ho and Patera, 1989).

Applying intgration-by-parts to the right-hand side terms of equation (2.17) and (2.18), for example

$$\int_{\Omega(t)} \frac{\partial p}{\partial r} \varphi_r\, dV = -\int_{\Omega(t)} \frac{\partial \varphi_r}{\partial r}\, p\, dV + \int_{\partial\Omega(t)} \varphi_r\, p\, ds$$

$$= -\int_{\Omega(t)} \frac{\partial \varphi_r}{\partial r}\, p\, dV,$$

where the second term in the right-hand side is zero since $\varphi_r = 0$ on inner boundaries and at the flow boundaries. Thus, after some further manipulations equations (2.17)-(2.19) for the droplet become

$$\int_{\Omega(t)} \left\{ \frac{\partial u}{\partial t} + u \frac{\partial u}{\partial z} + v \frac{\partial u}{\partial r} \right\} \varphi_z\, r dr dz =$$

$$\int_{\Omega(t)} \frac{\partial \varphi_z}{\partial z}\, p\, r dr dz + \int_{\partial\Omega(t)} \sigma\, \kappa\, n_z \varphi_z\, ds$$

$$-\frac{1}{Re} \int_{\Omega(t)} \left\{ \frac{\partial \varphi_z}{\partial z} \frac{\partial u}{\partial z} + \frac{\partial \varphi_z}{\partial r} \frac{\partial u}{\partial r} \right\} r dr dz, \tag{2.20}$$

$$\int_{\Omega(t)} \left\{ \frac{\partial v}{\partial t} + u \frac{\partial v}{\partial z} + v \frac{\partial v}{\partial r} \right\} \varphi_r\, r dr dz =$$

$$\int_{\Omega(t)} \frac{\partial \varphi_r}{\partial r}\, p\, r dr dz + \int_{\partial\Omega(t)} \sigma\, \kappa\, n_r \varphi_r\, ds$$

$$-\frac{1}{Re} \int_{\Omega(t)} \left\{ \frac{\partial \varphi_r}{\partial z} \frac{\partial v}{\partial z} + \frac{\partial \varphi_r}{\partial r} \frac{\partial v}{\partial r} + \frac{v}{r^2} \varphi_r \right\} r dr dz, \tag{2.21}$$

and

$$\int_{\Omega(t)} \left\{ u \frac{\partial q}{\partial z} + v \frac{\partial q}{\partial r} + \frac{v}{r^2} q \right\} r dr dz = 0, \tag{2.22}$$

where $rdrdz$ is dV in the cylindrical polar coordinates, $\partial\Omega(t)$ represents the interface, and s is the distance along the interface.

2.6.2 Surface Tension Modelling

In equations (2.21) and (2.22) the term

$$\int_{\partial\Omega(t)} \sigma\,\kappa\, n_i \varphi_i\, ds \qquad i = z \text{ or } r \tag{2.23}$$

is the integral of the the pressure jump caused by the interfacial tension, σ is the surface tension coefficient usually measured in experiments for various fluids and assumed to be constant, $\vec{n} = (n_z, n_r)$ is the normal vector to the interface and κ is the intermediate curvature of the interface, which is defined by

$$\kappa = \frac{1}{R_1} + \frac{1}{R_2},$$

where R_1, R_2 are the local principal radii of curvature. The surface tension force at an interface between two fluids depends on the mixed curvature of interface. For an arbitrarily shaped surface, the principal radii of curvature are very difficult to determine both theoretically and numerically. But in the present work, we deal with an axisymmetric, or say two and half dimensional, surface. In this case, these principal radii of curvature can be specified relatively simply. Let the droplet profile be of parametric form $r = r(s), z = z(s)$, where r is the distance from the axis of symmetry, z is another distance along the axis (the location of the co-ordinates is set up in this way), and s is the distance along the material interface on the vertical plane through the symmetric axis, then the radii of curvature can be obtained as (Deng and Jeng 1992)

$$\frac{1}{R_1} = \left(\frac{dz}{ds}\frac{d^2r}{ds^2} - \frac{dr}{ds}\frac{d^2z}{ds^2}\right)\left[\left(\frac{dz}{ds}\right)^2 + \left(\frac{dr}{ds}\right)^2\right]^{-\frac{3}{2}},$$

$$\frac{1}{R_2} = \frac{dz}{ds}\, r^{-1} \left[\left(\frac{dz}{ds} \right)^2 + \left(\frac{dr}{ds} \right)^2 \right]^{-\frac{1}{2}}.$$

More specially for a two-dimensional surface such as a cylinder, R_2 is infinite so that $1/R_2 = 0$.

Chapter 3

Discretization with Spectral Element Methods

3.1 Introduction

The spectral element (SE) method is essentially a discretization method for determining an approximate solution of partial differential equations (PDEs) expressed in a weak form, based on high order polynomial interpolants used in conjunction with particular quadrature rules. The method was pioneered in the mid 1980's by Anthony Patera at MIT (Patera 1984) and Yvon Maday at Paris-VI (Maday et al 1989).

Earlier developed spectral methods may be viewed as an extreme development of the class of discretization schemes for differential equations known generically as the method of weighted residuals, from which the finite volume method and various finite element methods were also developed. The key elements of the method are the trial functions (also called the p-type expansion or approximate functions) and the test functions (also known as

weight functions). The trial functions are used as basis functions for a truncated series expansion (usually a polynomial) of the solution (the variables in the differential equations to be solved) whilst the test functions ensure that the differential equation is satisfied in some sense as closely as possible by the truncated series expansion. This is achieved by minimising the residual, i.e. the error in the differential equation produced by using the truncated expansion instead of the exact solution, with respect to a suitable norm. An equivalent requirement is that the residual satisfies a suitable orthogonality condition with respect to each of the test functions.

The advantages of the spectral method are the rapid convergence rate and that high accuracy of the approximation to the solution, obtained as a result of the high-order polynomials representations of both trial and test functions. Nevertheless, the method is usually used for limited cases such as single site numerical models (Chandler, 1997) or applied to the area of model comparison due to its characteristic of single block geometry. On the other hand, it is comparatively much easier for finite volume methods and classical finite element methods to handle complex geometries, although less accurate solutions are obtained. Nevertheless, in finite element methods, the basis functions are usually constructed for one specific order of the scheme (they are derived from Lagrange interpolants on regular grids inside each element) and need to be reprogrammed as the order of the scheme is modified.

In a spectral element method, the computational domain is decomposed into elemental contributions, the "h-type extension process", then the spectral method is applied to the sub-domains (the spectral elements) over which vector and scalar unknowns are approximated by N-th order tensor-product polynomial expansions, and PDEs are solved on the whole domain in the

similar ways as that used in finite element methods. The elemental decomposition is an integral part of both h- and p-type finite element methods as the p-type extension is based upon an initial mesh or h-type discretization. Due to varying order polynomials inside quadrilaterals or triangles that form the mesh, the SE method allows for irregular geometries. Therefore, it combines the accuracy of spectral techniques with the geometric flexibility of finite element methods. The spectral element method also exhibits several favourable computational properties, such as the use of tensor products, naturally diagonal mass matrices, adequacy to concurrent implementations, which are shown in the following sections. More background on SE methods can be found in the monograph of Karniadakis and Sherwin (1999).

In the work for this thesis, a nodal-type Legendre polynomial expansion is used for the interpolation approximation on quadrilateral spectral elements, which, including a mapping technique for the computational domain, are discussed in detail in this chapter. The detailed spatial discretization of the governing equations are also given here, whereas the temporal discretization will be discussed in Chapter 4.

3.2 Numerical Methods to Solve PDEs

The best way to solve physical problems governed by a set of partial differential equations is to obtain the analytical solution. However, there are many situations where the analytical solution is extremely difficult or not feasible to determine due to the complex nature of the governing equations such as those obtained in Chapter 2. In many industrial fluid flow problems, domains for the calculations may be so irregular that it is mathematically impossible to describe the boundaries. For instance, the interface between the drop

and the ambient flow in the problem of droplet deformation discussed in this thesis. From the view of the PDE itself, problems involving nonlinear terms in the governing PDEs are usually difficult to solve analytically, as are the Navier-Stokes equations from which the governing equations in Chapter 2 are derived.

A numerical method can be used to obtain an approximate solution when an analytical solution can not be developed. All numerical solutions produce values at discrete points for a set of the dependent variables, e.g. velocity, pressure etc. in problems in fluid dynamics. For a time dependent problem, the complete solution procedure is repeated at each time step. Numerical solutions, however, are much more desirable than no solution at all. The calculated values provide important information about the physical process, even though they are defined at discrete points.

There are several procedures for obtaining a numerical solution to a partial differential equation. The methods can be separated into three basic groupings: (1) the finite difference method, (2) variational methods and (3) methods that employ a weighted residual. Although the variational functional is the basis for many finite element formulations, it is usually applied to the problems in solid mechanics or heat transfer due to its disadvantage of not being applicable to any PDE containing a first derivative term, such as the Navier-Stokes in fluid dynamics. Therefore, it is not discussed here. The finite difference method approximates partial differential equations using difference approximations to derivative terms. These are based on Taylor series approximation and can be used to provide approximations of any order. This method is useful for solving benchmark heat transfer and fluid mechanics problems and works well for two-dimensional regions with boundaries

parallel to the coordinate axes. Nevertheless, the method is rather cumbersome when computational regions have curved or irregular boundaries.

As mentioned in Section 3.1, the numerical method used in this thesis is based on a spectral element approximation, which is a weighted residual method.

3.2.1 Weighted Residual Methods

The weighted residual method involves an integral of the partial differential equation to be solved, in which the dependent variables are substituted by an approximate solution to them. Since the approximate solution does not satisfy the equation, a residual or error term results. To explain this let us consider the Poisson equation

$$\nabla^2 \mathbf{u} + f = 0 \,. \tag{3.1}$$

This equation arises in many areas of physics such as irrotational fluid flow and steady state heat conduction, where u is velocity or temperature and f is a given function of the independent variables. In one-dimension equation (3.1) becomes

$$\frac{\partial^2 u}{\partial z^2} + f = 0 \,. \tag{3.2}$$

Suppose that $u = \hat{u}(z)$ is an approximate solution to the above equation, the substitution gives

$$\frac{\partial^2 \hat{u}}{\partial z^2} + f = R(z) \neq 0 \,, \tag{3.3}$$

Since $u = \hat{u}(z)$ does not satisfy the equation the weighted residual methods require that

$$\int_0^h R(z)\, w_i(z)\, dz = 0, \qquad 1 \leq i \leq N \,, \tag{3.4}$$

where $(0, h)$ is the domain of the computation. The residual $R(z)$ is multiplied by a weighting function $w_i(z)$, and the integral of the resulting product is required to be zero. Usually the number of the weighting functions, N, is equal to the number of unknown coefficients in the approximate solution. For instance, in a finite volume method, or say subdomain method (one of the most popular weighted residual scheme), $(0, h)$ is divided into N subintervals and each weighting function is selected as unity over a specific interval of the domain. The number of integration intervals equals the number of undetermined coefficients in the approximate solution as the coefficients may be represented by the node values between the subintervals.

One of the other methods in the family is the least squares method which utilizes the residual as the weighting function and obtains a new error form defined by

$$Er = \int_0^h [R(z)]^2 dz \ . \tag{3.5}$$

This error is minimized with respect to the unknown coefficients in the approximate solutions. The least squares methods looks reasonable mathematically and has been utilized to formulate finite element solutions, but it is not as popular as Galerkin's method for solving problems in fluid dynamics.

3.2.2 Galerkin's Method

Galerkin's method is one of the most useful weighted residual methods, which uses the same functions for the weighting or test functions $w(z)$ as those used in the trial space or basis used to represent the solution. This approach is the basis of the finite element method for problems involving first derivative terms and has been widely used to solve the partial differential equations in

fluid dynamics as well as other PDE problems. As the difference between SE and FE is mainly the way of the interpolation within the elements, the whole work in this thesis is based on the method.

3.2.2.1 Expansion of the Variables

In the Galerkin method, (3.4) becomes

$$\int_0^h \left(\frac{\partial^2 u}{\partial z^2} + f \right) \varphi \, dz = 0 \,, \tag{3.6}$$

where we use φ to represent the weighting or test function, which is the same as the function used to approximate u but may have different values on the boundaries. If linear interpolation for values of u between mesh nodes is considered, for example, for the approximate solution $\hat{u}$ of (3.6), then we have

$$\hat{u} = a_1 + a_2 z \,, \tag{3.7}$$

where the coefficients a_1 and a_2 are determined by using the nodal conditions:

$$u = \hat{u}_i \quad at \quad z = z_i \,,$$

$$u = \hat{u}_{i+1} \quad at \quad z = z_{i+1} \,.$$

obviously

$$\hat{u}_i = a_1 + a_2 z_i \,,$$

$$\hat{u}_{i+1} = a_1 + a_2 z_{i+1} \,, \tag{3.8}$$

from which we obtain

$$a_1 = \frac{\hat{u}_i z_{i+1} - \hat{u}_{i+1} z_i}{z_{i+1} - z_i} \,,$$

$$a_2 = \frac{\hat{u}_{i+1} - \hat{u}_i}{z_{i+1} - z_i} \,. \tag{3.9}$$

Substitution of (3.9) into (3.7) and rearranging gives

$$\hat{u}(z) = \left(\frac{z_{i+1} - z}{L}\right)\hat{u}_i + \left(\frac{z - z_i}{L}\right)\hat{u}_{i+1} , \tag{3.10}$$

where $z_{i+1} - z_i$ has been replaced by L. The linear functions which are multiplied by the nodal values are called shape functions and usually denoted by S with a subscript to indicate the node with which a specific shape function is associated. Therefore, equation (3.10) can be written as

$$\hat{u}(z) = S_i(z)\hat{u}_i + S_{i+1}(z)\hat{u}_{i+1}. \tag{3.11}$$

A continuous piecewise smooth approximate solution for a one dimensional domain can be constructed by connecting a number of linear approximations with the properties developed in the above. Each of these equations can be written as

$$\hat{u}_i^{el} = S_i^{el}\hat{u}_i^{el} + S_{i+1}^{el}\hat{u}_{i+1}^{el} , \tag{3.12}$$

where el is the element number, and

$$\begin{aligned} S_i^{el} &= \frac{z_{i+1} - z}{L} , \\ S_{i+1}^{el} &= \frac{z_i - z}{L} . \end{aligned} \tag{3.13}$$

The computational domain is defined as

$$z \in \Omega = \{ z \,|0 \leq z \leq h\} ,$$

here $z_0 = 0 < \cdots < z_i < z_{i+1} < \cdots < z_n = h$. Note that $el = i + 1$.

3.2.2.2 The Standard Element

The global expansion modes S_i^{el}, S_{i+1}^{el} discussed in the last subsection are typical local linear finite element basis functions when the elements are defined

between adjacent nodes with L representing the length of element. Each of the local basis functions takes a unit value, at one end of the element and decays linearly to zero across the element. However, to realise such a linear interpolation the global modes may be uneconomical as local coordinates are involved, particularly when using a large number of elements. We can see that, from the discussion in Section 3.2.2.2, both modes vary from 0 to 1 or from 1 to 0 at the element level. Therefore, if we introduce a standard element Ω_{st} such that

$$\Omega_{st} = \{ \xi \mid -1 < \xi < 1 \} \ ,$$

then the following linear functions, similar to the global modes, over Ω_{st} in terms of local coordinate ξ may be defined

$$\Phi_0(\xi) = \begin{cases} (1-\xi)/2 & \xi \in \Omega_{st} \\ 0 & otherwise \end{cases} \ ,$$

$$\Phi_1(\xi) = \begin{cases} (1+\xi)/2 & \xi \in \Omega_{st} \\ 0 & otherwise \end{cases} \ .$$

Thus, equation (3.12) may be written as

$$\hat{u}_i^{el} = \Phi_0 \, \hat{u}_i^{el} + \Phi_1 \, \hat{u}_{i+1}^{el} \ . \tag{3.14}$$

The standard element Ω_{st} can be mapped to any elemental domain

$$\Omega^{el} = \{ z \mid z_i \leq z \leq z_{i+1} \} \ ,$$

and the following transformation expresses the global coordinate z in terms of the local coordinate ξ as

$$z = \left(\frac{1-\xi}{2} \right) z_i + \left(\frac{1+\xi}{2} \right) z_{i+1} \ . \tag{3.15}$$

In this way, the nodal positions are not included in the expression for the global consideration, which is a significant simplification not only in solving PDEs numerically, but also in mapping a complex geometry in two or three dimensional calculations.

3.2.2.3 Weak Form of Galerkin Integral and its Numerical Approximation

We can see that equation (3.6) is equivalent to setting a weighted residual of the Poisson equation (3.2) to zero, so that the solution of (3.6) shall be an approximate solution of (3.2).

Integrating equation (3.6) by parts yields

$$\int_0^h \frac{\partial u}{\partial z}\frac{\partial \varphi}{\partial z}\,dz = \int_0^h f\varphi\,dz + \left[\frac{\partial u}{\partial z}\varphi\right]_0^h . \tag{3.16}$$

As the weight functions are required to be zero on the part of the boundary where essential or Dirichlet boundary condition are imposed (no weight is required here) we know that $\varphi(0) = \varphi(h) = 0$ in the above equation. Therefore, (3.16) becomes

$$\int_0^h \frac{\partial u}{\partial z}\frac{\partial \varphi}{\partial z}\,dz = \int_0^h f\varphi\,dz . \tag{3.17}$$

The integral form, as shown in equation (3.16) and (3.17), is referred to the weak form of the problem. Obviously the Galerkin approximation of the problem (3.2) is the solution to the weak form of equation (3.17) when the exact solution $u(z)$ is approximated by a finite expansion denoted by $\hat{u}(z)$. The function $\varphi(z)$ is also replaced by a finite expansion $\hat{\varphi}(z)$, so (3.17) becomes

$$\int_0^h \frac{\partial \hat{u}}{\partial z}\frac{\partial \hat{\varphi}}{\partial z}\,dz = \int_0^h f\hat{\varphi}\,dz . \tag{3.18}$$

The set of functions used in the finite expansion of the solution $\hat{u}$ are referred to as the trial functions whereas the functions contained within $\hat{\varphi}$ are called the test functions. Considering the linear expansion of $\hat{u}$ and $\hat{\varphi}$ as well as the integration on the standard element, equation (3.18) can be written as in the following

$$\sum_{el=1}^{N} \int_{-1}^{1} \frac{\partial \hat{u}(\xi)}{\partial \xi} \frac{\partial \hat{\varphi}(\xi)}{\partial \xi} \frac{d z}{d \xi} d \xi = \sum_{el=1}^{N} \int_{-1}^{1} f \hat{\varphi}(\xi) \frac{d z}{d \xi} d \xi . \tag{3.19}$$

After the integral operations and some matrix manipulations, (3.19) may yield a system of linear algebraic equations, which can be solved for the approximate and discrete solution $\hat{u}(\xi_i)\,(i = 0, \cdots, N)$, since we know $\hat{u}(\xi_0)$, $\hat{u}(\xi_N)$ through the boundary conditions.

This is a typical and classical finite element method. A spectral element scheme to solve the same equation may be created by simply replacing $\hat{u}$ and $\hat{\varphi}$ with spectral expansions involving Legendre polynomials, which will be discussed in next section.

3.3 One-dimensional Spatial Approximation

To increase the accuracy of approximate solutions of partial differential equations, such as Poisson's equation discussed in last section, quadratic or higher order polynomial basis functions may need to be used in the expansion of the dependent variables in the equations, in which more nodes on the grid are created and more nodal values need to be determined as shown in Fig. 3.1. This is the so-called p-type of the finite element method that has been widely investigated in last two or three decades. A shortcoming of this method is that its flexibility is limited due to the difficulties in programming when the polynomial order needs to be changed(I. Babaska and M. Suri, 1994).

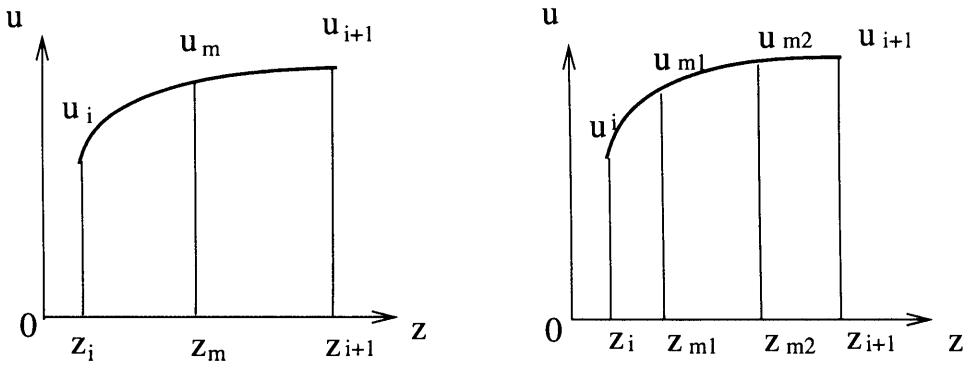

Figure 3.1: Nodes creation within a spectral element.

However, changing the polynomial order is relatively straightforward for a program coded for the spectral method, in which more flexible and easily manipulated p-type expansions are employed. This method has been extended to the spectral element method to deal with complex geometries for a wide range of numerical, experimental and industrial applications. Due to the fact that both the mesh structure and size and the polynomial order within the spectral elements can be easily changed, the method is also called the h/p finite element method, which will be discussed in detail in the context of this section.

3.3.1 Jacobi Polynomial

Beside the requirement of a universal formulation for different polynomial order p-type expansions in a spectral element scheme, it is advantageous to consider orthogonal polynomials when constructing an expansion. Such a polynomial forms a sparse mass matrix which can be easily inverted (Karniadakis and Sherwin, 1999) and makes the process of solution simpler and less costly. The most commonly used spectral expansions are based upon the orthogonal set called Jacobi polynomials. Although these expansions are

usually expressed in terms of the integral of Legendre polynomials (Oden 1992, Szabo and Babaska 1991), which is the special case, a more general description in terms of Jacobi polynomials ought to be considered as it more naturally extends to multi-dimensional cases.

Jacobi polynomials, usually denoted by $P_n^{\alpha\beta}(\xi)$, represent the family of polynomial solutions to a singular Sturm-Liouville problem which, in the region $(-1 < \xi < 1)$, is written as (Karniadakis and Sherwin, 1999)

$$\frac{d}{d\,\xi}\left\{(1\,-\,\xi)^{1+\alpha}\,(1\,+\,\xi)^{1+\beta}\,\frac{d}{d\,\xi}\,u_n(\xi)\right\} = \lambda_n(1-\xi)^{\alpha}(1-\xi)^{\beta}u_n(\xi)\,, \quad (3.20)$$

where n is the polynomial order and

$$u_n(\xi) \;=\; P_n^{\alpha\beta}(\xi)\;,$$

and

$$\lambda_n \;=\; -n(\alpha\,+\,\beta\,+\,n\,+\,1)\;.$$

An important property of these polynomials is the orthogonality relation

$$\int_{-1}^{1}(1\,-\,\xi)^{\alpha}\,(1\,-\,\xi)^{\beta}\,P_n^{\alpha\beta}(\xi)\,P_m^{\alpha\beta}(\xi)\,d\,\xi \;=\; C_n^{\alpha,\beta}\,\delta_{n\,m}\;. \quad (3.21)$$

where δ_{nm} represents the Kronecker delta, and $C_n^{\alpha,\beta}$, which depends on α, β and n, is given by

$$C_n^{\alpha,\beta} \;=\; \frac{2^{\alpha+\beta+1}}{(2\,+\,\alpha\,+\,\beta\,+\,1)}\;\frac{\Gamma(n+\alpha+1)\,\Gamma(n+\beta+1)}{n!\,\Gamma(n+\alpha+\beta+1)}\;. \quad (3.22)$$

This relation implies that $P_n^{\alpha\beta}(\xi)$ is orthogonal to all polynomials of order less than n with respect to the weight function $(1\,-\,\xi)^{\alpha}\,(1\,-\,\xi)^{\beta}$. These polynomials can be constructed using a three-term recursion relationship as shown in the next subsection.

Corresponding to the choice $\alpha = \beta$ the polynomials become symmetric and

known as ultraspherical polynomials. Well-known ultraspherical polynomials are Legendre polynomials ($\alpha = \beta = 0$) and Chebychev polynomials ($\alpha = \beta = \frac{1}{2}$). The latter were widely used in the early development of the spectral methods, whereas the former have been mostly used in recent years and will be discussed in the next few subsections.

3.3.2 Legendre Polynomials

The Legendre polynomials can be expressed in a recursion form as (Karniadakis and Sherwin, Appendix A, 1999)

$$L_0(\xi) = P_0^{0,0}(\xi) = 1 , \qquad L_1(\xi) = P_1^{0,0}(\xi) = \xi ,$$

$$L_{n+1}(\xi) = P_{n+1}^{0,0}(\xi) = [(a_n^2 + a_n^3)/a_n^1]L_n(\xi) - (a_n^4/a_n^1)L_{n-1}(\xi),$$

where

$$a_n^1 = 4n(n+1)^2 , \qquad a_n^1 = 0 ,$$

$$a_n^3 = 4n(2n+1)(n+1) , \qquad a_n^4 = 4(n+1)n^2 .$$

Some of its advantages in numerical formulation are given as follows.

3.3.2.1 The Orthogonality

By the definition of equation (3.21), the orthogonality of Legendre polynomials reduces to the Legendre inner product

$$(L_n(\xi), L_m(\xi)) = \int_{-1}^{1} L_n(\xi)\, L_m(\xi)\, d\,\xi = \frac{2}{2n\ +\ 1}\, \delta_{n,m} , \qquad (3.23)$$

where the polynomial order, $0 \leq n, m \leq N$.

This simple form has very important implications for the Galerkin method using spectral elements, some of them are shown in the following sections. Another advantage is that the Legendre polynomials are orthogonal on $(-1, 1)$

with respect to the unit weight function $w(z) = 1$, which also makes it convenient for finite volume methods to incorporate the interpolations based on Legendre polynomials.

3.3.2.2 The Mass Matrix

Let us consider the Galerkin projection of a smooth function $f(\xi)$ in the domain Ω_{st} onto the polynomial expansion $\hat{u}(\xi)$, which may be expressed as the problem

$$(\hat{\varphi},\, \hat{u}) \;=\; (\hat{\varphi},\, f)\;, \tag{3.24}$$

where the brackets mean the inner product in the absence of explicit boundaries, which need not be prescribed to obtain a solution, or say that Dirichlet condition is implied. To find $\hat{u}(\xi)$, letting

$$\hat{u}(\xi) \;=\; \sum_{n=0}^{N} \hat{u}_n\, L_n(\xi) \qquad \hat{\varphi}(\xi) \;=\; L_m(\xi)\;,$$

i.e. the Legendre polynomial is used in the expansions for both trial and test functions, then problem (3.24) is equivalent to solving the matrix equation

$$M\hat{u} \;=\; f\;,$$

where

$$M_{m,n} \;=\; (L_n, (\xi)\, L_m(\xi)) \;=\; \int_{-1}^{1} L_n(\xi)\, L_m(\xi)\, d\,\xi \;=\; \frac{2}{2n \,+\, 1}\, \delta_{n,m}\;,$$

here

$$\hat{u} \;=\; [\hat{u_0},\, \cdots\, \hat{u_N}]^T\;,$$

$$f_n \;=\; (L_n(\xi),\, f)\;.$$

The matrix M, known as the mass matrix, is diagonal, and can be inverted to determine the solution

$$\hat{u} \;=\; M^{-1}\, f\;.$$

Obviously M^{-1} is also diagonal. The Legendre mass matrix is very easy to construct, invert and numerically efficient, specially when comparing with the mass matrices of some other expansions such as moment expansion, the mass matrix of which has components of the form

$$M_{n\,m} = \int_{-1}^{1} \xi^n \xi^m \, d\xi = \begin{cases} 2/(n+m+1) & n+m \quad even \\ 0 & n+m \quad odd \end{cases} .$$

The Legendre polynomials also make inner products of first order derivatives such as

$$\left(\frac{d\,\hat{u}}{d\,\xi}, \frac{d\,\hat{\varphi}}{d\,\xi} \right)$$

easier and more efficient to calculate. This will be discussed later in this chapter.

3.3.3 Nodal P-type Expansions

The polynomials discussed previously are modal p-type expansions which have a few disadvantages when used to solve differential equations.

At first, there is an inner mesh within a spectral element but the approximate solutions on the mesh nodes are not directly evaluated except for that at elemental boundaries. This is inconvenient. Secondly, the basis cannot be extended to an elemental decomposition which is globally C^0 continuous since the continuity constraints destroy the orthogonality of the global matrix structure. For instance, we may define a modal expansion with the Legendre polynomial, in which the test or trial functions are

$$\varphi_n = \begin{cases} (1 - \xi)/2 & n = 0 \\ (1 - \xi)(1 + \xi)/4 & 0 < n < N \\ (1 + \xi)/2 & n = N \end{cases} \tag{3.25}$$

to ensure C^0 continuity on elemental boundaries. In compensation its mass matrix $M = (\varphi_n , \varphi_m)$ is no longer diagonal.

On the other hand, nodal p-type basis such as Lagrange polynomials

$$h^n(\xi) = \left(\prod_{m=0(m\neq n)}^{N} (\xi - \xi_m) \right) / \left(\prod_{m=0(m\neq n)}^{N} (\xi_n - \xi_m) \right)$$

already satisfied the C^0 condition as

$$h^n(\xi_m) = \delta_{nm} .$$

This must include the nodes on the boundaries. The nodal interpolation also means that the coefficients in the expansions, as unknowns to be solved, are the approximate solutions on the mesh nodes. Nevertheless, there is no explicit form for its mass matrix and the matrix is full.

If we denotes by $g(\xi)$ the polynomial of order N with zeros at the $(N + 1)$ nodal points ξ_m, $0 \leq m \leq N$, i.e.

$$g(\xi) = \prod_{m=0}^{N} (\xi - \xi_m) ,$$

then obviously we have

$$\frac{g(\xi)}{\xi - \xi_n} = \prod_{m=0(m\neq n)}^{N} (\xi - \xi_m) ,$$

so that

$$g'(\xi) = \sum_{n=0}^{N} \prod_{m=0(m\neq n)}^{N} (\xi - \xi_m) ,$$

or

$$g'(\xi_n) = \prod_{m=0(m\neq n)}^{N} (\xi_n - \xi_m) ,$$

Then we can write $h_n(\xi)$ in a more compact form as

$$h_n(\xi) = \frac{g(\xi)}{g'(\xi)\,(\xi - \xi_n)} . \tag{3.26}$$

Furthermore, let

$$g(\xi) = (1-\xi)(1+\xi)L'_N(\xi) .$$

This is called Gauss-Lobatto-Legendre interpolatory polynomial, at the roots of which $(N+1)$ nodal values are given. Substituting this into equation (3.26), we obtain the following nodal p-type expansion for the standard element Ω_{st}

$$h_n(\xi) = \frac{(1-\xi)(1+\xi)L'_N(\xi)}{N(N+1)L_N(\xi_n)(\xi - \xi_n)} , \tag{3.27}$$

where we have used equation (3.20) to deduce and get

$$g'(\xi) = -N(N+1)L_N(\xi) .$$

The derivative of the Legendre polynomial $L'_n(\xi)$ can be related to the Jacobi polynomial $P^{1,1}_{N-1}(\xi)$ (Karniadakis and Sherwin 1999, appendix A). Therefore, we may also consider the spectral element basis as a Lagrange polynomial with the nodal points at the roots of the polynomial

$$g(\xi) = (1-\xi)(1+\xi)P^{1,1}_{N-1}(\xi) .$$

The roots of $g(\xi)$ are known as the Gauss-Lobatto points.

The elemental mass matrix using $h_i(\xi)$ as the expansion or basic function is

still full when we evaluate the product $M_{nm} = (h_n(\xi),\ h_m(\xi))$ exactly. If, however, we use the Gauss-Lobatto-Legendre quadrature rule (see Section 3.3.4) corresponding to the same choice of nodal points on which the expansion $h_n(\xi)$ was defined, the mass matrix is diagonal due to the Kronecker delta property, i.e.

$$M_{nm} = (h_n,\ h_m) = \sum_{i=0}^{N} w_i\, h_n(\xi_i)\, h_m(\xi_i) = \sum_{i=0}^{N} w_i\, \delta_{ni}\delta_{mi} = w_n\, \delta_{mn}\ ,$$

where

$$w_i = \int_{-1}^{1} h_i(\xi)\, d\,\xi = \int_{-1}^{1} \left[\frac{(1-\xi)(1+\xi)L'_N(\xi)}{N(N+1)L_N(\xi_i)(\xi\ -\ \xi_i)}\right] d\,\xi$$

are the weights for the Gauss-Legendre-Lobatto rule using the $(N+1)$ nodal points.

Until now, we can see the modified Lagrange polynomial $h_n(\xi)$ shown in equation (3.27) has all the advantages such as constructed by Legendre polynomials, which are relatively easier in manipulation and efficient in calculation; continuous on the boundaries of elemental decomposition; and resulting in a diagonal mass matrix in numerical approximation. These have made it widely used and the nodal p-type elements have become known as spectral elements since 1980s (Patera 1984, Karniadakis 1985 and 1999). This polynomial expansion has been used throughout this thesis.

3.3.4 Differentiation and Gauss-Lobatto-Legendre Integral

Differentiating and integrating spectral expansions in terms of basis function (3.27) are necessary to discretize the weak formulation of PDEs to be solved. If we assume that $\hat{u}(\xi)$ is a polynomial of degree equal or less than N, then it can be exactly expressed in terms of Lagrange polynomials $h_i(\xi)$, discussed in subsection 3.3.3, through the $(N+1)$ Gauss-Lobatto nodal points ξ_i $(0 \leq i \leq N)$ as

$$\hat{u}(\xi) = \sum_{i=0}^{N} \hat{u}(\xi_i)\, h_i(\xi) \,. \tag{3.28}$$

Therefore the derivative of $\hat{u}(\xi)$ can be represented as

$$\hat{u}'(\xi) = \sum_{i=0}^{N} \hat{u}(\xi_i)\, h_i'(\xi) \,.$$

Typically we only require the derivative at the nodal points ξ_j which is given by

$$\left(\frac{d\,\hat{u}(\xi)}{d\,\xi}\right)_{\xi=\xi_j} = \sum_{i=0}^{N} d_{ji}\, u(\xi_i)$$

where $d_{ij} = \left(\frac{d\,h_j(\xi)}{d\,\xi}\right)_{\xi=\xi_i}$ can be found to be (Karniadakis and Sherwin 1999)

$$d_{ij} = \begin{cases} -N(N+1)/4 & i = j = 0 \\ L_N(\xi_i)/\left(L_N(\xi_j)(\xi_i - \xi_j)\right) & i \neq j,\ 0 \leq i,j \leq N \\ 0 & 1 \leq i = j \leq N-1 \\ N(N+1)/4 & i = j = N \end{cases}, \tag{3.29}$$

and

$$\xi_i = \begin{cases} -1 & i = 0 \\ \xi^{1,1}_{i-1,N-1} & i = 1, \cdots, N-1 \\ 1 & i = N \end{cases} .$$

The matrix D is known as the Gauss-Lobatto-Legendre differentiation matrix, and here $\xi^{1,1}_{i-1,N-1}$, $i = 1, \cdots, N-1$ are the inner Gauss-Lobatto points which can be obtained by solving

$$(1-\xi)(1+\xi)P^{1,1}_{N-1}(\xi) \;=\; 0$$

The Gauss-Lobatto-Legendre quadrature rule used to evaluate the integrals in the weak form of partial differential equations is defined as

$$\int_{-1}^{1} \hat{u}(\xi)\, d\xi \;\approx\; \sum_{i=0}^{N} w_i\, \hat{u}(\xi_i)\;,$$

with equality when $\hat{u}$ is a polynomial of degree $2N-1$ or less. The numerical weights w_i, $0 \leq i \leq N$, are calculated as the integral of the Lagrange polynomials, shown in section 3.3.3. This yields (Canuto et al, 1987)

$$w_i \;=\; \int_{-1}^{1} \hat{u}(\xi)\, d\xi \;=\; \frac{2}{N(N+1)\left[L_N(\xi_i)\right]^2} \tag{3.30}$$

where ξ_i, $0 \leq i \leq N$, are the Gauss-Lobatto points given in equation (3.29).

3.4 Axisymmetric Discretization

3.4.1 Two-dimensional Expansions

As the droplet concerned is assumed to be axisymmetric in shape in the process of deformation, the expansion basis discussed in previous sections needs to be extended to two and half dimensions. Since, in an axisymmetric domain, the dependent variables in PDEs such as $u \;=\; u(z,r)$ in equation (3.1) are independent of the angular variable θ, only two-dimensional expansions are considered, but note that the governing momentum equations for axisymmetric case are more complicated than that in the planar case.

The two-dimensional basis is, in general, denoted by $\varphi_{pq}(\xi,\eta)$ where ξ, η are

the Cartesian coordinates in the computational domain on the standard element. This notation may equally well refer to a modal or nodal expansion within triangular or quadrilateral standard elements, although our interest is only in nodal expansions within quadrilateral elements.

There is a wide variety of expansion bases, particularly in the standard h-type finite element method, but our attention is only to those most commonly used in the spectral/hp element literature, which may be expressed in terms of a tensor product of one-dimensional expansions, that is

$$\varphi_{pq}(\xi,\eta) \;=\; \varphi_p(\xi)\,\varphi_q(\eta)\;.$$

and we choose

$$\varphi_p(\xi) \;=\; h_p(\xi) \qquad \varphi_q(\eta) \;=\; h_q(\eta)\;.$$

Therefore, the approximation, or say discretization, of the variable u in equation (3.1) may be written as

$$u(\xi,\eta) \;=\; \sum_{p=0}^{N}\sum_{q=0}^{N} \hat{u}_{pq}\, h_p(\xi)\, h_q(\eta)\;,$$

where N is the polynomial order. One of the most useful advantages of these expansion bases is the simplification of differentiation such as

$$\frac{du}{d\xi} \;=\; \sum_{p=0}^{N}\sum_{q=0}^{N} \hat{u}_{pq}\, h_p^{'}(\xi)\, h_q(\eta)\;.$$

And the Gauss-Lobatto-Legendre integral of the expansion may be also simply calculated using

$$\int_{\Omega_{st}} h_p(\xi)h_q(\eta)\,d\xi d\eta \;=\; \sum_{i=0}^{N}\sum_{j=0}^{N} h_p(\xi_i)h_q(\xi_j)\,w_i w_j \;=\; w_p w_q\;.$$

Expansions of the above form allow many numerical operations to be per-

formed very efficiently using the sum factorization technique, this will be discussed in the later part of this chapter. Specifically, the nodal interpolation

$$\varphi_{pq}(\xi,\eta) \;=\; h_p(\xi)\, h_q(\eta)$$

implies that on elemental boundaries the expansion reduces to a one dimensional function.

3.4.2 Structured Domains

Structured domains are used for the calculations in this research. As mentioned previously the word 'structured' implies here a quadrilateral in two dimensions or in axisymmetric domains with conforming adjacent edges of spectral elements. Thus, the spatial discretization of the physical domain Ω of a certain geometry involves dividing, Ω, into K non-overlapping spectral elements Ω_{el} with

$$\bigcup_{el=1}^{K} \Omega_{el} \;=\; \Omega$$

where $1 \leq el \leq K$. This provides greater freedom in creating meshes for calculations in complex geometries and also allows for higher mesh resolution in flow regions where high gradients may occur, which is the h-type characteristic of the spectral element method. The interpolations in nodal methods are defined on the computational unit square

$$\Omega_{st} \;=\; \{-1 \leq \xi,\eta \leq 1\} \;,$$

where each point (ξ,η) is associated with a point $\vec{x} = (z,r) \in \Omega_{el}$. So a projection between Ω_{st} and Ω_{el} is required. A few mapping methods to mesh a spectral element used in the research will be discussed in Section 3.4.3 .

3.4.3 The Mapping Method

3.4.3.1 Linear Transfinite Mapping

For an arbitrary straight-sided elemental domain as shown in Fig 3.2, where s and t represent the coordinates ξ and η in the computational space repectively, a one-to-one linear mapping onto the standard element Ω_{st} can be expressed by

$$\begin{aligned}\vec{x} &= T(\xi,\eta) \\ &= f^A(\xi)\Phi_1(\eta) + f^B(\eta)\Phi_2(\xi) + f^C(\xi)\Phi_2(\eta) + f^D(\eta)\Phi_1(\xi) \\ &\quad - \Phi_1(\xi)\Phi_1(\eta)f^A(-1) - \Phi_2(\xi)\Phi_1(\eta)f^A(1) \\ &\quad - \Phi_1(\xi)\Phi_2(\eta)f^C(-1) - \Phi_2(\xi)\Phi_2(\eta)f^C(1) \ , \end{aligned} \tag{3.31}$$

where $f^A(\xi)$, $f^B(\eta)$, $f^C(\xi)$, $f^D(\eta)$ are physical quadrilateral element boundaries which can be expressed as

$$f^A(\xi) = \vec{x}(\xi,-1) \ , \quad f^C(\xi) = \vec{x}(\xi,1) \ ,$$

$$f^B(\eta) = \vec{x}(1,\eta) \ , \quad f^D(\eta) = \vec{x}(-1,\eta) \ .$$

Here

$$\vec{x} = (z(\xi,\eta), r(\xi,\eta)) \ ,$$

in which the coordinates are $\vec{x}_2 = f^A(1) = f^B(-1)$, $\vec{x}_4 = f^C(-1) = f^D(1)$ etc. The basis functions are defined by

$$\Phi_1(\xi) = \frac{1-\xi}{2} \ , \quad \Phi_2(\eta) = \frac{1+\eta}{2} \ . \tag{3.32}$$

If $f^A(\xi)$, $f^B(\eta)$, $f^C(\xi)$, $f^D(\eta)$ are all linear functions, for instance

$$f^A(\xi) = \vec{x}_1\frac{(1-\eta)}{2} + \vec{x}_2\frac{(1+\xi)}{2} \ ,$$

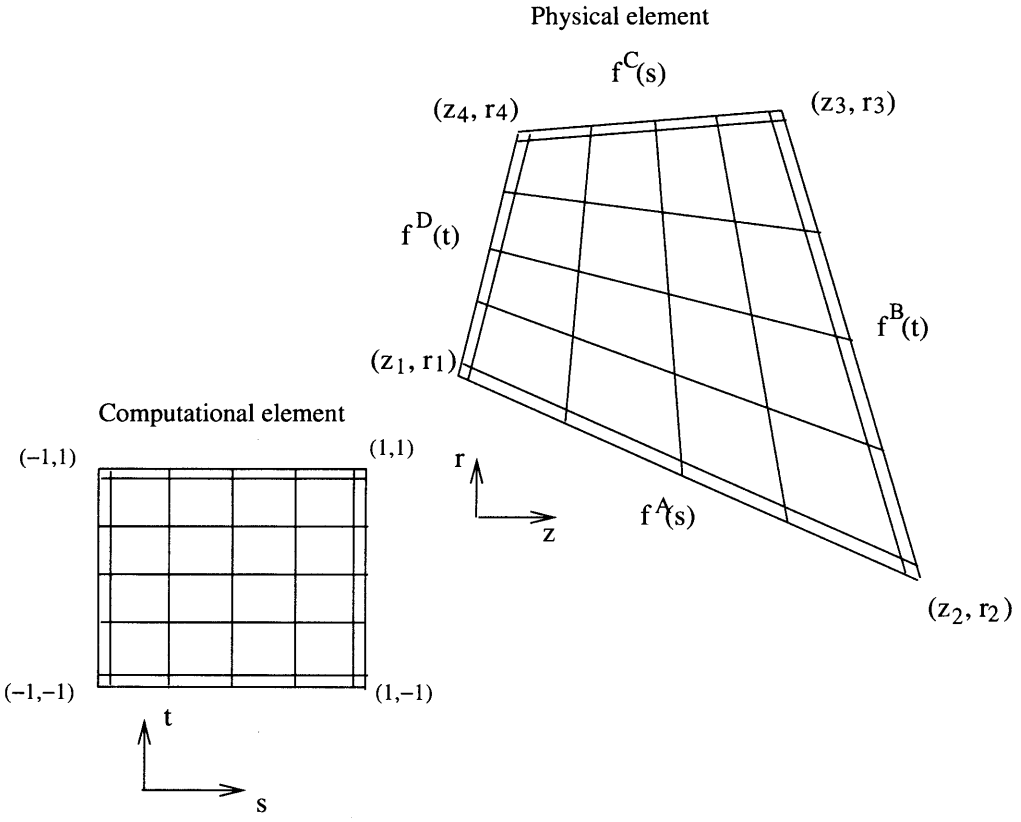

Figure 3.2: The standard (computational) element Ω_{st} in the computational space and the spectral element Ω_{el} in the physical space

the mapping is the bi-linear transfinite mapping $T_{1,1}$ (Gordon and Hall 1973, Gordon and Thiel 1982). Higher order transfinite mapping $T_{a,b}$ may also be defined, where a and b denote the highest order on the physical boundaries $f^A(\xi)$, $f^C(\xi)$ and $f^B(\eta)$, $f^D(\eta)$ respectively, see Schneidesch and Deville 1993. Only $T_{1,1}$ is used in this thesis.

3.4.3.2 Isoparametric Mapping

The linear transfinite mapping discussed in last section may also be expressed as

$$\begin{aligned}\vec{x} \;=\; & \vec{x}_1 \frac{(1-\xi)}{2}\frac{(1-\eta)}{2} \;+\; \vec{x}_2 \frac{(1+\xi)}{2}\frac{(1-\eta)}{2} \\ & + \vec{x}_4 \frac{(1-\xi)}{2}\frac{(1+\eta)}{2} \;+\; \vec{x}_3 \frac{(1+\xi)}{2}\frac{(1+\eta)}{2} \;. \end{aligned} \tag{3.33}$$

We note that this simply involves the vertex modes of a hierarchical modal expansion basis within a quadrilateral region. So, for axisymmetric cases we may write this expansion as

$$x^i(\xi,\eta) \;=\; \sum_{p=0}^{N}\sum_{q=0}^{N} \hat{x}^i_{pq}\, \varphi_{pq}(\xi,\eta) \;,$$

where $i = r, z$ and $\hat{x}_{pq}$ represents the vertex coordinates. Obviously

$$(\hat{z}_{00}, \hat{r}_{00}) \;=\; \vec{x}_1 \;,$$

$$(\hat{z}_{N0}, \hat{r}_{N0}) \;=\; \vec{x}_2 \;,$$

$$(\hat{z}_{NN}, \hat{r}_{NN}) \;=\; \vec{x}_3 \;,$$

$$(\hat{z}_{0N}, \hat{r}_{0N}) \;=\; \vec{x}_4 \;.$$

Thus, it can be clearly seen from the above that we only need to know the values of the vertex locations $\hat{x}_{pq}$ for the mapping to be constructed. However, to describe a curved region we would normally expect to be given the shape

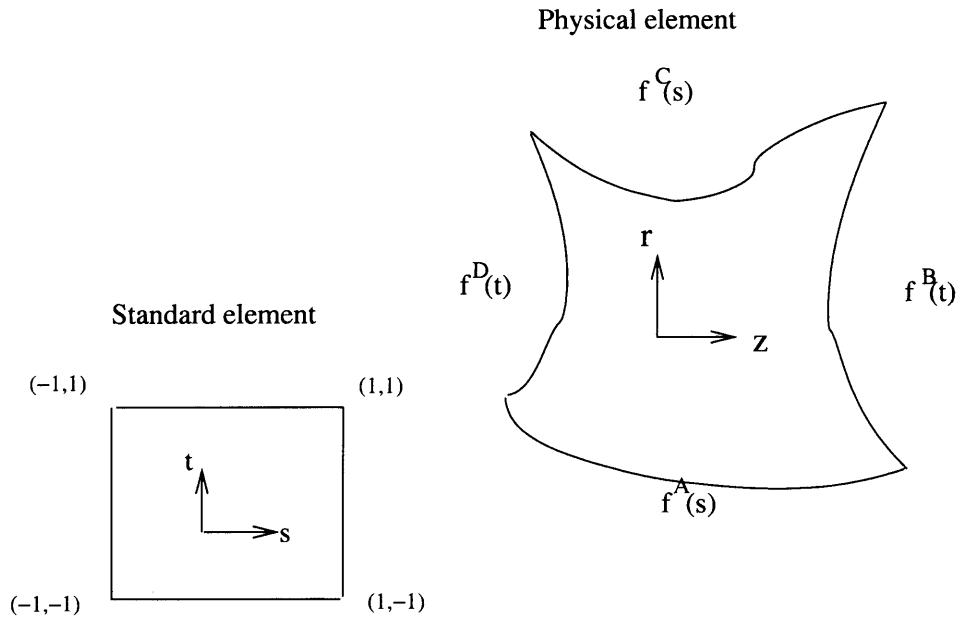

Figure 3.3: Physical and computational domains for the isoparametric mapping, s and t represent ξ and η respectively

of each edge in terms of series of parametric functions, which we may define as $f_i^A(\xi)$, $f_i^B(\eta)$, $f_i^C(\xi)$, $f_i^D(\eta)$, as shown in Fig 3.3.

If the expansions, which are the same as those used for the unknowns in the partial differential equations to be solved, are applied to the parametric functions, i.e.

$$f_i^A(\xi) = \sum_{p=0}^{N} \hat{x}_{p0}^i \varphi_p(\xi) ,$$

and

$$f_i^B(\eta) = \sum_{q=0}^{N} \hat{x}_{Nq}^i \varphi_q(\eta) , \tag{3.34}$$

we may construct an isoparametric mapping relating the standard region (ξ, η) to the curved quadrilateral region as follows

$$x^i(\xi, \eta) = \sum_{p=0}^{N} \sum_{q=0}^{N} \hat{x}_{pq}^i \, \varphi_p(\xi) \, \varphi_q(\eta) , \tag{3.35}$$

where $\hat{x}_{p0}^i$ are found as an analytic function of higher order (for modal type interpolation) or a set of given values for a subgrid boundary nodes in nodal type expansion. The inner coefficients $\hat{x}_{pq}^i$ ($0 < p , q < N$) need to be created or interpolated between the four boundaries.

It should be noted that $\hat{x}_{p0}^i$, $\hat{x}_{qN}^i$ etc., in (3.34) are found from a boundary transformation which ensures that the coordinates remain continuous at the vertices in order to obtain a C^0 continuous representation. The mapping from (ξ, η) to (z, r) is then determined by equation (3.35).

Replacing $\varphi_p(\xi)$, $\varphi_q(\eta)$ in equations (3.34) and (3.35) with the nodal type expansions $h_p(\xi)$, $h_q(\eta)$, we have

$$x^i(\xi, \eta) = \sum_{p=0}^{N} \sum_{q=0}^{N} \hat{x}_{pq}^i h_p(\xi) h_q(\eta) . \tag{3.36}$$

One may see that the elemental boundaries are curves interpolating the nodal values $\hat{x}^i_{p0}$, $\hat{x}^i_{Nq}$ etc., which makes the transformation between computational and physical domains more accurate. For further details of isoparametric mapping see Viggo (1980).

3.4.3.3 Mixed Mapping

In most practical applications, only one edge (or surface in three-dimensions) in a 2-D element is typically curved. For straight-sided edges the transformation between (ξ, η) and (z, r) will simply reduce to vertex contribution. As an example, Fig. 3.4 is a physical domain to simulate a flow of a deforming liquid droplet in an axial gas current, the deformation is assumed to be axisymmetric.

As we can see from the Fig. 3.4 the spectral elements around the droplet boundary have only one curved edge while the other three are straight-sided. The curve which determines the shape of the drop and hence the location of the interface between the phases must be determined accurately, whereas the decomposition of the other part of the domain can be performed with flexibility. Therefore, the quadrilateral expansion in equation (3.35) may be replaced using a linear blending function originally proposed by Gordon and Hall (1973), which is given by

$$\begin{aligned}\vec{x} = {} & f^A(\xi)\frac{(1-\eta)}{2} + f^C(\xi)\frac{(1+\eta)}{2} + f^D(\eta)\frac{(1-\xi)}{2} + f^B(\eta)\frac{(1+\xi)}{2} \\ & - \frac{(1-\xi)}{2}\frac{(1-\eta)}{2}f^A(-1) - \frac{(1+\xi)}{2}\frac{(1-\eta)}{2}f^A(1) \\ & - \frac{(1-\xi)}{2}\frac{(1+\eta)}{2}f^C(-1) - \frac{(1+\xi)}{2}\frac{(1-\eta)}{2}f^C(1)\,, \end{aligned} \tag{3.37}$$

where continuity at the vertex points mean that $f^A(-1) = f^B(-1)$ etc.

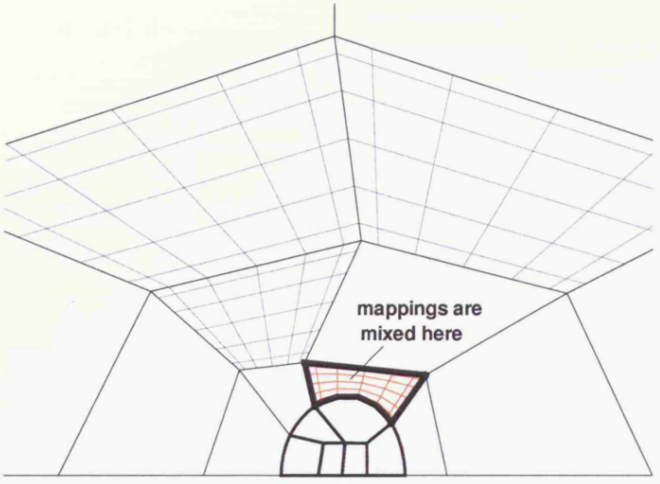

Figure 3.4: Blended transfinite and isoparametric mapping.

The above equation is of a similar form as equation (3.31) but one of $f^A(\xi)$, $f^B(\eta)$, $f^C(\xi)$, $f^D(\eta)$ may be analytical functions to represent elemental boundary curves. If we replace the analytical curves with the approximate expansion of the type given in (3.34) and rearrange we may obtain an expansion of the form given by equation (3.35).

Equation (3.37) is a mapping function that has been used in the spectral element method. When the nodal type basis such as Lagrange polynomial $h_p(\xi)$ is applied, for instance

$$f_i^A(\xi) \;=\; \sum_{p=0}^{N} \hat{x}_{p0}^i h_p(\xi) \;,$$

the mesh nodes on element boundaries can be exactly interpolated. This characteristic is useful in moving boundary problems.

3.5 Discretization of the Continuity Equation

With the mixed mapping method and the Lagrange polynomials used as the trial and test functions, discussed in last section, the weak form of the conservation of mass equation (2.19) may be transformed from the physical space to computational space and given as

$$\begin{aligned}\int_{\Omega_{el}(t)} \left\{ \frac{\partial u(z,r)}{\partial z} + \frac{\partial v(z,r)}{\partial r} + \frac{v(z,r)}{r} \right\} q(z,r)\, r dr dz \\ = \int_{\Omega_{st}(t)} \left\{ \frac{\partial u(\xi,\eta)}{\partial z} + \frac{\partial v(\xi,\eta)}{\partial r} + \frac{v(\xi,\eta)}{r(\xi,\eta)} \right\} \\ q(\xi,\eta)\, r(\xi,\eta)\; |J|\, d\xi\, d\eta \;=\; 0 \;, \qquad (3.38)\end{aligned}$$

where Ω_{el} is the physical domain of a spectral element, $q(\xi,\eta)$ represents the discrete pressure test functions, and J is the Jacobian of the transformation from the global co-ordinates to the computational space, which may be

expressed as

$$J = \frac{\partial z}{\partial \xi}\frac{\partial r}{\partial \eta} - \frac{\partial z}{\partial \eta}\frac{\partial r}{\partial \xi} .$$

From the Jacobian, it can also be found that

$$\frac{\partial}{\partial z} = \frac{1}{J}\left(\frac{\partial r}{\partial \eta}\frac{\partial}{\partial \xi} - \frac{\partial r}{\partial \xi}\frac{\partial}{\partial \eta}\right) ,$$

and

$$\frac{\partial}{\partial r} = \frac{1}{J}\left(\frac{\partial z}{\partial \xi}\frac{\partial}{\partial \eta} - \frac{\partial z}{\partial \eta}\frac{\partial}{\partial \xi}\right) ,$$

The integral over the parent element Ω_{st} from (3.38) can now be expressed as

$$\int_{\Omega_{st}(t)} \left[\left(\frac{\partial r}{\partial \eta}\frac{\partial}{\partial \xi} - \frac{\partial r}{\partial \xi}\frac{\partial}{\partial \eta}\right) u(\xi,\eta) + \left(\frac{\partial z}{\partial \xi}\frac{\partial}{\partial \eta} - \frac{\partial z}{\partial \eta}\frac{\partial}{\partial \xi}\right) v(\xi,\eta)\right]$$
$$q(\xi,\eta) r \frac{|J|}{J} d\xi d\eta$$
$$+ \int_{\Omega_{st}(t)} v(\xi,\eta) q(\xi,\eta)\, |J|\, d\xi d\eta . \qquad (3.39)$$

The mapping factors $\partial z/\partial \xi$, $\partial z/\partial \eta$, $\partial r/\partial \xi$ *and* $\partial r/\partial \eta$ are determined by the mixed mapping operator (3.37).

The spectral approximation in an element Ω_{el} of the velocity and pressure are given by

$$\mathbf{u}(\xi,\eta) = \sum_{i=0}^{N}\sum_{j=0}^{N} \mathbf{u}_{i,j} h_i(\xi) h_j(\eta) , \qquad (3.40)$$

$$p(\xi,\eta) = \sum_{j=1}^{N-1}\sum_{j=1}^{N-1} p_{i,j} \widetilde{h}_i(\xi) \widetilde{h}_j(\eta) , \qquad (3.41)$$

where $\mathbf{u} = (u, v)$, and the hats above the variables to represent the approximate solutions have been withdrawn for convenience. The Lagrangian interpolatants, based on Legendre polynomials of degree $N-2$ in both spatial directions, $\widetilde{h}_i(\xi)$ are defined as

$$\widetilde{h}_i(\xi) = \frac{(1-\xi_i^2)L'_N(\xi)}{N(N+1)L_N(\xi_i)(\xi - \xi_i)} , \tag{3.42}$$

here $1 \leq i \leq N-1$. This choice of the Lagrangian interpolatants $\widetilde{h}_i(\xi)$ ensures that the discrete pressure nodes are the internal collocation points in the Gauss-Lobatto-Legendre grid. Here the pressure treatment is slightly different from the velocity (for the details see chapter 4).

Substituting these spectral approximations into the weak formulation of the continuity equation on the the parent element, (3.40) yields for the first term

$$\int_{\Omega_{st}(t)} \left[\left(\frac{\partial r}{\partial \eta}\frac{\partial}{\partial \xi} - \frac{\partial r}{\partial \xi}\frac{\partial}{\partial \eta} \right) \sum_{i=0}^{N}\sum_{j=0}^{N} u_{i,j} h_i(\xi) h_j(\eta) \right] q(\xi,\eta) r \frac{|J|}{J} d\xi d\eta \tag{3.43}$$

Then, the approximate continuity equation can be written as

$$\begin{aligned}
&\int_{\Omega_{st}(t)} \left[\frac{\partial r}{\partial \eta} \sum_{i=0}^{N}\sum_{j=0}^{N} u_{i,j} h_i'(\xi) h_j(\eta) - \frac{\partial r}{\partial \xi} \sum_{i=0}^{N}\sum_{j=0}^{N} u_{i,j} h_i(\xi) h_j'(\eta) \right] \\
&\qquad \widetilde{h}_k(\xi)\widetilde{h}_l(\eta) r \frac{|J|}{J} d\xi d\eta \\
&+ \int_{\Omega_{st}(t)} \left[\frac{\partial z}{\partial \xi} \sum_{i=0}^{N}\sum_{j=0}^{N} v_{i,j} h_i(\xi) h_j'(\eta) - \frac{\partial z}{\partial \eta} \sum_{i=0}^{N}\sum_{j=0}^{N} v_{i,j} h_i'(\xi) h_j(\eta) \right] \\
&\qquad \widetilde{h}_k(\xi)\widetilde{h}_l(\eta) r \frac{|J|}{J} d\xi d\eta \\
&+ \int_{\Omega_{st}(t)} \left[\sum_{i=0}^{N}\sum_{j=0}^{N} v_{i,j} h_i(\xi) h_j(\eta) \right] \widetilde{h}_k(\xi)\widetilde{h}_l(\eta) \, |J| \, d\xi d\eta = 0 ,
\end{aligned} \tag{3.44}$$

where the pressure test functions are also based on the Lagrangian interpolants

$$q(\xi,\eta) \;=\; \widetilde{h}_k(\xi)\widetilde{h}_l(\eta)\;. \tag{3.45}$$

The discrete equation for a single inner collocation point (k,l) of the element can be obtained by carrying out the Gauss-Lobatto-Legendre integration. So the first term of the above equation is approximated as

$$\sum_{p=0}^{N}\sum_{q=0}^{N}\frac{\partial r}{\partial \eta}_{pq}\sum_{i=0}^{N}\sum_{j=0}^{N}u_{i,j}h_i^{'}(\xi_p)h_j(\eta_q)\widetilde{h}_k(\xi_p)\widetilde{h}_l(\eta_q)r(\xi_p,\eta_q)\frac{|J_{pq}|}{J_{pq}}w_pw_q\;-$$

$$\sum_{p=0}^{N}\sum_{q=0}^{N}\frac{\partial r}{\partial \xi}_{pq}\sum_{i=0}^{N}\sum_{j=0}^{N}u_{i,j}h_i(\xi_p)h_j^{'}(\eta_q)\widetilde{h}_k(\xi_p)\widetilde{h}_l(\eta_q)r(\xi_p,\eta_q)\frac{|J_{pq}|}{J_{pq}}w_pw_q\;. \tag{3.46}$$

This can be expressed as matrix vector products

$$D_{z\xi}\mathbf{u}_z + D_{z\eta}\mathbf{u}_z$$

$$= \begin{pmatrix} d^{z\xi}_{11,00} & \cdots & d^{z\xi}_{11,ij} & \cdots & d^{z\xi}_{11,NN} \\ \cdot & \cdots & \cdot & \cdots & \cdot \\ \cdot & \cdots & \cdot & \cdots & \cdot \\ d^{z\xi}_{kl,00} & \cdots & d^{z\xi}_{kl,ij} & \cdots & d^{z\xi}_{kl,NN} \\ \cdot & \cdots & \cdot & \cdots & \cdot \\ \cdot & \cdots & \cdot & \cdots & \cdot \\ d^{z\xi}_{(N-1)(N-1),00} & \cdots & d^{z\xi}_{(N-2)(N-1),ij} & \cdots & \cdot \end{pmatrix} \begin{pmatrix} u_{00} \\ \cdot \\ \cdot \\ u_{ij} \\ \cdot \\ \cdot \\ u_{NN} \end{pmatrix}$$

$$+ \begin{pmatrix} d^{z\eta}_{11,00} & \cdots & d^{z\eta}_{11,ij} & \cdots & d^{z\eta}_{11,NN} \\ . & \cdots & . & \cdots & . \\ . & \cdots & . & \cdots & . \\ d^{z\eta}_{kl,00} & \cdots & d^{z\eta}_{kl,ij} & \cdots & d^{z\eta}_{kl,NN} \\ . & \cdots & . & \cdots & . \\ . & \cdots & . & \cdots & . \\ d^{z\eta}_{(N-1)(N-1),00} & \cdots & d^{z\eta}_{(N-2)(N-1),ij} & \cdots & . \end{pmatrix} \begin{pmatrix} u_{00} \\ . \\ . \\ u_{ij} \\ . \\ . \\ u_{NN} \end{pmatrix} \tag{3.47}$$

where

$$d^{z\xi}_{kl,ij} = \sum_{p=0}^{N}\sum_{q=0}^{N} h_i'(\xi_p)h_j(\eta_q)\widetilde{h}_k(\xi_p)\widetilde{h}_l(\eta_q)r(\xi_p,\eta_q)\frac{\partial r}{\partial \eta}_{pq}\frac{|J_{pq}|}{J_{pq}}w_p w_q \ , \tag{3.48}$$

and

$$d^{z\eta}_{kl,ij} = \sum_{p=0}^{N}\sum_{q=0}^{N} h_i(\xi_p)h_j'(\eta_q)\widetilde{h}_k(\xi_p)\widetilde{h}_l(\eta_q)r(\xi_p,\eta_q)\frac{\partial r}{\partial \xi}_{pq}\frac{|J_{pq}|}{J_{pq}}w_p w_q \ . \tag{3.49}$$

Similarly, the second term of the equation (3.39) can be written as

$$\int_{\Omega_{st}(t)} \left(\frac{\partial z}{\partial \xi}\frac{\partial}{\partial \eta} - \frac{\partial z}{\partial \eta}\frac{\partial}{\partial \xi}\right) v(\xi,\eta)q(\xi,\eta)r\frac{|J|}{J}d\xi d\eta = D_{r\xi}\mathbf{u}_r + D_{r\eta}\mathbf{u}_r \tag{3.50}$$

and the last term as

$$\int_{\Omega_{st}(t)} v(\xi,\eta)q(\xi,\eta)\,|J|\,d\xi d\eta = D_v\mathbf{u_r} \ , \tag{3.51}$$

where, for instance, in $D_{r\eta}\mathbf{u_r}$

$$d^{r\eta}_{kl,ij} = \sum_{p=0}^{N}\sum_{q=0}^{N} h_i(\xi_p)h_j'(\eta_q)\widetilde{h}_k(\xi_p)\widetilde{h}_l(\eta_q)r(\xi_p,\eta_q)\frac{\partial z}{\partial \xi}_{pq}\frac{|J_{pq}|}{J_{pq}}w_p w_q \ , \tag{3.52}$$

and in D_v

$$d^v_{kl,ij} = \sum_{p=0}^{N}\sum_{q=0}^{N} h_i(\xi_p)h_j(\eta_q)\widetilde{h}_k(\xi_p)\widetilde{h}_l(\eta_q)\,|J_{pq}|\,w_p w_q\ . \tag{3.53}$$

Obviously D_v is the mass matrix, which is not diagonal since $\widetilde{h}_k(\pm 1) \neq 0$ and $\widetilde{h}_l(\pm 1) \neq 0$. If we let

$$D_z = D_{z\xi} + D_{z\eta} \quad \textit{and} \quad D_r = D_{r\xi} + D_{r\eta}\ , \tag{3.54}$$

and

$$D = (D_z,\ \ D_r + D_v)\ ,$$

then the discrete weak formulation of the continuity equation (3.44) can be written as

$$D\mathbf{u} = 0\ . \tag{3.55}$$

3.6 Spacial Discretization of the Momentum Equation

The pressure term in the weak form of the momentum v-equation (2.21) may be written as

$$\int_{\Omega_{el}(t)} \frac{\partial \varphi_r(z,r)}{\partial r} p(z,r) r dz dr$$

$$= \int_{\Omega_{st}(t)} \left(\frac{\partial z}{\partial \xi}\frac{\partial}{\partial \eta} - \frac{\partial z}{\partial \eta}\frac{\partial}{\partial \xi}\right) \varphi_r(\xi,\eta) p(\xi,\eta) r(\xi,\eta) \frac{|J|}{J} d\xi d\eta\ , \tag{3.56}$$

Similar to the continuity equation, the right-hand side of the above equation may be expressed in the form of matrix as

$$D_r^T \mathbf{p} = (D_{r\xi}^T + D_{r\eta}^T)\mathbf{p}\ , \tag{3.57}$$

where

$$\mathbf{p} = \begin{pmatrix} p_{11} \\ . \\ . \\ p_{kl} \\ . \\ . \\ p_{(N-1)(N-1)} \end{pmatrix} , \tag{3.58}$$

$$d^{r\xi}_{ij,kl} = -\sum_{p=0}^{N}\sum_{q=0}^{N} h_i'(\xi_p)h_j(\eta_q)\widetilde{h}_k(\xi_p)\widetilde{h}_l(\eta_q)r(\xi_p,\eta_q)\frac{\partial z}{\partial \eta}_{pq}\frac{|J_{pq}|}{J_{pq}}w_p w_q , \tag{3.59}$$

and

$$d^{r\eta}_{ij,kl} = \sum_{p=0}^{N}\sum_{q=0}^{N} h_i(\xi_p)h_j'(\eta_q)\widetilde{h}_k(\xi_p)\widetilde{h}_l(\eta_q)r(\xi_p,\eta_q)\frac{\partial z}{\partial \xi}_{pq}\frac{|J_{pq}|}{J_{pq}}w_p w_q . \tag{3.60}$$

In the same way the pressure term in weak form of the momentum u-equation (2.21) can be given as

$$\int_{\Omega_{el}(t)} \frac{\partial \varphi_z(z,r)}{\partial z} p(z,r) r dz dr = (D^T_{z\xi} + D^T_{z\eta})\mathbf{p} = D^T_z \mathbf{p} , \tag{3.61}$$

where

$$d^{z\xi}_{ij,kl} = \sum_{p=0}^{N}\sum_{q=0}^{N} h_i'(\xi_p)h_j(\eta_q)\widetilde{h}_k(\xi_p)\widetilde{h}_l(\eta_q)r(\xi_p,\eta_q)\frac{\partial r}{\partial \eta}_{pq}\frac{|J_{pq}|}{J_{pq}}w_p w_q , \tag{3.62}$$

and

$$d^{z\eta}_{ij,kl} = -\sum_{p=0}^{N}\sum_{q=0}^{N} h_i(\xi_p)h_j'(\eta_q)\widetilde{h}_k(\xi_p)\widetilde{h}_l(\eta_q)r(\xi_p,\eta_q)\frac{\partial r}{\partial \xi}_{pq}\frac{|J_{pq}|}{J_{pq}}w_p w_q . \tag{3.63}$$

The test functions $h_k(\xi)$, $h_l(\eta)$ $(k,l = 0,\cdots,N)$ are chosen for both φ_z *and* φ_r, which are different from that in the continuity equation. Note that test functions corresponding to boundary nodes at which Dirichlet conditions are

imposed are omitted.

For the diffusion term in equation (2.21), we have

$$\int_{\Omega_{el}(t)} \left(\frac{\partial \varphi_z}{\partial z}\frac{\partial u}{\partial z} + \frac{\partial \varphi_z}{\partial r}\frac{\partial u}{\partial r} \right) r dz dr$$

$$= \int_{\Omega_{st}(t)} \left[G_1 \frac{\partial u}{\partial \xi}\frac{\partial \varphi_z}{\partial \xi} + G_2 \frac{\partial u}{\partial \eta}\frac{\partial \varphi_z}{\partial \eta} + G_3 \left(\frac{\partial u}{\partial \xi}\frac{\partial \varphi_z}{\partial \eta} + \frac{\partial u}{\partial \eta}\frac{\partial \varphi_z}{\partial \xi} \right) \right] r \left| J \right| d\xi d\eta$$

$$= \int_{\Omega_{st}(t)} G_1 \left(\sum_{i=0}^{N}\sum_{j=0}^{N} u_{i,j} h_i'(\xi) h_j(\eta) \right) h'(\xi) h(\eta) r \left| J \right| d\xi d\eta$$

$$+ \int_{\Omega_{st}(t)} G_2 \left(\sum_{i=0}^{N}\sum_{j=0}^{N} u_{i,j} h_i(\xi) h_j'(\eta) \right) h(\xi) h'(\eta) r \left| J \right| d\xi d\eta$$

$$+ \int_{\Omega_{st}(t)} G_3 \left(\sum_{i=0}^{N}\sum_{j=0}^{N} u_{i,j} h_i'(\xi) h_j(\eta) \right) h(\xi) h'(\eta) r \left| J \right| d\xi d\eta$$

$$+ \int_{\Omega_{st}(t)} G_3 \left(\sum_{i=0}^{N}\sum_{j=0}^{N} u_{i,j} h_i(\xi) h_j'(\eta) \right) h'(\xi) h(\eta) r \left| J \right| d\xi d\eta \ , \tag{3.64}$$

where

$$G_1 = \left(\frac{\partial z}{\partial \xi} \right)^2 + \left(\frac{\partial r}{\partial \xi} \right)^2 ,$$

$$G_2 = \left(\frac{\partial z}{\partial \eta} \right)^2 + \left(\frac{\partial r}{\partial \eta} \right)^2 ,$$

$$G_3 = \frac{\partial z}{\partial \xi}\frac{\partial z}{\partial \eta} + \frac{\partial r}{\partial \xi}\frac{\partial r}{\partial \eta} .$$

After performing the integration, the last term of the momentum u-equation (2.20) can be written in the following matrix form

$$\left(E_\xi + E_\eta + E_{\xi\eta} + E_{\eta\xi} \right) \mathbf{u_z} \ . \tag{3.65}$$

Similar to D_ξ etc., except for the difference in size, E_ξ, E_η, $E_{\xi\eta}$ *and* $E_{\xi\eta}$ are $(N+1)^2 \times (N+1)^2$ matrices and their elements can be evaluated as

$$e^{\xi}_{kl,ij} = \sum_{p=0}^{N}\sum_{q=0}^{N} u_{ij} h_i'(\xi_p) h_j(\eta_q) h_k'(\xi_p) h_l(\eta_q) w_p w_q \frac{|J_{pq}|}{Re} G_1^{pq} ,$$

$$e^{\eta}_{kl,ij} = \sum_{p=0}^{N}\sum_{q=0}^{N} u_{ij} h_i(\xi_p) h_j'(\eta_q) h_k(\xi_p) h_l'(\eta_q) w_p w_q r \frac{|J_{pq}|}{Re} G_2^{pq} ,$$

$$e^{\xi\eta}_{kl,ij} = \sum_{p=0}^{N}\sum_{q=0}^{N} u_{ij} h_i'(\xi_p) h_j(\eta_q) h_k(\xi_p) h_l'(\eta_q) w_p w_q r \frac{|J_{pq}|}{Re} G_3^{pq} ,$$

$$e^{\eta\xi}_{kl,ij} = \sum_{p=0}^{N}\sum_{q=0}^{N} u_{ij} h_i(\xi_p) h_j'(\eta_q) h_k'(\xi_p) h_l(\eta_q) w_p w_q r \frac{|J_{pq}|}{Re} G_3^{pq} . \quad (3.66)$$

The above equations can be further simplified, for instance, $e^{\eta\xi}_{kl,ij}$ may be written as

$$e^{\eta\xi}_{kl,ij} = \sum_{q=0}^{N} u_{ij} h_j'(\eta_q) h_k'(\xi_i) h_l(\eta_q) w_i w_q r \frac{|J_{pq}|}{Re} G_3^{iq} .$$

In the same way as described above to discretize the momentum u-equation, the last term of the momentum v-equation may also be written as

$$(E_\xi + E_\eta + E_{\xi\eta} + E_{\eta\xi} + E_v)\, \mathbf{u}_r , \quad (3.67)$$

where in E_v

$$e^{v}_{kl,ij} = \sum_{p=0}^{N}\sum_{q=0}^{N} h_i(\xi_p) h_j(\eta_q) h_k(\xi_p) h_l(\eta_q) \frac{|J_{pq}|}{r(\xi_p\,,\eta_q)} \frac{1}{Re} w_p w_q .$$

$$= h_k(\xi_i) h_l(\eta_j) \frac{|J_{ij}|}{r(\xi_i\,,\eta_j)} \frac{1}{Re} w_i w_j . \quad (3.68)$$

Let

$$E_\xi + E_\eta + E_{\xi\eta} + E_{\eta\xi} = E_z = E_r ,$$

and

$$D_p = (D_z,\ D_r) \qquad E = \begin{pmatrix} E_z & 0 \\ 0 & E_r + E_v \end{pmatrix} , \tag{3.69}$$

then, providing that we do not consider surface tension effects at this stage (the tension term are discussed in Chapter 5), the discrete momentum equation, including both u and v components, can be expressed in the following compact matrix form

$$\int_{\Omega_{st}(t)} \frac{\delta \mathbf{u}}{\delta t}\, \varphi\, r\, |J|\, d\xi d\eta = D_p^T \mathbf{p} - E\mathbf{u} , \tag{3.70}$$

where

$$\mathbf{u} = (\mathbf{u_z}, \mathbf{v_r}) ,$$

$\delta/\delta t$ is the material derivative, E is the diffusion matrix and D_p is the discrete divergence operator.

Chapter 4

Flow past a Solid Sphere

4.1 Introduction

As a precursor to the numerical solution which traces single liquid droplet deformation in a gas flow, the Navier-Stokes equations are solved for the flow over a solid sphere in a circular channel and in an uniform ambience to show the validation of the code developed for the simulation of the moving boundary problem

One of the most important features of flow past a sphere is that the flow around the sphere changes significantly as the relative velocity between the sphere and ambient fluid increases. When this velocity is small the flow follows the contour of the sphere, as shown in Fig. 4.1, and the drag force on the sphere is primarily caused by the viscous stresses on the surface of the body. However, as the relative velocity increases the flow moving past the sphere separates from it at the rear causing a region of recirculating flow in the wake. Further increases in the relative velocity causes the point where the flow separates to move forward on the sphere and the size of recirculation zone to lengthen (Taneda, 1956). In these separated flows, the pressure at

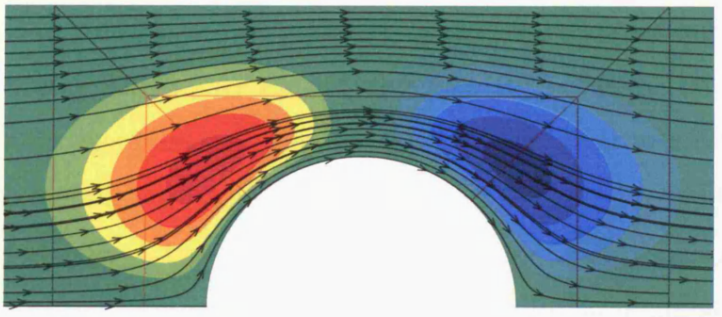

Figure 4.1: Streamlines and vertical velocity contours of the gas flow past a solid sphere in a circular channel with unit Reynolds number.

the front of the sphere, where the flow stagnates, is large while the pressure at the back is approximately equal to the ambient pressure. This asymmetric pressure distribution causes circulating wake and a net pressure force on the sphere forming a new component of the drag. As the separation point of the flow moves forward and the relative velocity increases this part of the drag makes an increasing portion of the total drag until eventually it makes the dominant contribution to the total drag force (Fox and McDonald, 1992).

As shown in Achenbach (1974) and Maxworthy (1969), the drag coefficient, C_d, for uniform flow over a sphere as a function of the Reynolds number, Re, was experimentally determined. For laminar flow, C_d decreases as Re increases and, in particular, varies linearly when the Reynolds number is very small (Schlichting, 1979). As the relative velocity between the sphere and ambient flow further increases, i.e. Re increases, natural instabilities occur causing the recirculating region to oscillate and the circular fluid structures are shed periodically in the wake behind the sphere, and a transition to turbulence may happen when an additional increase in the relative velocity is made. This gives the rise to what is known as a von Karman vortex street. At this stage the drag force experienced tends to vary irregularly, which is beyond our interest in this thesis.

The behaviour of the flow of viscous fluid past a stationary isolated sphere at varying Reynolds numbers has been studied by a number of researchers. Taneda (1956) used flow visualization methods to study the wake of a sting mounted solid sphere for $5 < Re < 300$, where Re is the Reynolds number based on the sphere diameter D and the free stream velocity U_∞. He determined that separation from the rear of the sphere occurs at $Re \approx 24$ and results in an axisymmetric vortex ring.

The dye technique was applied by Magarvey and Bishop (1961) to reveal the wakes of free falling drops of an immiscible liquid in water. A qualitative comparison may be made between the results observed and the standard solid sphere wakes because of the presence of surface-active impurities at the liquid-liquid interface, which hold the drops in semi-rigid spherical shapes, as pointed out by Natarajan and Acrivos (1993). The wakes of the liquid spheres, showed by Magarvey and Bishop, exhibited the same vortex ring structure observed by Taneda. In the range $210 < Re < 270$, the flow became non-axisymmetric as the ring vortex shifted off axis and the dye was released from the wake in two parallel threads, which was observed to remain steady, and from $Re = 270$ the double-thread wake was seen to become unstable.

A numerical solution of the flow over a sphere for $25 < Re < 1000$, using a spectral element method, was presented by Tomboulides (1993), which shows steady axisymmetric flow for $Re < 212$ with initial separation at $Re = 20$. In this work a transition to non-axisymmetric wake occured at $Re = 212$ and the vorticity of the resulting steady flow field resembled the double-thread wake observed by Magarey and Bishop for $210 < Re < 270$. Natarajan and Acrivos (1993) applied a finite element method to investigate the stability of flows over a sphere at low Reynolds numbers, and results consistent with the above calculations were obtained.

Johnson and Patel (1999) investigated the flow of an incompressible viscous fluid past a stationary isolated sphere both numerically and experimentally for flow regimes including steady and unsteady laminar flow at Reynolds numbers up to 300. The calculations for Reynolds numbers up to 200, using a finite volume method, show steady axisymmetric flow and the near-wake

pattern which compares well to the previous numerical predictions and the observations in laboratories. A non-steady axisymmetric regime as well as unsteady flows are also found for Reynolds numbers in the range 210 to 270, and further.

In this chapter, a simplified formulation of the droplet deformation problem and its spectral element spatial approximation for the flows over a fixed sphere is given (see Section 4.2). The Navier-Stokes equations are solved using an iterative technique, for which a few temporal discretization schemes are introduced and described in Section 4.3. The nodes in the spectral element mesh need to be numbered conveniently so that the discrete operators can be set up and solved efficiently with the iterative method. This is presented in Section 4.4. The last two sections show the results from the numerical solution of the Stokes and the Navier-Stokes equations for the flows over a fixed solid sphere. The mesh convergence of the numerical approximations for the PDEs, the relation between Reynolds number and the drag on the sphere, and the wake structure behind the sphere are also presented. Furthermore, some of the data from the calculations are compared with previous results in the context of the axisymmetric steady regime.

4.2 Governing Equations

The single phase flow of an isothermal, incompressible fluid is described by the equations for conservation of mass and momentum:

$$\nabla \cdot \mathbf{u} = 0 \tag{4.1}$$

$$\rho \left(\frac{\partial \mathbf{u}}{\partial t} + \mathbf{u} \cdot \nabla \mathbf{u} \right) = -\nabla p + \nabla \cdot \boldsymbol{\tau} \tag{4.2}$$

where $\mathbf{u} = (u, v)$ is the velocity field ρ is the density, p is the pressure, and $\boldsymbol{\tau}$ is the viscous stress tensor. After non-dimensionalization and coordinate transformation (see Section 2.4), equation (4.1) and (4.2) can be written as the component form of equations (2.14) to (2.16) with the phase number k and the interfacial force M_k omitted.

The continuity equation is

$$\frac{\partial u}{\partial z} + \frac{\partial v}{\partial r} + \frac{v}{r} = 0 \ . \tag{4.3}$$

The components of the momentum equation are

$$\frac{\partial u}{\partial t} + u\frac{\partial u}{\partial z} + v\frac{\partial u}{\partial r} = -\frac{\partial p}{\partial z} + \frac{1}{Re}\left(\frac{\partial^2 u}{\partial z^2} + \frac{\partial^2 u}{\partial r^2} + \frac{1}{r}\frac{\partial u}{\partial r}\right) \tag{4.4}$$

and

$$\frac{\partial v}{\partial t} + u\frac{\partial v}{\partial z} + v\frac{\partial v}{\partial r} = \frac{\partial p}{\partial r} + \frac{1}{Re}\left(\frac{\partial^2 v}{\partial z^2} + \frac{\partial^2 v}{\partial r^2} + \frac{1}{r}\frac{\partial v}{\partial r} - \frac{v}{r^2}\right) \tag{4.5}$$

Obviously the discrete form of equation (4.3) as well as the discrete forms of (4.4) and (4.5) are equations (3.55) and (3.70), the temporal approximations of which are discussed in Section 4.3.

The boundary condition for the calculation is basically the same as that discussed in Section (2.5). A Stokes flow field may be taken as initial flow state for $Re \neq 0$.

4.3 Temporal Discretization

In the governing equations (4.3)-(4.5), the time t is an independent variable. Like other numerical schemes with SE methods, it will not be discretized

using a spectral approximation. Instead, the Euler method and a scheme with the combination of the second order backward differentiation and the third order Adams-Bashforth formulation (BD2/AB3) are used.

Finite difference methods are widely applied to approximate the temporal derivative in the Navier-Stokes equations, irrespective of the spatial discretization methods used, for their efficiency and being good enough to fill the requirements of accuracy. Despite that we are only using these schemes as a means of obtaining steady flows in this chapter, the techniques used for transient flows are utilized to determine the solution, which will directly facilitate the moving boundary algorithm discussed in Chapter 5. We simply use the time step Δt as an iteration parameter. The discrete time levels are denoted as t^k, where $k = n + 1$ refers to the next time level that is to be calculated, $k = n$ refers to the current time level at which the solution has just been calculated, $k = n - 1$ is the time level before the time level n.

The Euler discretization is a first order scheme to approximate the material derivatives in the momentum equations. It is used to simulate axial flows over a sphere in a 2:1 circular duct as it is easy-formulated, and efficient for low speed laminar channel flows. This is the first stage of the code development, and then BD2/AB3 is introduced to raise the accuracy for ambient axial flows over a smaller sphere, which is much closer to the case of droplet deformation in an internal engine environment. Both schemes are semi-implicit as the convection terms will be approximated explicitly. So it is expected that comparatively smaller time steps, less than the large time steps usually adopted by implicit algorithms, should be taken to avoid critical CFL conditions and the instability in the calculations caused by the treatment of the nonlinear terms in the momentum equations.

4.3.1 Euler Scheme

The Euler approximation of the material derivative of velocity $\mathbf{u}$ is

$$\frac{D\mathbf{u}}{Dt} = \frac{\partial \mathbf{u}}{\partial t} + \mathbf{u} \cdot \nabla \mathbf{u} \approx \frac{\mathbf{u} - \mathbf{u}^n}{\Delta t} + \mathbf{u}^n \cdot \nabla \mathbf{u}^n \tag{4.6}$$

replacing the convection term in equation (3.6) by the above approximation and carrying out the Gauss-Lobatto integration we obtain the following system of algebraic equations as complete discretization for the momentum equations

$$(E + \sigma M)\mathbf{u} - D_p^T \mathbf{p} = \mathbf{f} \tag{4.7}$$

where $\sigma = 1/\Delta t$, and M is the velocity mass matrix defined by

$$M_{pq} = \omega_p \omega_q r(\xi_p, \eta_q) \, |J_{pq}| \, \delta_{pq} \ , \qquad p, q = 0, \cdots, N \ . \tag{4.8}$$

Here δ_{pq} is the Kroneker delta and

$$\omega_p = \frac{2}{N(N+1)[L_N(\xi_p)]^2} \ ,$$

as explained in Section 3.3.4 . Also $\mathbf{f} = (\mathbf{f_u}, \mathbf{f_v})$ is a known vector in which, for example, $\mathbf{f_u}$ can be expressed as

$$\mathbf{f}_u = \sigma M \mathbf{u}_z^n - M \begin{pmatrix} c_{00}^n \\ \cdot \\ \cdot \\ c_{kl}^n \\ \cdot \\ \cdot \\ c_{NN}^n \end{pmatrix} \tag{4.9}$$

or, alternatively, as

$$\mathbf{f}_u = (f_u^{00}, \cdots, f_u^{kl}, \cdots, f_u^{NN})^T$$

where

$$f_u^{kl} = \sigma \sum_{p=0}^{N}\sum_{q=0}^{N}\sum_{i=0}^{N}\sum_{j=0}^{N} u_{ij}^n h_k(\xi_p) h_l(\eta_q) h_i(\xi_p) h_j(\eta_q) \omega_p \omega_q r(\xi_p, \eta_q) \, |J_{pq}|$$

$$+ \sum_{p=0}^{N}\sum_{q=0}^{N}\sum_{i=0}^{N}\sum_{j=0}^{N} c_{ij}^n h_k(\xi_p) h_l(\eta_q) h_i(\xi_p) h_j(\eta_q) \omega_p \omega_q r(\xi_p, \eta_q) \, |J_{pq}| \ . \tag{4.10}$$

The coefficients in (4.10) are given by

$$c_{ij}^n = u_{ij}^n \left(\frac{\partial u^n}{\partial z}\right)_{i,j} + v_{ij}^n \left(\frac{\partial u^n}{\partial r}\right)_{i,j} \tag{4.11}$$

where

$$\left(\frac{\partial u^n}{\partial z}\right)_{i,j} = \left(\frac{\partial u^n}{\partial \xi}\frac{\partial r}{\partial \eta} - \frac{\partial u^n}{\partial \eta}\frac{\partial r}{\partial \xi}\right)_{i,j} \frac{1}{J_{ij}}$$

$$= \left(\frac{1}{J}\frac{\partial r}{\partial \eta}\right)_{i,j} \sum_{r=0}^{N}\sum_{s=0}^{N} u_{rs}^n h_r'(\xi_p) h_s(\eta_q)$$

$$- \left(\frac{1}{J}\frac{\partial r}{\partial \xi}\right)_{i,j} \sum_{r=0}^{N}\sum_{s=0}^{N} u_{rs}^n h_r(\xi_p) h_s'(\eta_q)$$

and

$$\left(\frac{\partial u^n}{\partial r}\right)_{i,j} = \left(\frac{\partial u^n}{\partial \eta}\frac{\partial z}{\partial \xi} - \frac{\partial u^n}{\partial \xi}\frac{\partial z}{\partial \eta}\right)_{i,j} \frac{1}{J_{ij}}$$

$$= \left(\frac{1}{J}\frac{\partial z}{\partial \xi}\right)_{i,j} \sum_{r=0}^{N}\sum_{s=0}^{N} u_{rs}^n h_r(\xi_p) h_s'(\eta_q)$$

$$- \left(\frac{1}{J}\frac{\partial z}{\partial \eta}\right)_{i,j} \sum_{r=0}^{N}\sum_{s=0}^{N} u_{rs}^n h_r'(\xi_p) h_s(\eta_q) \ .$$

4.3.2 BD2/AB3

In the BD2/AB3 scheme, the linear terms in the temporal discretization are discretized implicitly using a second order differentiation scheme and

the nonlinear terms are discretized explicitly using a third order Adams-Bashforth method. Thus, the momentum equations may be written in the following matrix form

$$\frac{1}{2\Delta t}M\left(3\mathbf{u}^{n+1} - 4\mathbf{u}^{n} + \mathbf{u}^{n-1}\right) - \frac{8}{3}C^{n} + \frac{7}{3}C^{n-1} - \frac{2}{3}C^{n-2} = D_p^T\mathbf{p} - E\mathbf{u}^{\mathbf{n+1}} , \tag{4.12}$$

where

$$C^q = M(c_{00}^q, \cdots, c_{kl}^q, \cdots, c_{NN}^q)^T ,$$

here $q = n, n-1, n-2$.

To coincide with the expression of equation (4.7), (4.12) may also be expressed as

$$(E + \sigma M)\mathbf{u}^{n+1} - D_p^T\mathbf{p} = \mathbf{f} , \tag{4.13}$$

where

$$\sigma = \frac{3}{2\Delta t} .$$

The right-hand side of the axial component of the momentum equation is

$$\mathbf{f}_u = \frac{1}{3}M(4\sigma\mathbf{u}_z^n - \sigma\mathbf{u}_z^n) + \frac{8}{3}M\begin{pmatrix} c_{00}^n \\ \cdot \\ \cdot \\ c_{kl}^n \\ \cdot \\ \cdot \\ c_{NN}^n \end{pmatrix}$$

$$-\frac{7}{3}M\begin{pmatrix} c_{00}^{n-1} \\ \cdot \\ \cdot \\ c_{kl}^{n-1} \\ \cdot \\ \cdot \\ c_{NN}^{n-1} \end{pmatrix} + \frac{2}{3}M\begin{pmatrix} c_{00}^{n-2} \\ \cdot \\ \cdot \\ c_{kl}^{n-2} \\ \cdot \\ \cdot \\ c_{NN}^{n-2} \end{pmatrix} \tag{4.14}$$

Replace the derivatives $\left(\frac{\partial u^n}{\partial z}\right)_{i,j}$ and $\left(\frac{\partial u^n}{\partial r}\right)_{i,j}$ by $\left(\frac{\partial v^n}{\partial z}\right)_{i,j}$ and $\left(\frac{\partial v^n}{\partial r}\right)_{i,j}$ etc. in equation (4.11), $\mathbf{f_v}$ can be obtained in the same way as the above.

4.4 Solving the Discretized Equations

4.4.1 Pressure Treatment

Both finite element and finite volume methods suffer from the presence of parasitic modes as do spectral/*hp* element methods. This means that when solving the Navier-Stokes equations we need to filter out, in some way, the so-called 'spurious pressure modes', which are characterized as non-constant pressures whose derivatives will vanish at all the interior collocation mesh points so that they cannot be determined from the discrete equations.

Several methods have been developed to deal with the problem caused by the spurious pressure modes. For instance, the MAC method for finite differences (Roache, 1982) and the staggered grid method (Ferziger, 1999) for finite volume. However, those methods are usually difficult in manipulation with spectral element/*hp* schemes although some author has done a meaningful job, in which a particular implementation using a staggered grid consisting of Gauss-Legendre and Gauss-Lobatto-Legendre collocation points for the

pressure and the velocity, respectively (Rϕnquist, 1996). But it is difficult to apply Rϕnquist's method to three-dimensional situations.

On the other hand, the choice of basis for the test or trial functions does not deal with the checkerboard problem, although some of the theoretical results may be slightly different for Chebyshev or Legendre discretization (Canuto et.al., 1987). Therefore, the standard approach in most of SE/*hp* approaches is to reduce the order of the polynomial space for the pressure representation (Karniadakis and Sherwin, 1999). In this way, the pressure is only represented on the interior mesh nodes of the spectral elements.

Let us denote by $P_N(\Omega_{el})$ the space of all polynomials of degree less than or equal to N on the domain of a spectral element Ω_{el}. The velocity and pressure approximation spaces may be defined by

$$V_N = V \bigcap P_N(\Omega) \tag{4.15}$$

$$Q_N = Q \bigcap P_{N-2}(\Omega) \tag{4.16}$$

We further denote the global basis functions for V_N and Q_N by

$$\{\varphi_k(\mathbf{x}) : k = 0, \cdots, N\}$$

$$\{q_k(\mathbf{x}) : k = 1, \cdots, N-1\}$$

respectively, here $\mathbf{x}$ is the vector (z, r), and then the linear system of (4.13) and (3.55) is obtained. This is the reason that the test function $q(\mathbf{x})$ is used for the weak formulation of the continuity equation.

4.4.2 Solving the Linear System on a Spectral Element

4.4.2.1 The Uzawa Operator

Following the discussions in Sections 4.3 and 3.4, 3.5 of Chapter 3, the discrete linear system of the weak form of equations (4.3)-(4.5) may be written as

$$(\sigma M + E)\mathbf{u}^{n+1} - D_p^T\mathbf{p} = \mathbf{f} \tag{4.17}$$

$$D\mathbf{u}^{n+1} = 0 \tag{4.18}$$

and its component form can be shown as

$$\sigma M \begin{pmatrix} \mathbf{u}_z{}^{n+1} \\ \mathbf{u}_r{}^{n+1} \end{pmatrix} + \begin{pmatrix} E_z & 0 \\ 0 & E_r + E_v \end{pmatrix} \begin{pmatrix} \mathbf{u}_z{}^{n+1} \\ \mathbf{u}_r{}^{n+1} \end{pmatrix} - \begin{pmatrix} D_z^T \\ D_r^T \end{pmatrix} \mathbf{p} = \begin{pmatrix} \mathbf{f}_u \\ \mathbf{f}_v \end{pmatrix} \tag{4.19}$$

$$\begin{pmatrix} D_z & D_z + D_v \end{pmatrix} \begin{pmatrix} \mathbf{u}_z{}^{n+1} \\ \mathbf{u}_r{}^{n+1} \end{pmatrix} = 0 \,. \tag{4.20}$$

Elimination of $\mathbf{u}^{n+1}$ from this system yields

$$\mathbf{u}^{n+1} = (\sigma M + E)^{-1}(\mathbf{f} - D_p^T\mathbf{p}) \,, \tag{4.21}$$

which serves to provide the following equation for $\mathbf{p}$

$$D(\sigma M + E)^{-1}D_p^T\mathbf{p} = D(\sigma M + E)^{-1}\mathbf{f} \,. \tag{4.22}$$

The pressure matrix $S = D(\sigma M + E)^{-1}D_p^T$, sometimes known as the Uzawa operator, is positive semi-definite. It follows that $\mathbf{u}^{n+1}$ is uniquely determined by equation (4.21) and $\mathbf{p}$ is determined up to a constant by (4.22). The matrix S is also symmetric and this has important consequences for the iterative solution of (4.22). It means, for instance, the preconditional

conjugate gradient (PCG) method may be used to solve the system, and this is the solution procedure adopted in this thesis. In the process of solving the pressure equation (4.22) both the Uzawa operator and the diffusion matrix need to be inverted. The inversion of the diffusion operator E is nested within the Uzawa operation.

The other advantage in choosing an iteration method is that the algorithms are set up in such a way that there is no need to explicitly construct the discrete matrix. This results in a low memory usage and therefore relatively large problems may be solved, and in the process of inversion only matrix-vector multiplications have to be performed.

4.4.2.2 The PCG method

The standard preconditional conjugate gradient (PCG) method for inversion of the problem $U\mathbf{p} = \mathbf{b}$ is given by the following steps. Here U is the Uzawa operator, and $\mathbf{b}$ represents $D(\sigma M + E)^{-1}\mathbf{f}$ in the pressure equation. The right-hand side $\mathbf{b}$ is a known vector and is determined from previous calculations or the initial condition. In the process of solution, other known terms such as those associated with the boundary conditions will also be moved to the right-hand side of the equation.

The PCG Algorithm

- Use an initial guess $\mathbf{p}_0$ for the pressure to calculate the initial residual $\mathbf{r}_0$

$$\mathbf{r}_0 = \mathbf{b} - U\mathbf{p}_0$$

- Initialize the other PCGM variables

$$\mathbf{z}_0 = P_U^{-1}\mathbf{r}_0$$

$$\mathbf{q}_0 = \mathbf{z}_0$$

where P_U is the preconditioner for the Uzawa operator.

- The iteration to search for the correct solution vector $\mathbf{x}$ is

$$\begin{aligned}
\alpha_{n+1} &= \frac{\mathbf{r}_n^T \mathbf{z}_n}{\mathbf{q}_n^T U \mathbf{q}_n} \\
\mathbf{r}_{n+1} &= \mathbf{r}_n - \alpha_n U \mathbf{q}_n \\
\mathbf{z}_{n+1} &= P_U^{-1} \mathbf{r}_{n+1} \\
\beta_{n+1} &= \frac{\mathbf{r}_{n+1}^T \mathbf{z}_{n+1}}{\mathbf{r}_n^T \mathbf{z}_n} \\
\mathbf{x}_{n+1} &= \mathbf{x}_n + \alpha_{n+1} \mathbf{q}_n \\
\mathbf{q}_{n+1} &= \mathbf{z}_{n+1} + \beta_{n+1} \mathbf{q}_n
\end{aligned}$$

and repeat until a converged residual $\epsilon_U = \mathbf{r}_{n+1}^T \mathbf{z}_{n+1}$ is obtained.

To calculate $U\mathbf{q_n}$ in every iteration, a calculation for $(\sigma M + E)^{-1} D_p^T \mathbf{q}_n$ needs to be done at first. Since $D_p^T \mathbf{q}_n$ depends on the results from the previous step the inner problem may be understood as

$$\begin{aligned}
(\sigma M + E)^{-1} D_p^T \mathbf{q}_n &= (\sigma M + E)^{-1} \mathbf{b}' = \mathbf{y} \\
\rightarrow \quad (\sigma M + E)\mathbf{y} &= \mathbf{b}'
\end{aligned} \tag{4.23}$$

where $\mathbf{b}'$ is known from previous calculation and $(\sigma M + E)$, known as the Helmholtz operator, is also symmetric, so another PCGM iteration has to be performed to solve (4.23).

Obviously, the Uzawa inversion can only converge if the the convergence criterion for inversion of equation (4.23), ϵ_E, is smaller than the convergence criterion for the Uzawa operator, ϵ_U. The difference between these two criteria may increase as the time step decreases. As an empirical result, we

suggest a Uzawa convergence criterion of ϵ_U requires a convergence criterion for the inversion of diffusion matrix $\epsilon_E < 3 \times 10^{-2} \epsilon_U \Delta t$.

4.4.3 Solving Flow on a Physical Domain

A physical domain can be divided into a number of spectral elements, In this thesis the spectral element mesh is constructed using Gambit, a widely available meshing software package provided with the commercial software Fluent. In Gambit, the quadrilateral spectral elements are created within the graphical user interface to define the domain and the element edges, the latter can be assigned with certain boundary types to incorporate boundary conditions. An output data file is produced after the interactive mesh creation process, which provides a list of vertices of elements with their physical coordinates, the definition of the elements with four vertices, always ordered anti-clockwise, and at the end of the datafile, a list of boundaries associated with their types, element numbers and edge numbers.

The output file is read by the in-house code, developed to perform the calculations in this thesis, and the Gauss-Lobatto-Legendre (GLL) grid is created in the code for each of the spectral elements to form a fine mesh. The Gauss-Lobatto-Legendre nodes can only be allocated on the parent element (the standard element), but their physical coordinates can be found through the transfinite mapping (for the work of this chapter) described in Section 3.4.3.1. Note that for the arcs on the elements around the sphere, the mapping is not based on the physical coordinates but radians.

The GLL nodes (including the vertices of the elements) need to be numbered both locally on the spectral element level, and globally on the whole geometry of the computational domain. A convenient local numbering is necessary since most numerical operations may be performed on the elemental

level. Nodes on the element boundaries that are shared by other elements, are characterized by more than one local number. The number of elements that share one node is called the multiplicity, M, of this node, and so there are M different equations associated to this particular node. When solutions need to be continuous over element boundaries, those equations are added together, and a global node numbering is needed to provide this coupling between the elements.

In the local numbering, the origin of the element, where $i = 0$ and $j = 0$, is placed at the first vertex of the element under consideration. No matter how complex the geometry is the first vertex is chosen randomly, so that the origins of the local element numbering is not nessecarily the same in every element. In Fig. 4.2, for example, element 1 has its origin in the bottom left-hand corner, whereas the origin of element 2 is in the top left-hand corner. For the local numbering, a quick and convenient mapping from the discrete coordinates on the standard computational domain $0 \leq i, j \leq N$ is given by the following relation

$$m = i + j(N + 1) \ . \tag{4.24}$$

The local numbering m contains $(N + 1)^2$ entries, ranging from $0 \leq m \leq (N+1)^2 - 1$. In Fig. 4.2, the local numbering m is presented for two adjacent elements using an approximation order $N = 4$. The figure also represents the fact that the origin of the numbering is random, and that as a result of this, an edge of a certain spectral element can share any other edge of the adjacent element. In this figure edge number 2 of element 1 is shared by edge number 1 of element 2.

The global numbering depends on the output data file from Gambit since the first few nodes of a spectral element in the global numbering are the vertices

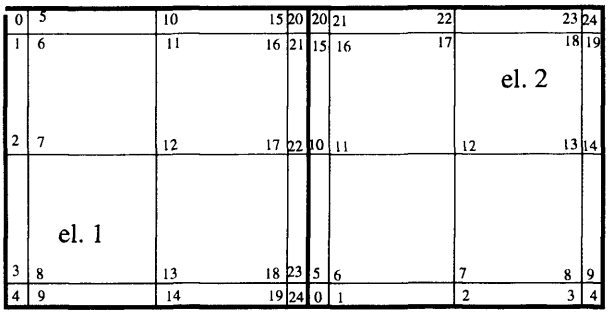

Figure 4.2: Local numbering in adjacent elements, N=4.

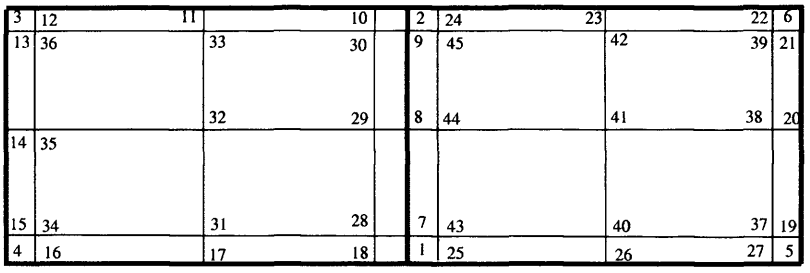

Figure 4.3: Global numbering in adjacent elements, N=4.

of the element, which are numbered as that in the file. Fig. 4.3 shows that these six vertices are numbered at first, followed by the nodes on the element boundaries and finally the inner nodes are numbered. Node numbers 2, 1, 7, 8 and 9 have a multiplicity $M = 2$ but characterized by only one global number. To find a global node number from a local number and vice-versa, a mapping function has been developed to provide the one-to -many mapping from the global to the local numbering and a many-to-one mapping in the reverse direction.

With the local and the global numbering, the algebraic system of equations (4.17) and (4.18) may be solved using the following steps

- Read the output file produced by Gambit, then create a data system

to be used by the solution algorithm.

- Calculate GLL points on the parent computational domain, and then project them onto each spectral element using a transfinite mapping to construct a fine mesh for the computation.

- Set up the selected boundary conditions and initial condition for the flow to be simulated. The pressure values on boundaries are not always available or necessary for industrial applications. However, they are not required because the pressure equation is solved only at the interior mesh nodes of each spectral element.

- Start the time marching. Within every time step

  - Solve the pressure equation via nested PCGM iterations and find the pressure values on the element boundaries using the method of extrapolation. The mean values of the pressure are taken on the edges shared by multiple spectral elements.

  - Substitute the obtained pressure into equation (4.21) to up-date the velocity.

  Take the above solutions as the initial values to start a new time step and continue until they converge.

Since the calculations in this chapter are designed as a provision for the simulation of a moving droplet in air flows, the only preconditioner used for the Uzawa operator is the pressure mass matrix because of the complication of the deformed moving boundary problem. The preconditioner is given by $P_U = M_P$, which involves the spectral element mass matrix in the pressure space acting on the pressure.

4.5 Flow past a Confined Sphere in Circular Channel

The code developed for the purpose of simulating the drop deformation in gas flows was programmed and tested by solving the Stokes flow and the Navier-Stokes flow over a solid sphere as a precursor to solving the moving droplet problem. In this section, the simulations for the Stokes and Navier-Stokes flows past a fixed solid sphere in a circular channel are discussed, whereas the calculations for flows over a solid sphere in an environment of drop deformation will be discussed in the next section.

4.5.1 Stokes Flow

As the first test, Stokes flow may be considered as a special case of the Navier-Stokes flow in which the Reynolds number tends to be zero and the inertia term $\mathbf{u} \cdot \nabla \mathbf{u}$ is negligible when compared with the viscous term $\frac{1}{Re}\nabla^2 \mathbf{u}$, so that the convected time derivative (material derivative $D\mathbf{u}/Dt$) on equation (4.2) is removed and the equations read

$$\nabla \cdot \mathbf{u} = 0 \,, \tag{4.25}$$

$$-\nabla p + \nabla \cdot \boldsymbol{\tau} = 0 \,. \tag{4.26}$$

Therefore, equations (4.3)-(4.5) are reduced by removing the left hand side of the momentum equations and their spectral approximation become

$$-D_p^T \mathbf{p} + E\mathbf{u} = 0 \,, \tag{4.27}$$

$$D\mathbf{u} = 0 \,. \tag{4.28}$$

The computational domain and spectral element structure for the Stokes problem are shown in Fig. 4.4 and Fig. 4.5 respectively. Since the centre of the sphere is located on the axis of the cylinder, the problem is assumed to be axisymmetric and only half of the domain needs to be considered. The algebraic system reduced from (4.22) is solved with the PCG method, as explained in Section 4.4, in cylindrical polar coordinates (r, θ, z), when r is the radial coordinate and the line $r = 0$ represents the axis of symmetry, the coordinate z is in the axial direction, and θ represents the azimuthal coordinate. Obviously it is assumed that the same solution is obtained on any plane θ equals a constant within $[0, \pi]$. In the PCG iteration the convergence criterion of the Uzawa operator is $\epsilon_U = 10^{-13}$ and for the Helmboltz operator (the diffusion matrix), $\epsilon_E = 10^{-17}$. The mesh, shown in Fig. 4.5, is more refined than the mesh in Fig. 4.4 to capture the detailed structure of the flows. The mesh shown in Fig. 4.4 has fewer spectral elements than the mesh in Fig. 4.5 and is therefore cheaper to use computationally.

Both Stokes and Navier-Stokes problems discussed in this chapter are characterized by the maximum velocity U at the inlet or the outlet, and the radius of the channel R that is twice the radius of the sphere. The ratio of the sphere radius r_s to the length of cylinder L is 1:32 (for the 9 element mesh) or 1:16 (for the 12 element mesh), which is sufficient to include the effect from the sphere and ensure that the flow is fully developed according to our experience and the work by Gerritsma and Phillips (2000) as well as Phillips (2001), although the presence of the sphere is felt everywhere in the cylinder due to the elliptic nature of the governing equations.

The calculations of the flow are subject to the following boundary conditions:

$$u = 0 \quad v = 0 \tag{4.29}$$

Figure 4.4: Nine spectral elements mesh for the problem of flow over a sphere in a cylinder tube. The dark lines correspond to element boundaries and the light lines are lines in each physical element that correspond to the lines $\xi = \xi_i, i = 1, \cdots, N-1$ and $\eta = \eta_j, j = 1, \cdots, N-1$ of the parent element in the computational domain. The polynomial order is $N = 4$ for the mesh.

on solid walls including sphere surface,

$$u = U\left[1 - \left(\frac{r}{R}\right)^2\right] \quad v = 0 \tag{4.30}$$

at inflow and outflow,

$$\frac{\partial u}{\partial r} = 0 \quad v = 0 \tag{4.31}$$

on the axisymmetric axis.

For non-dimensional approximation we usually set $U = 1$ and $R = 1$. And initially, the velocity inside the domain is set to zero. The calculations are carried out on both meshes of $K = 9$ and $K = 12$, in which the mesh convergence is checked by the 'error'

$$E_N(\mathbf{u}) = \left\|\mathbf{u}^{N=12} - \mathbf{u}^N\right\| .$$

The solution with $N = 12$ is taken to be the benchmark solution for comparison purposes. Thus, we have

$$\left\|\mathbf{u}^{N=12} - \mathbf{u}^N\right\|^2 = \sum_{el=1}^{K} \sum_{k=0}^{(N=12)^2-1} \left[(u_{k,el}^{N=12} - u_{k,el}^N)^2 + (v_{k,el}^{N=12} - v_{k,el}^N)^2\right] ,$$

where $\mathbf{u}_N$ are the values interpolated to the mesh with $N = 12$ from the results calculated on the mesh with polynomial order $N \neq 12$. The errors are given in Table 4.1 for $K = 9$, one can see the errors decline rapidly towards the machine precision as the approximation order N increases to modest values.

Fig. 4.6 - 4.11 are contours of the numerical approximations of velocities and pressures for a few approximation orders. The difference between the velocities for different values of N does not visibly vary for a value $N \geq 10$. This feature is reflected in the value of drag on the sphere, given in Table 4.2, which has a converged value of 25.79 for $N \geq 10$.

N	$E(\mathbf{u})$
4	1.7593×10^{0}
5	7.0579×10^{-1}
6	1.0847×10^{-1}
7	4.7783×10^{-2}
8	1.0162×10^{-2}
9	3.5573×10^{-3}
10	9.2985×10^{-4}
11	2.0847×10^{-4}

Table 4.1: Convergence of the errors in $\mathbf{u}$ with the increasing polynomial order N calculated using the spectral element mesh with $k = 9$.

N	Drag
4	22.49016
5	24.63574
6	24.99320
7	25.06793
8	25.71722
9	25.77095
10	25.79461
11	25.79572
12	25.79598

Table 4.2: Calculated drag on the sphere fixed in the Stokes flow with increasing refinement of the mesh $K = 9$.

The non-dimensional drag on the sphere is computed using the following expression

$$F_{el} = -2\pi R \int_{\theta_1}^{\theta_2} \left\{ (-p + \mu \frac{\partial u}{\partial z}) cos\theta \; + \; \mu (\frac{\partial u_r}{\partial z} + \frac{\partial u_z}{\partial r}) sin\theta \right\} sin\theta \, r d\theta \quad (4.32)$$

$$F = \sum_{el=1}^{K} F_{el} \; , \quad (4.33)$$

where θ is the angle between the radius of the sphere through the integral node and the axis of the tube, and θ_1, θ_2 are the angles defined respectively by the two corner nodes on the arc edge of a spectral element which is adjacent to the sphere.

Figs. 4.6-4.8 show the contour plots of the velocities and pressure at $N = 8$ on the mesh with 9 elements whereas Figs. 4.9 and 4.10 give the contours of velocity at higher polynomial orders. The velocity contours in Fig 4.11 are obtained from the calculation with the other mesh structure ($K = 12$) with $N = 10$, which demonstrates the similarity of the velocity results produced on the mesh with $k = 9$ at higher polynomial order $N = 12$.

4.5.2 Navier-Stokes Flows

Solving the Navier-Stokes equations is an extension of the solution of the Stokes problem. Comparing equations (4.1)-(4.2) and (4.25)-(4.26) it can be seen that the convected time derivative $D\mathbf{u}/Dt$ adds further complexities to the numerical scheme used. As expressed in Section 4.4, not only a nested PCG algorithm is required, a time marching scheme over the PCG scheme is also needed to lead a calculation to a stable approximate solution of the Navier-Stokes equations.

The backward-Euler method is applied to the time-stepping scheme for the

calculations here, in which the geometry of the flow field is the same as that in the Stokes flow problem. The time marching is terminated when the norm of velocities smaller than 10^{-7}, the norm is defined

$$\left\|\mathbf{u}^{n+1}-\mathbf{u}^{n}\right\| = \left\{\int_{\Omega}[(u_{k,el}^{n+1}-u_{k,el}^{n})^2+(v_{k,el}^{n+1}-v_{k,el}^{n})^2]d\Omega\right\}^{1/2} \tag{4.34}$$

where Ω is the whole domain of flow.

The mesh used, shown in Fig. 4.5, has a finer grid around the surface of the sphere to handle the abrupt change of the flow there, especially the wake behind the sphere. The wake may occur as the Reynolds number increases. Fig. 4.12 shows the fine grid near the interface.

The boundary conditions expressed in the equations (4.29)-(4.31) are also used for the cases discussed in this subsection. The flow field obtained from solving the Stokes problem will be taken as initial condition. In order to ensure that the continuous problem has a classical solution, the initial velocity field must be divergence free, i.e. it must satisfy the the continuity equation (Heywood and Rannacher, 1986). Obviously, the velocity field of Stokes flow meets the requirement and helps the time iteration reach the stable solution quickly as it is much closer to the velocity field to be solved than the zero initiation.

The mesh convergence of the Navier-Stokes problem is studied with the drag, still determined by equations (4.32)-(4.33), on the surface of the sphere. The calculations are performed at Reynolds number $Re = 1$ and the influence of the p-type mesh refinement is shown in Table 4.3 in which the drag is tabulated as a function of the spectral approximation. The table shows that the drag converges with increasing polynomial order. Fig. 4.13 shows the contours of the radial velocity calculated on $K = 12$ mesh with polynomial

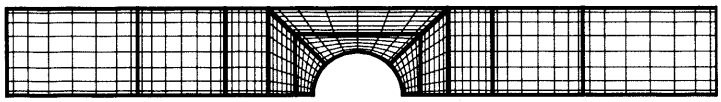

Figure 4.5: Twelve spectral elements mesh for the physical domain for the computation of flows past a solid sphere with $N = 8$.

N	Drag ($Re = 1$)
5	26.46738
6	26.72814
7	27.01195
8	27.02407
9	27.09272
10	27.09632
11	27.09705
12	27.09713

Table 4.3: Convergence of the approximate drag on the sphere for $Re = 1$, with increasing polynomial order.

order $N = 12$.

The choice of time step for the flow simulation is made by comparing the drag computed with $\Delta t = 10^{-2}, 3 \times 10^{-3}, 10^{-3}$ and 3×10^{-4} in Table 4.4, which shows that the differences between drags are less than 1/1000 for the cases when $\Delta t \leq 3 \times 10^{-3}$. Care was taken to select a time step large enough to reach a solution quickly (for a steady problem) and, at the same time, small enough to ensure that any stability criterion is satisfied. Therefore, for most other calculations we use the time step of 3×10^{-3} to reduce the cost of computing. With this value of Δt we did not find any sign of instability in the calculations discussed in this section.

A range of Reynolds number are tested for the numerical simulation to study its influence on the solution . Table 4.5 shows the dependence of the drag on the Reynolds number, as other studies have shown the drag decreases rapidly with increasing Re (e.g. Helenbrook and Edwards 2000).

Δt	Drag $(Re = 1), (N = 10)$
10^{-2}	27.0927
3×10^{-3}	27.0944
10^{-3}	27.0941
3×10^{-4}	27.0943

Table 4.4: Drag on the sphere computed for different values of Δt on the mesh $K = 12$ and $N = 10$ for $Re = 1$.

Re	1	10	20	30	40	50
Drag	27.097	3.627	2.903	2.339	1.927	1.694

Table 4.5: Dependence of drag on Reynolds number.

Previous research found that a wake forms after the sphere as the value of the Reynolds number is increased. It is the onset of this wake region that can cause the numerical schemes to fail, the reasons of which can be that the exit length, the part of tube behind the sphere, is not long enough for the flow to be fully developed, or that the Reynolds number is too large to maintain the axisymmetrical behaviour. The profiles shown in Figs. 4.14 and 4.15 are the velocity contours calculated with $Re = 10$. We can see that there is no wake at this stage. It was found that we are able to have reasonable convergent solutions with $Re \leq 50$ for this case due to the restriction from the length of the channel. The calculations with the values of Re higher than 50 will be discussed in next section. Figs. 4.16-4.17 show the velocity contours at $Re = 50$. There is still no disturbed wake behind the sphere, which occurs in the 2-D channel flow past a cylinder calculated in a similar circumstances

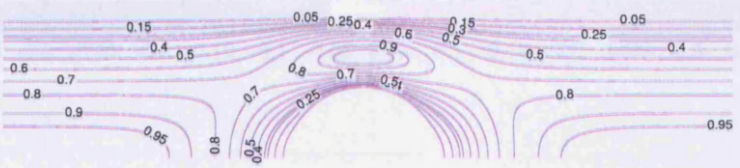

Figure 4.6: Contours of the horizontal component of velocity in the Stokes flow past a solid sphere calculated on the 9 element mesh with the polynomial order $N = 8$.

as that used here. This may be explained by the fact that the resistance to the flow from the sphere is less than the cylinder. Fig. 4.18 is the pressure distribution from the same calculation.

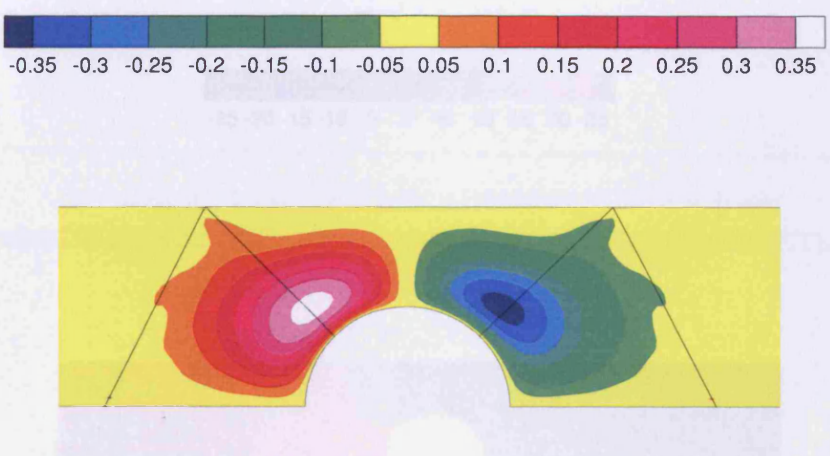

Figure 4.7: Contours of the vertical component of velocity in the Stokes flow past a solid sphere calculated on the 9 element mesh with the polynomial order $N = 8$.

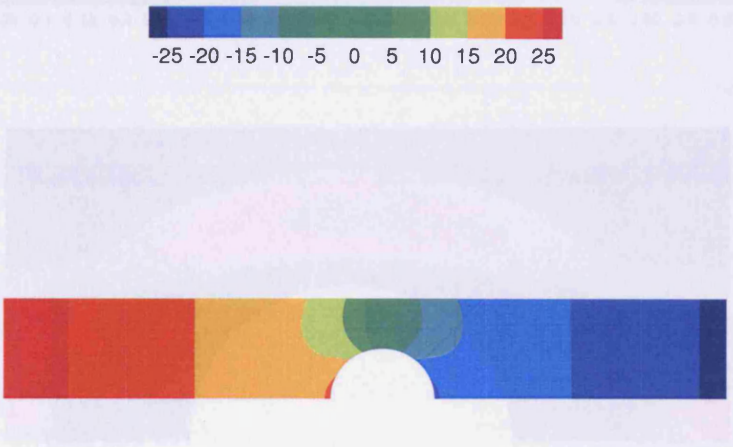

Figure 4.8: Contours of pressure of velocity in the Stokes flow past a solid sphere calculated on the spectral element mesh with $K = 12$ and $N = 10$.

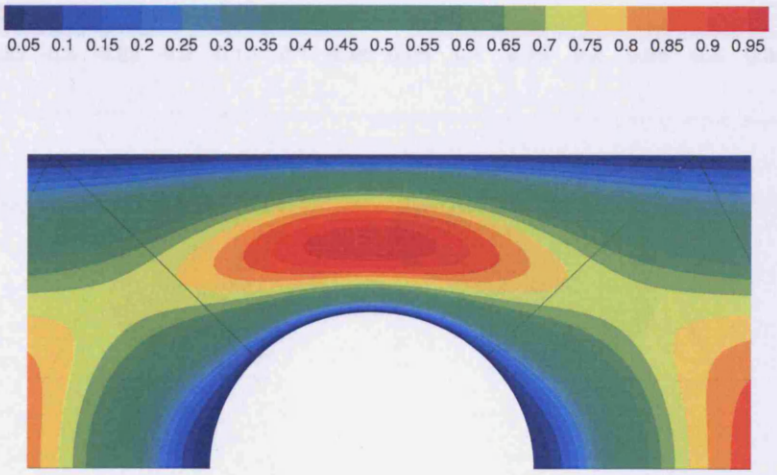

Figure 4.9: Contours of the horizontal component of velocity in the Stokes flow past a solid sphere calculated with $K = 9$ and $N = 12$.

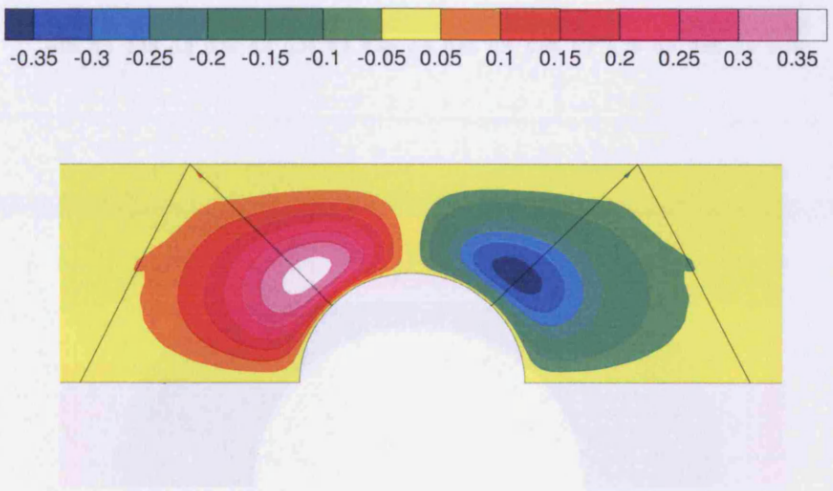

Figure 4.10: Contours of the vertical component of velocity in the Stokes flow past a solid sphere calculated with $K = 9$ and $N = 12$.

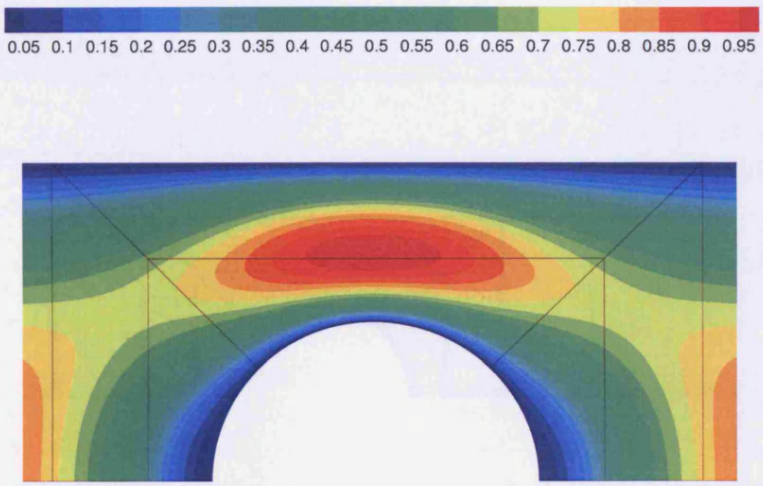

Figure 4.11: Contours of the horizontal component of velocity in the Stokes flow past a solid sphere calculated with $K = 12$ and $N = 10$.

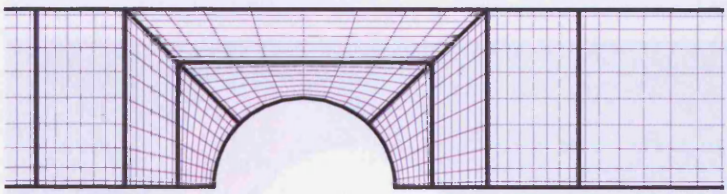

Figure 4.12: Mesh structure around the sphere in a tube with $K = 12$ and $N = 8$ to handle the detail of the abrupt change in Navier-Stokes flows.

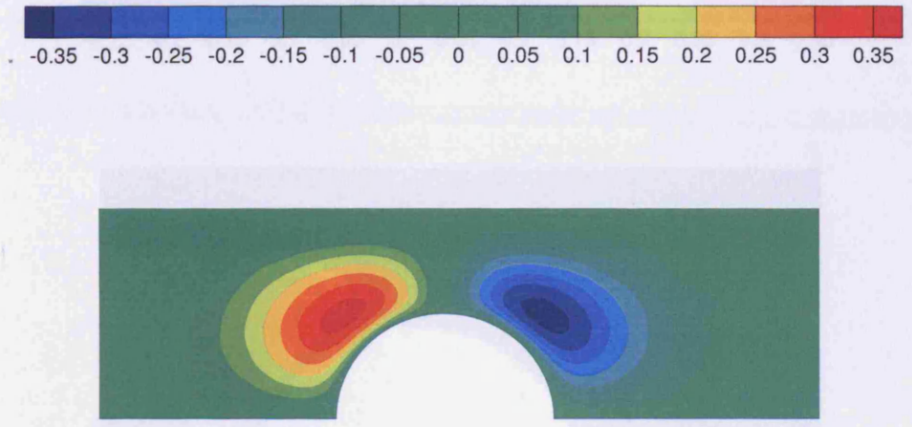

Figure 4.13: Contours of the radial component of velocity in the flow past a solid sphere calculated with $K = 12$ and $N = 12$ for $Re = 1$.

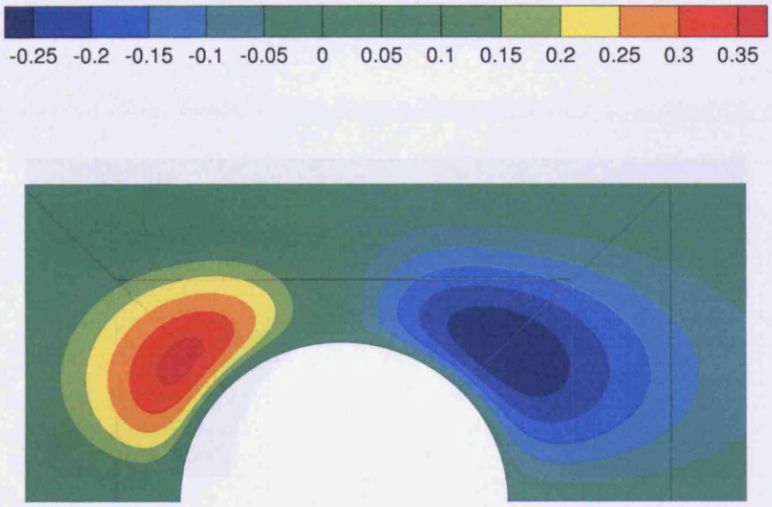

Figure 4.14: Contours of the radial component of velocity in the flow past a solid sphere calculated with $K = 12$ and $N = 8$ for $Re = 10$.

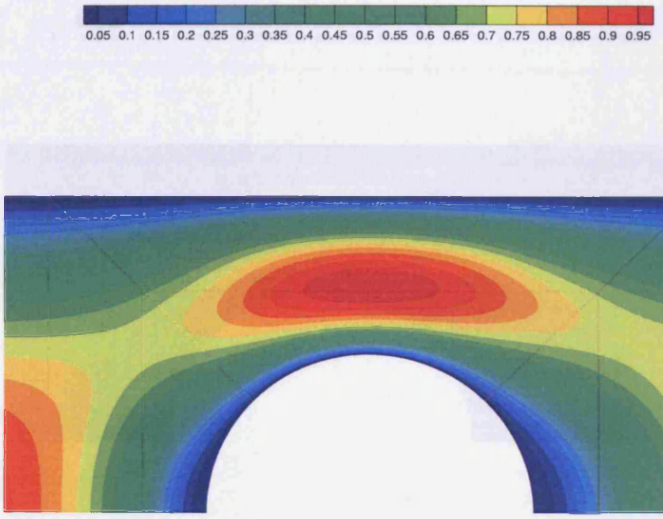

Figure 4.15: Contours of the radial component of velocity in the flow past a solid sphere calculated on the 12 element mesh with $Re = 10$ and the polynomial order $N = 8$.

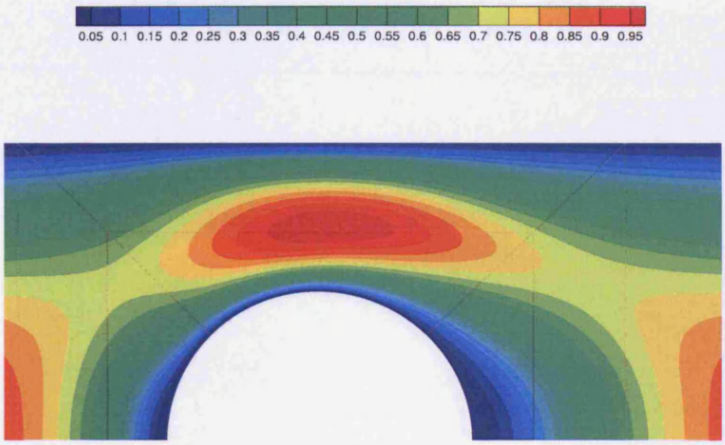

Figure 4.16: Contours of the axial component of velocity in the flow past a solid sphere calculated with $K = 12$ and $N = 8$ for $Re = 50$.

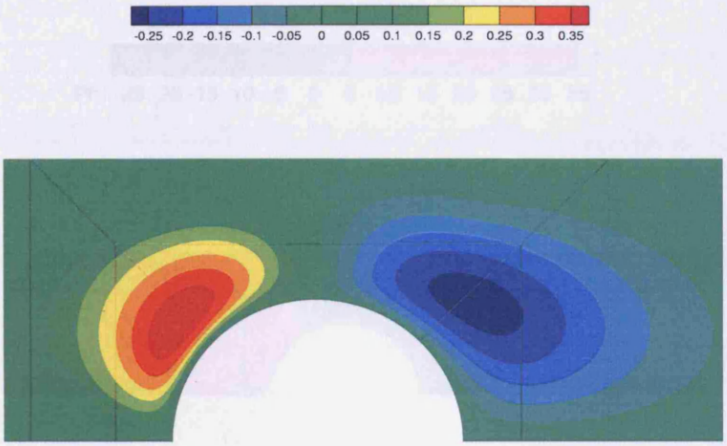

Figure 4.17: Contours of the radial component of velocity in the flow past a solid sphere calculated with $K = 12$ and $N = 8$ for $Re = 50$.

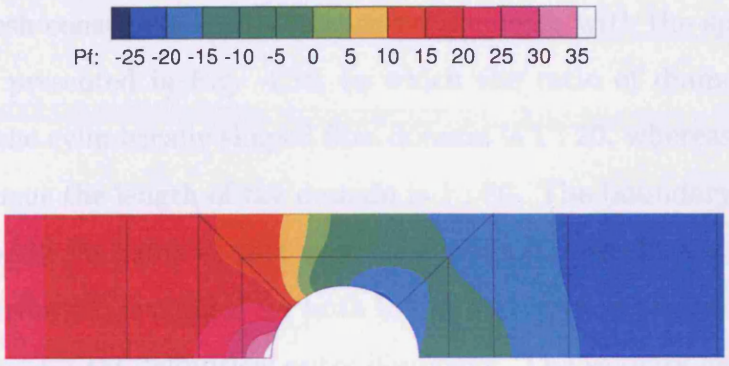

Figure 4.18: Pressure contours of the flow past a solid sphere calculated with $K = 12$ and $N = 8$ for $Re = 50$.

4.6 Flow past a Solid Sphere in a Uniform Ambience

The geometry shown in Fig. 4.5 is too short to simulate the wake behind sphere. As the flow velocity in the tube increases, it was found that the time iteration did not converge properly. Ambient axial flows over a smaller solid sphere is further tested to explore the effect of the obstruction due to the sphere for flows with higher Reynolds numbers. The calculations are carried out on a mesh constructed with 26 spectral elements with the sphere in the middle and presented in Fig. 4.19, in which the ratio of diameters of the sphere and the cylindrically shaped flow domain is 1 : 20, whereas the sphere diameter versus the length of the domain is 1 : 80. The boundary conditions here are mostly the same as that used in Section 4.5 except that a uniform velocity distribution is applied for both inflow and outflow, and that the slip-wall condition for the cylindrical outer boundary. The velocity field obtained from the resolution of Stokes flow on the same grid is also taken as the initial approximations for the simulation. Obviously, this test is more meaningful than the previous as it imitates physically and geometrically the flow with a deformable droplet in industrial environments.

The calculations are conducted with Re between 100 to 200. As mentioned in Section 4.1, within this range of Reynolds number, the flow separates and is steady, axisymmetric and topologically similar. The numerical solutions in this regime were obtained by setting Δt from 3×10^{-3} to 10^{-4} in the interest of numerical efficiency. The results compare well with Johnson and Patal (1999), which matched with the experimental results of Magarvey and Bishop (1961) as well as the numerical results of Natarajan and Acrivos (1993) and Tomboulides (1993). The small differences between the current

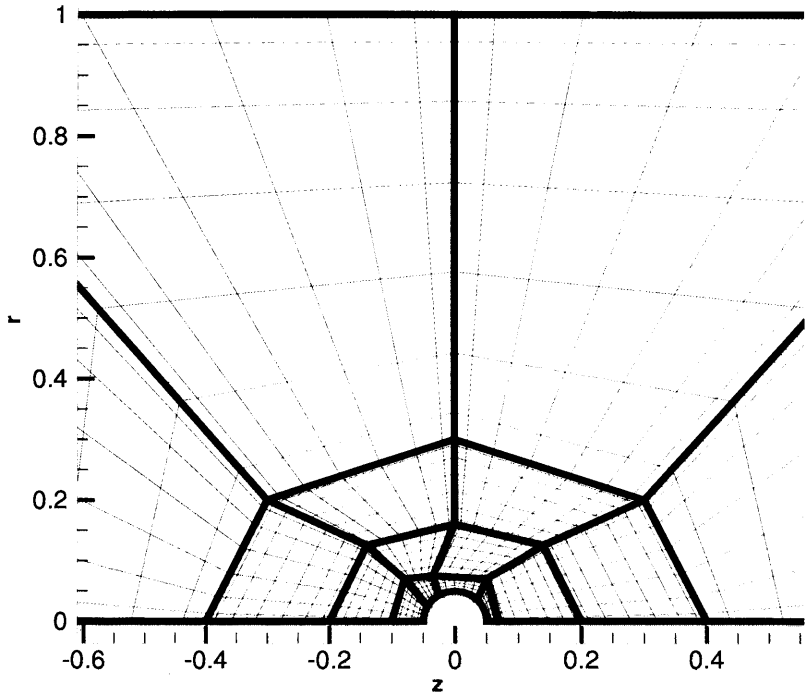

Figure 4.19: Geometry and mesh structure of the ambient flow over a solid sphere.

Re	100	120	150	180
z_c	0.0675	0.0700	0.0705	0.0725
r_c	0.0270	0.0285	0.0300	0.0315
θ_s	132^0	128^0	125^0	120^0
C_D	1.157	0.978	0.917	0.808

Table 4.6: Wake structure and drag coefficient versus the Reynolds number.

simulations and the work of Johnson and Patal are partially due to the lack of complete coincidence between the geometries of the flow domains.

Figs 4.20 to 4.23 plot the flow fields at Reynolds numbers 100, 120, 150, 180 in the form of streamlines, whereas Fig. 4.24 and Fig. 4.25 show the velocity contours together with the streamlines, the flow is from left to right. From the figures we can see that the regimes separate from the rear part of the sphere surface and rejoin on the symmetry axis of the flow, forming a closed bubble with a toroidal vortex centered at (z_c, r_c) where the velocity is zero. All the regimes are almost the same except for the separation location, the size and position of the separation bubble.

Table 4.6 gives the results obtained from the current calculations which shows good agreement with that presented in Johnson and Patal's paper (1999) for separation angle θ_s and vortex centre position (z_c, r_c), the latter includes both numerical and experimental data that are not tabulated here.

Johnson and Patal's results are further compared with the present study in drag coefficient, given as $C_D = F_z/(\frac{1}{2}\rho U_\infty^2 \pi d^2/4)$, where U_∞ is the ambient velocity, d denotes the diameter of the sphere and F_z is the force acting on the sphere in z direction. Johnson and Patal's work was compared well with the

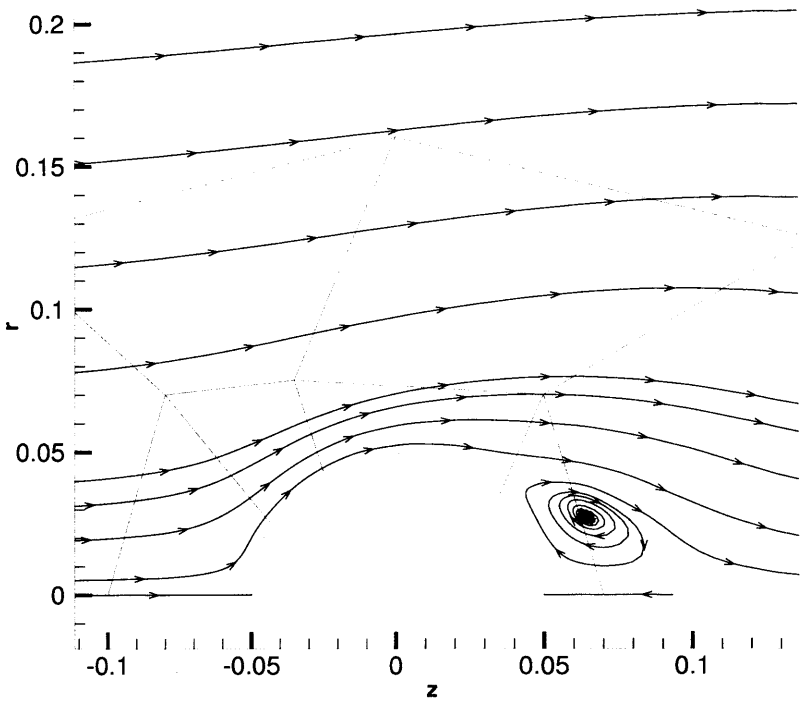

Figure 4.20: Particle tracks (streamlines) and wake structure of the ambient flow over a solid sphere at $Re = 100$.

experimental drag coefficient data provided by Roos and Willmarth (1971). Table 4.6 also shows the values of C_D from the current calculations, which display good agreement with Johnson and Patal's work as well.

Until now, the problem of flow past a solid sphere has been successfully solved using the numerical model expressed in the previous sections for both the conventional test case and the case imitating the problem of gas flow over a liquid drop. The work done in this chapter has formed the basis for the numerical simulation of droplet deformation.

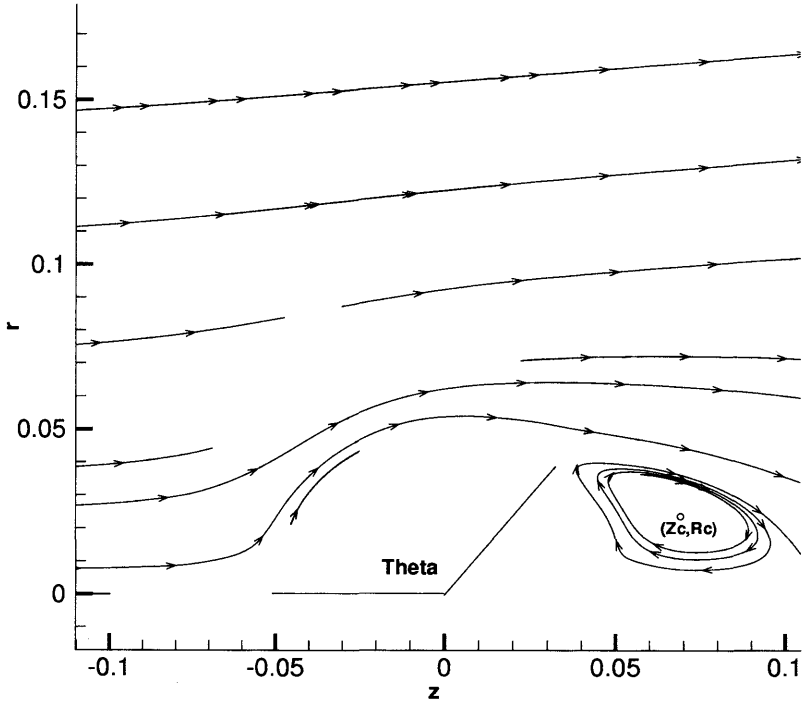

Figure 4.21: Particle tracks (streamlines) and wake structure of the ambient flow over a solid sphere at $Re = 120$.

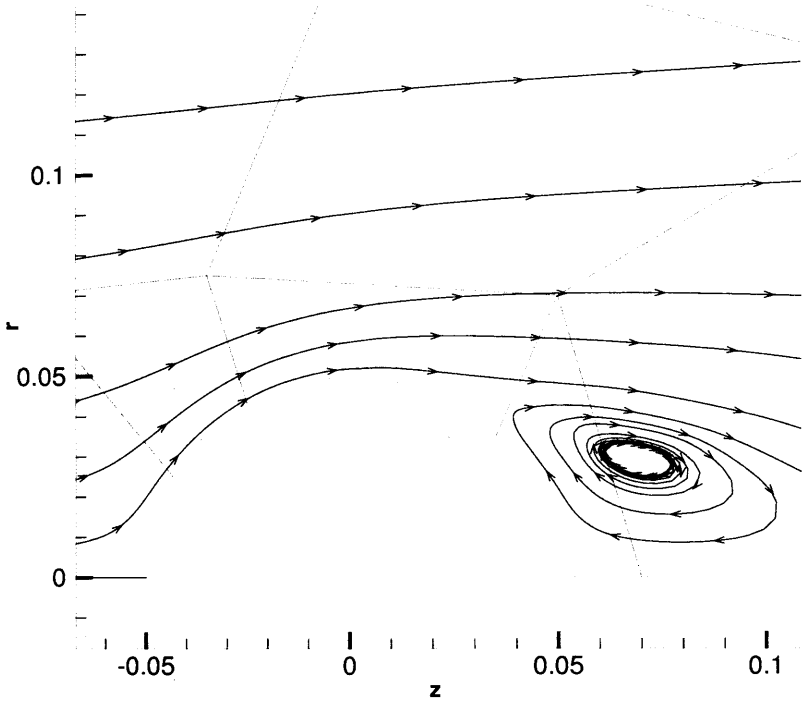

Figure 4.22: Particle tracks (streamlines) and wake structure of the ambient flow over a solid sphere at $Re = 150$.

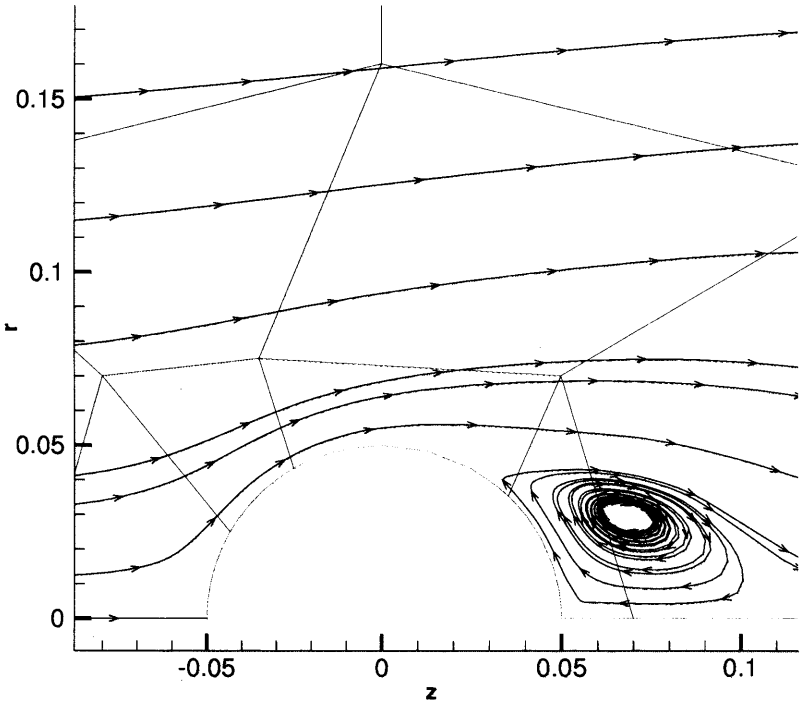

Figure 4.23: Particle tracks (streamlines) and wake structure of the ambient flow over a solid sphere at $Re = 180$.

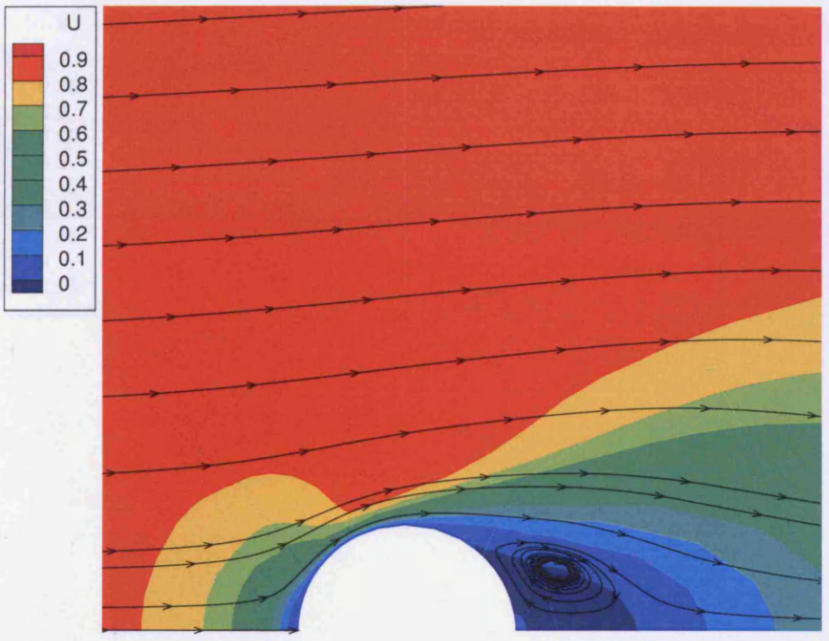

Figure 4.24: Particle tracks (streamlines) with axial velocity contours of the ambient flow over a solid sphere at $Re = 180$.

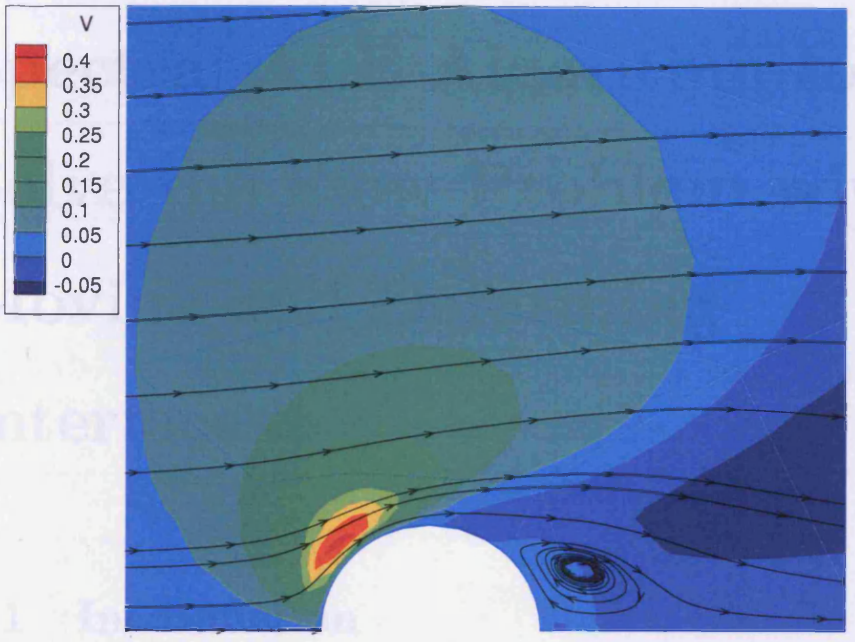

Figure 4.25: Particle tracks (streamlines) with radial velocity contours of the ambient flow over a solid sphere at $Re = 180$.

Chapter 5

Spectral ALE Algorithm to Solve the Flow Problem with Moving and Deforming Interfaces

5.1 Introduction

In this chapter, an arbitrary Lagrange-Eulerian algorithm using spectral element methods to solve microscopic two-phase flow problems with moving boundaries is described. The details of the weak formulation for such a problem are given in Section 5.2. This is based on the variational formulation of the governing equations in Chapter 2, in which the moving mesh velocity is incorporated. The corresponding spectral element approximation of the weak formulation is shown in Section 5.3. Actually this is only a supplement to the temporal and the pressure term discretization discussed in last two chapters, in which the surface tension term that causes a pressure jump is

included. The ALE scheme used in the study is described in Section 5.4. Furthermore, another non-dimensionalization of the governing equations is made to incorporate the two fluid phases. With this new formulation the numerical tests for simulating the deformations of different drops with different flow conditions are performed by changing the Reynolds number, the Weber number, the density ratio, and the viscosity ratio (see Section 5.5). Finally, in Section 5.6 a test case and the comparison with previous research is discussed.

5.2 Weak Formulation Incorporating the Mesh Velocity

The major computational challenge for droplet-gas problems is the deformation of the droplet. The numerical algorithm for solving this problem requires an appropriate treatment of the interface between the fluids and a method to deal with the time-dependent problem in a deforming domain. The former requires a description of the jump in the stress induced by surface tension (for the modelling see Section 2.4), whereas the latter requires an algorithm for remeshing the computational domain.

The shortcomings of pure Lagrangian and Eulerian descriptions for problems with moving boundaries prompted the development of what are known as arbitrary Lagrange-Eulerian techniques. The ALE approach is based on the arbitrary movement of the reference frame, i.e. the reference system is not fixed *a priori* in space or associated with the fluid. It may be considered as a computational reference system that can be chosen quite arbitrarily and is continually changing in order to allow for the precise description of moving

interfaces and to ensure the integrity of the mesh over time. Given a reference frame with velocity $\mathbf{w}$, then the partial time derivative can be evaluated by

$$\frac{\partial}{\partial t} = \frac{\delta}{\delta t} - (\mathbf{w} \cdot \nabla) \tag{5.1}$$

where $\delta/\delta t$ is the time derivative with respect to the moving reference frame. The material derivative is then defined in terms of the ALE derivative by

$$\frac{D}{Dt} = \frac{\delta}{\delta t} + (\mathbf{u} - \mathbf{w}) \cdot \nabla \tag{5.2}$$

When the reference frame is fixed ($\mathbf{w} = 0$) the Eulerian description is recovered. When reference frame follows the motion of the fluid ($\mathbf{w} = \mathbf{u}$) the Lagrangian description is recovered with $\delta/\delta t$ becoming the material derivative.

To incorporate the mesh velocity into the weak formulation of the momentum equations given in Chapter 2, we write, at first, equations (2.20) and (2.21) in compact form as follows

$$\begin{aligned} &\int_{\Omega(t)} \left\{ \frac{\partial u_i}{\partial t} + u_j \frac{\partial u_i}{\partial x_j} \right\} \varphi_i \, dV \\ &= \int_{\Omega(t)} \frac{\partial \varphi_i}{\partial x_i} \, \delta_{i,j} p \, dV + \int_{\partial\Omega(t)} \sigma \, \kappa \, n_i \, \varphi_i \, ds \\ &- \frac{1}{Re_k} \int_{\Omega(t)} \left\{ \frac{\partial \varphi_i}{\partial x_j} \frac{\partial u_i}{\partial x_j} + K_i \frac{u_i}{x_i^2} \varphi_i \right\} dV \qquad \forall \varphi_i \in V_N \,, \end{aligned} \tag{5.3}$$

where $\Omega(t)$ is time dependent and consists of $\Omega_c(t)$ and $\Omega_d(t)$, which are the domains occupied by the two fluids respectively, since the fluids are assumed to be immiscible; $\partial\Omega(t)$ denotes the free interface between the gas and the droplet, ds is the infinitesimal arc length; $Re_k (k = g, d)$ are Reynolds numbers for the two phases, $\delta_{i,j}$ is the Kronecker delta. Here $i, j = 1, 2$ represents

the components so that $\varphi_1 = \varphi_z$, $\varphi_2 = \varphi_r$, $u_1 = u$, $u_2 = v$, $x_1 = z$, $x_2 = r$, $n_1 = n_z$, $n_2 = n_r$, $K_1 = 0$, and $K_2 = 1$. The second term on the right hand side in the above equation is a parametric one-dimensional integral on the interface, in which $\sigma\kappa n_i$ represents a pressure jump. This boundary term arises from the integration-by-parts procedure and provides a natural means for incorporating the force balance accounting for the surface tension into the weak formulation of the problem. This term only contributes to the weak formulation for the test functions that do not vanish on $\partial\Omega(t)$.

Also note that in equation (5.3) the summation convention has been employed. And care must be exercised in defining suitable test functions for the sake of consistency since the function spaces are defined on the time-dependent domain $\Omega(t)$ and the time derivative will depend on the spatial frame of reference. Generally the test functions φ must be independent of time in the reference system i.e.

$$\frac{\delta\varphi_i}{\delta t} = 0 \, .$$

Fortunately, most of the interpolating functions in spectral element methods satisfy this condition, and so do the test functions used here.

Now let us look at the unsteady term in some more detail:

$$\int_{\Omega(t)} \frac{\partial u_i}{\partial t} \varphi_i \, dV = \int_{\Omega(t)} \frac{\partial}{\partial t}(u_i\varphi_i) \, dV - \int_{\Omega(t)} u_i \frac{\partial \varphi_i}{\partial t} \, dV \, . \qquad (5.4)$$

The two contributions to the unsteady term $\varphi_i \, \partial u_i/\partial t$ on the right-hand side of the above equation are defined on different time configurations when discrete time difference is taken. For instance, if $BD2/AB3$ is adopted for the temporal discretization then the unsteady term will be defined on the domain sequence $\Omega(t^{n+1})$, $\Omega(t^n), \Omega(t^{n-1}), \Omega(t^{n-2})$, whereas the integration is

only defined on $\Omega(t)^{n+1}$. This inconsistency can be avoided as follows.

The first term may be rewritten using the Reynolds transport theorem (the general transport theorem) as

$$\int_{\Omega(t)} \frac{\partial(u_i\varphi_i)}{\partial t}\, dV \;=\; \frac{\delta}{\delta\, t} \int_{\Omega(t)} u_i\, \varphi_i\, dV \;-\; \int_{\Omega(t)} \frac{\partial(u_i\varphi_i w_j)}{\partial x_j}\, dV \qquad (5.5)$$

where a field of observers who are moving at velocity $\mathbf{w}$ is defined, and the position of an observer as a function of time can be given by a mesh node. The other contribution can be treated using

$$\frac{\delta\varphi_i}{\delta t} \;=\; \frac{\partial\varphi_i}{\partial t} \;+\; w_j \frac{\partial\varphi_i}{\partial x_j} \;=\; 0$$

thus, we have

$$-\int_{\Omega(t)} u_i \frac{\partial\varphi_i}{\partial t}\, dV \;=\; \int_{\Omega(t)} u_i w_j \frac{\partial\varphi_i}{\partial x_j}\, dV$$

and further considering

$$\int_{\Omega(t)} \frac{\partial(u_i\varphi_i w_j)}{\partial x_j}\, dV \;=\; \int_{\Omega(t)} u_i w_j \frac{\partial\varphi_i}{\partial x_j}\, dV \;+\; \int_{\Omega(t)} \varphi_i \frac{\partial(u_i w_j)}{\partial x_j}\, dV$$

then, we obtain

$$\int_{\Omega(t)} \frac{\partial u_i}{\partial t}\varphi_i\, dV \;=\; \frac{\delta}{\delta\, t} \int_{\Omega(t)} u_i\, \varphi_i\, dV \;-\; \int_{\Omega(t)} \frac{\partial(u_i w_j)}{\partial x_j}\varphi_i\, dV\;. \qquad (5.6)$$

Substituting all of the above relations into equation (5.3) yields

$$\begin{aligned}
\frac{\delta}{\delta\, t} \int_{\Omega(t)} u_i\, \varphi_i\, dV \;&=\; \int_{\Omega(t)} \frac{\partial\varphi_i}{\partial x_i}\, \delta_{i,j} p\, dV \\
&- \frac{1}{Re_k} \int_{\Omega(t)} \left\{ \frac{\partial\varphi_i}{\partial x_j}\, \frac{\partial u_i}{\partial x_j} \;+\; K_i\, \frac{u_i}{x_i^2}\, \varphi_i \right\} dV \\
&+ \int_{\partial\Omega(t)} \sigma\, \kappa\, n_i\, \varphi_i\, ds \\
- \int_{\Omega(t)} \left[\varphi_i u_j \frac{\partial u_i}{\partial x_j} \;-\; \frac{\partial(u_i w_j)}{\partial x_j}\varphi_i \right] dV \qquad & \forall\, \varphi_i \,\in\, V_N\;, \qquad (5.7)
\end{aligned}$$

where the time derivative on the left-hand side may be calculated using the current and previous velocities that are defined on the previous meshes in the mesh moving history.

Through the manipulations in the above, the mesh velocity, which may be controlled independently except for the mesh nodes on the interface, has been brought into the theoretical expression of the moving boundary problem, and the obstacles to the integration of the time derivative in the weak formulation of the momentum equation have been overcome. For the convenience of making a spectral element approximation of the above weak form coincident with the discrete equations derived in Chapter 4, the component form of it is written in the following. Note that the weak formulation of the continuity equation remains the same as that given in Chapter 2 since the flows considered are incompressible, i.e. the density ρ does not change with time. So we have the momentum equations:

$$\begin{aligned}
\frac{\delta}{\delta t}\int_{\Omega(t)} u\,\varphi_z\, r dr dz \;&=\; \int_{\Omega(t)} \frac{\partial \varphi_z}{\partial z}\, p\, r dr dz \\
&- \frac{1}{Re}\int_{\Omega(t)} \left\{ \frac{\partial \varphi_z}{\partial z}\frac{\partial u}{\partial z} + \frac{\partial \varphi_z}{\partial r}\frac{\partial u}{\partial r} \right\} r dr dz \\
&+ \int_{\partial\Omega(t)} \sigma\,\kappa\, n_z\,\varphi_z\, ds \\
&- \int_{\Omega(t)} \varphi_z \left(u\frac{\partial u}{\partial z} + v\frac{\partial u}{\partial r} \right) r dr dz \\
+ \int_{\Omega(t)} \varphi_z \left(\frac{\partial (u w_z)}{\partial z} + \frac{\partial (u w_r)}{\partial r} \right) r dr dz \qquad & \forall\, \varphi_i \in V_N\ ,
\end{aligned} \tag{5.8}$$

and

$$\frac{\delta}{\delta t}\int_{\Omega(t)} v\,\varphi_r\, r dr dz \;=\; \int_{\Omega(t)} \frac{\partial \varphi_r}{\partial r}\, p\, r dr dz$$

$$
\begin{aligned}
&- \frac{1}{Re}\int_{\Omega(t)} \left\{ \frac{\partial \varphi_r}{\partial z}\frac{\partial v}{\partial z} + \frac{\partial \varphi_r}{\partial r}\frac{\partial v}{\partial r} + \frac{v}{r^2}\varphi_r \right\} r dr dz \qquad (5.9)\\
&+ \int_{\partial\Omega(t)} \sigma\,\kappa\, n_r\, ds\\
&- \int_{\Omega(t)} \varphi_r \left(u\frac{\partial v}{\partial z} + v\frac{\partial v}{\partial r} \right) r dr dz\\
&+ \int_{\Omega(t)} \varphi_r \left(\frac{\partial (v w_z)}{\partial z} + \frac{\partial (v w_r)}{\partial r} \right) r dr dz \qquad \forall\, \varphi_i \in V_N\ ,
\end{aligned}
$$

and the continuity equation:

$$
\int_{\Omega(t)} \left\{ u\frac{\partial q}{\partial z} + v\frac{\partial q}{\partial r} + \frac{v}{r}q \right\} r dr dz = 0 \qquad \forall\, q \in Q_N\ . \qquad (5.10)
$$

5.3 Numerical Discretization of the Weak Formulation

Based on the numerical approximation of the Navier-Stokes equations for single phase flow using the spectral element method, described in previous chapters, the numerical discretization of equations (5.8)- (5.10) may be written in the following form. Note that the single spectral element approximation is discussed here and the discretization on the whole computational domain is merely a simple combination of the approximations on the subdomains, each of which is normally occupied by a spectral element. The semi-discrete problem is

$$
\frac{\delta(M\mathbf{u})}{\delta\, t} = D_p^T p - E\mathbf{u} + \mathbf{F} + \mathbf{f} \qquad (5.11)
$$

$$
D\mathbf{u} = 0\ , \qquad (5.12)
$$

where the left hand side can be expressed as follows, if the second order Adams-Bashforth method BD2/AB3 is used

$$
\frac{\delta(M\mathbf{u})}{\delta\, t} \cong \frac{3}{2}M^{n+1}\mathbf{u}^{n+1} - 2M^n\mathbf{u}^n + \frac{1}{2}M^{n-1}\mathbf{u}^{n-1} \qquad (5.13)
$$

here $M^k(k = n+1, n, n-1)$ is the velocity mass matrix at time step k, and

$$M^k \mathbf{u}^k \;=\; M^k \begin{pmatrix} \mathbf{u}_z^k \\ \mathbf{u}_r^k \end{pmatrix}$$

as discussed in Section 4.3, M^k is a diagonal matrix with elements

$$M_{mn} \;=\; \omega_p \omega_q r^k(\xi_p, \eta_q) \left| J_{pq}^k \right| \delta_{mn} \;, \tag{5.14}$$

where $p, q = 0, \cdots, N$ and $m, n = 0, \cdots, (N+1)^2 - 1$. The relation between the local and global counters is given as

$$m, n \;=\; p \times (N+1) + q \;.$$

The physical geometric values $\left| J_{pq}^k \right|$ and r^k are calculated on the mesh at time step k.

Also in equations (5.11)-(5.12), D_p^T is the discrete gradient matrix, D is the discrete divergence matrix, and E is the discrete diffusion matrix. They are all defined in Sections 3.5 and 3.6. Here $\mathbf{F}$ represents the surface tension contributions which are only evaluated on the interface and is given as

$$\mathbf{F} \;=\; S \begin{pmatrix} \sigma_z \\ \sigma_r \end{pmatrix} \;,$$

where S is a $(N+1)^2 \times (N+1)^2$ matrix and its elements can be expressed as

$$S_{mn} \;=\; \omega_q \left\{ \left[\frac{\partial z}{\partial \eta} \right]_{pq}^2 + \left[\frac{\partial r}{\partial \eta} \right]_{pq}^2 \right\}^{1/2} \delta_{mn} \tag{5.15}$$

and

$$\sigma_{\mathbf{z}} = \begin{pmatrix} K\sigma\ \kappa_{00}\ n_z^{00} \\ . \\ . \\ . \\ K\sigma\ \kappa_{pq}\ n_z^{pq} \\ . \\ . \\ . \\ K\sigma\ \kappa_{NN}\ n_z^{NN} \end{pmatrix} \qquad \sigma_{\mathbf{r}} = \begin{pmatrix} K\sigma\ \kappa_{00}\ n_r^{00} \\ . \\ . \\ . \\ K\sigma\ \kappa_{pq}\ n_r^{pq} \\ . \\ . \\ . \\ K\sigma\ \kappa_{NN}\ n_r^{NN} \end{pmatrix}$$

where $p,\ q = 0, \cdots, N$ and $m, n = 0, \cdots, (N+1)^2 - 1$ are local and global counters as explained for equation (5.14), and

$$K = \begin{cases} 1 & when\ (\xi_p, \eta_q)\ \in\ \Omega_d\ , \\ 0 & elsewhere \end{cases}$$

Note that the geometry here is determined by the mesh at $t = (n+1)\Delta t$.

Finally $\mathbf{f} = (f_u, f_v)$ contains all the other contributions which are calculated at previous time steps, and it may be written as

$$\mathbf{f} = \frac{8}{3}\mathbf{c}^n - \frac{7}{3}\mathbf{c}^{n-1} + \frac{2}{3}\mathbf{c}^{n-2} - \frac{8}{3}\mathbf{c}1^n + \frac{7}{3}\mathbf{c}1^{n-1} - \frac{2}{3}\mathbf{c}1^{n-2}\ , \qquad (5.16)$$

where $\mathbf{c}^k$, $k = n, n-1, n-2$ is almost the same as C^n, that has been defined in Section 4.3, except for the moving mesh on which $\mathbf{c}^k$ is calculated, thus we have

$$\mathbf{c}^k = M^k \begin{pmatrix} c_u^k \\ c_v^k \end{pmatrix}\ ,$$

where

$$c_u^k = (c_{u,00}^k, \cdots, c_{u,\,ij}^k, \cdots, c_{u,NN}^k)^T\ .$$

Furthermore $\mathbf{c}1^k (k = n, n-1, n-2)$ is expressed as

$$\mathbf{c}1^k \;=\; M^k \begin{pmatrix} c1_u^k \\ c1_v^k \end{pmatrix} \;, \tag{5.17}$$

where the u-component of $\mathbf{c}1^k$ can be expressed as

$$M^k (c1_{u,00}^k, \cdots, c1_{u,\,ij}^k, \cdots, c1_{u,NN}^k)^T \;.$$

Therefore, as an example, the convective part of the u-momentum equation (5.8), i.e. the last two integrals in the equation, may be written as

$$\begin{aligned} f_u \;&=\; (f_u^{00}, \cdots, f_u^{kl}, \cdots, f_u^{NN})^T \\ &= \frac{8}{3} M^n c_u^n \;-\; \frac{7}{3} M^{n-1} c_u^{n-1} \;+\; \frac{2}{3} M^{n-2} c_u^{n-2} \\ &\quad - \frac{8}{3} M^n c_u^n \;+\; \frac{7}{3} M^{n-1} c_u^{n-1} \;-\; \frac{2}{3} M^{n-2} c_u^{n-2} \;, \end{aligned} \tag{5.18}$$

in which

$$\begin{aligned} f_u^{kl} \;=\; & \frac{8}{3} \sum_{p=0}^{N} \sum_{q=0}^{N} \sum_{i=0}^{N} \sum_{j=0}^{N} c_{u,ij}^n h_k(\xi_p) h_l(\eta_q) h_i(\xi_p) h_j(\eta_q) \omega_p \omega_q r^n(\xi_p, \eta_q) \left| J_{pq}^n \right| \\ & - \frac{7}{3} \sum_{p=0}^{N} \sum_{q=0}^{N} \sum_{i=0}^{N} \sum_{j=0}^{N} c_{u,ij}^{n-1} h_k(\xi_p) h_l(\eta_q) h_i(\xi_p) h_j(\eta_q) \omega_p \omega_q r^{n-1}(\xi_p, \eta_q) \left| J_{pq}^{n-1} \right| \\ & + \frac{2}{3} \sum_{p=0}^{N} \sum_{q=0}^{N} \sum_{i=0}^{N} \sum_{j=0}^{N} c_{u,ij}^{n-2} h_k(\xi_p) h_l(\eta_q) h_i(\xi_p) h_j(\eta_q) \omega_p \omega_q r^{n-2}(\xi_p, \eta_q) \left| J_{pq}^{n-2} \right| \\ & - \frac{8}{3} \sum_{p=0}^{N} \sum_{q=0}^{N} \sum_{i=0}^{N} \sum_{j=0}^{N} c1_{u,ij}^n h_k(\xi_p) h_l(\eta_q) h_i(\xi_p) h_j(\eta_q) \omega_p \omega_q r^n(\xi_p, \eta_q) \left| J_{pq}^n \right| \\ & + \frac{7}{3} \sum_{p=0}^{N} \sum_{q=0}^{N} \sum_{i=0}^{N} \sum_{j=0}^{N} c1_{u,ij}^{n-1} h_k(\xi_p) h_l(\eta_q) h_i(\xi_p) h_j(\eta_q) \omega_p \omega_q r^{n-1}(\xi_p, \eta_q) \left| J_{pq}^{n-1} \right| \\ & - \frac{2}{3} \sum_{p=0}^{N} \sum_{q=0}^{N} \sum_{i=0}^{N} \sum_{j=0}^{N} c1_{u,ij}^{n-2} h_k(\xi_p) h_l(\eta_q) h_i(\xi_p) h_j(\eta_q) \omega_p \omega_q r^{n-2}(\xi_p, \eta_q) \left| J_{pq}^{n-2} \right| \;, \end{aligned}$$

where, for $k = n, n-1, n-2$

$$c_{ij}^k = u_{ij}^k \left(\frac{\partial u^k}{\partial z}\right)_{i,j} + v_{ij}^k \left(\frac{\partial u^k}{\partial r}\right)_{i,j} , \tag{5.19}$$

$$\begin{aligned} c1_{ij}^k = {} & u_{ij}^k \left(\frac{\partial w_z^k}{\partial z}\right)_{i,j} + w_{z,ij}^k \left(\frac{\partial u^k}{\partial z}\right)_{i,j} \\ & + u_{ij}^k \left(\frac{\partial w_r^k}{\partial r}\right)_{i,j} + w_{r,ij}^k \left(\frac{\partial u^k}{\partial r}\right)_{i,j} . \end{aligned} \tag{5.20}$$

The details of $(\partial u^k/\partial z)_{i.j}$ and $(\partial u^k/\partial r)_{i,j}$ can be found in Section 4.3.1, while the derivatives of the mesh velocity may be calculated as

$$\begin{aligned} \left(\frac{\partial w_z^k}{\partial z_k}\right)_{i,j} &= \left(\frac{\partial w_z^k}{\partial \xi}\frac{\partial r^k}{\partial \eta} - \frac{\partial w_z^k}{\partial \eta}\frac{\partial r^k}{\partial \xi}\right)_{i,j} \frac{1}{\mathbf{J}_{ij}^k} \\ &= \left(\frac{1}{\mathbf{J}^k}\frac{\partial r^k}{\partial \eta}\right)_{i,j} \sum_{m=0}^{N}\sum_{n=0}^{N} w_{z,mn}^k h_m'(\xi_p) h_n(\eta_q) \\ &\quad - \left(\frac{1}{\mathbf{J}^k}\frac{\partial r^k}{\partial \xi}\right)_{i,j} \sum_{m=0}^{N}\sum_{n=0}^{N} w_{z,mn}^k h_m(\xi_p) h_n'(\eta_q) \end{aligned} \tag{5.21}$$

and

$$\begin{aligned} \left(\frac{\partial w_r^k}{\partial r_k}\right)_{i,j} &= \left(\frac{\partial w_r^k}{\partial \eta}\frac{\partial z^k}{\partial \xi} - \frac{\partial w_r^k}{\partial \xi}\frac{\partial z^k}{\partial \eta}\right)_{i,j} \frac{1}{\mathbf{J}_{ij}^k} \\ &= \left(\frac{1}{\mathbf{J}^k}\frac{\partial z^k}{\partial \xi}\right)_{i,j} \sum_{m=0}^{N}\sum_{n=0}^{N} w_{r,mn}^k h_m(\xi_p) h_n'(\eta_q) \\ &\quad - \left(\frac{1}{\mathbf{J}^k}\frac{\partial z^k}{\partial \eta}\right)_{i,j} \sum_{m=0}^{N}\sum_{n=0}^{N} w_{r,mn}^k h_m'(\xi_p) h_n(\eta_q) . \end{aligned} \tag{5.22}$$

5.4 ALE Scheme to Solve the Problem of Droplet Deformation

Based on the formulation and the numerical approximation discussed in the last two sections, the arbitrary Lagrangian-Eulerian (ALE) algorithm used in this thesis to solve the the problem of droplet deformation in gas flows is described in the following steps:

1. Form an initial mesh around and within the droplet. Part of the skeleton spectral element mesh Ω_f, which is far away from the droplet, is fixed, while the remain portion Ω_m is allowed to change in time.

2. Start with an initial solution at time $t = 0$, for instance gas and droplet at rest or the velocity field determined by solving an associated problem for a fixed solid sphere the same size as the droplet at the same Reynolds number.

3. Solve the equations presented below for flow field $\mathbf{u}(\mathbf{x}[z(\xi,\eta), r(\xi,\eta)], t^n)$ and $p\ (\mathbf{x}[z(\xi,\eta), r(\xi,\eta)], t^n)$ using the preconditional conjugate gradient method described in Section 4.4 and the boundary conditions for circular channel flows or ambient flows in the way of traditional CFD (this is the Eulerian part of the scheme). Zero mesh velocity may be selected for the first step of time marching, and a new mesh velocity to carry on the solving procedure can be calculated in the way explained in step 4 after the first field results are obtained.

   By rearranging the equations (5.11)-(5.13) we have

$$(\frac{3}{2}M^{n+1} + E^{n+1})\mathbf{u}^{n+1} - (D_p^{n+1})^T \mathbf{t}p^{\,n+1} = \mathbf{r} \qquad (5.23)$$

$$D^{n+1}\mathbf{u}^{n+1} = 0\ , \qquad (5.24)$$

where the term on the right-hand side of (5.23) is

$$\mathbf{r} = 2M^n\mathbf{u}^n - \frac{1}{2}M^{n-1}\mathbf{u}^{n-1} + \mathbf{F}^{n+1} + \mathbf{f}\,. \tag{5.25}$$

The Uzawa operator $D^{n+1}(\frac{3}{2}M^{n+1} + E^{n+1})^{-1}(D_p^{n+1})^T$ is almost the same as that given in Section 4.4.2 and is positive semi-definite as well as symmetric, so that the discrete system may be solved using the PCG iterative method that has been discussed in detail in Section 4.4. Note that different fluid properties ought to be given to the two phases respectively, which are represented by Ω_g and Ω_d.

4. Move from time t^n to t^{n+1} by performing the loop described as follows:

   - Calculate the mesh movement by solving

$$\frac{dX_i^{n+1}}{dt} = w_i^{n+1} \tag{5.26}$$

     to determine the positions of the new vertices on the skeleton spectral element mesh corresponding to Ω_m. As mentioned in step 1, to avoid large scale remeshing at each time step the computational domain is decomposed into two zones, Ω_m and Ω_f. The former, associated with a region surrounding the droplet, is allowed to deform in time while the latter is fixed for all time. In the above equation $i = 1, 2$, $X_1^{n+1} = z^{n+1}$ and $X_2^{n+1} = r^{n+1}$, and w_i^{n+1} are the components of the mesh velocity. We also use the following equation to manipulate the movement of the skeleton vertices, which accounts for recent history of the mesh moving:

$$\frac{1}{\Delta t}[X_i^{n+1} - X_i^n] = \frac{3}{2}w_i^n - \frac{1}{2}w_i^{n-1} \tag{5.27}$$

     In this way, an initial mesh velocity needs to be given.

The skeleton vertices mentioned in the above do not include the nodes on the interface. Not only the vertices of the skeleton spectral element mesh but also the sub-mesh nodes on the interface corresponding to the Gauss-Lobatto points need to be moved exactly with the velocity field for the purpose of tracking the droplet deformation accurately. This means that

$$\mathbf{w} = \mathbf{u} \tag{5.28}$$

i.e.

$$w_z = u \qquad w_r = v \tag{5.29}$$

needs to be ensured on the interface.

Since the four sides of a spectral element are exactly parameterizable by polynomials of the same order as the spectral approximation, we can obtain the new shape of the interface at time t^{n+1} using an isoparametric mapping that interpolates the new positions of the nodes on the interface. These new nodes are calculated using equation (5.26). In the case of spectral elements that border the interface, a 1D isoparametric mapping is used to represent the side that is on the interface. This is then blended with exact parameterizations of the other sides using equation (3.37) to obtain a hybrid transfinite/isoparametric mapping for the spectral element grid (see Section 3.4.3 for the details). This technique is widely used in finite element methods and has been used in conjunction with the spectral element method by Korczak and Patera (1986).

The new grids for other spectral elements that are not adjacent to

the interface can be obtained using equation (3.31), using a pure linear transfinite mapping. After the new mesh is determined as a whole, the velocity $\mathbf{w}$ at other mesh nodes may be solved using equation (5.26).

- Update the matrices $M^{n+1}, E^{n+1}, D^{n+1}, D_p^{n+1}, M^n,\ M^{n-1}, F^{n+1}$, etc.
- Solve for the flow field (velocity and pressure) at the new time level using the PCG method as explained in step 3.
- Obtain the new velocity for the spectral element vertices, then go back to the beginning of step 4 and repeat.

Spectral element methods may need more computer memory and CPU time to solve the field problems than other traditional CFD methods because of the higher order interpolations used. However, the PCG solver developed in Chapter 4 does not claim much memory associated to the storage of discrete spectral element operators as no direct inversion is needed. Apart from this, the ALE scheme has the following advantages:

There are a number of advantages in using the implicit scheme (5.23)-(5.24) for problems involving droplet deformation. For droplets characterized by a low Weber number, the time step for an explicit method is restricted by the time scale associated with surface tension. For most low Weber number simulations, the droplet remains almost spherical and so there is no need to resolve this time scale. Furthermore, the viscosity of the droplet is generally much higher than that of the gas. This means that the circulation in the drop is all but eliminated. However, an explicit scheme would be limited by the diffusive time scale associated with the interior of the droplet. There are also no difficult choices to be made concerning the interfacial boundary

conditions.

The physical movement of the mesh nodes along the interface is well followed as long as the time step is small enough, and with the spectral element method the droplet shape is more accurately tracked because higher order interpolations are used to deform the geometry of the interface. Comparing with previous work (Helenbrook and Edwards 2000), it seems that less quadrilateral elements than triangular ones are needed to conform the complex geometry of deformed droplet.

In theory, the velocity of any mesh node can be arbitrarily designated to follow the drop movement and handle the topological deformation of the moving mesh in the mean time. With this ALE scheme only the vertices of the spectral elements need to be controlled for the above two purposes. This is a great convenience. As described in step 4, the movement of all the mesh nodes can be determined after remeshing, that is, in fact, the transfinite or mixed isoparametric/transfinite interpolations to the velocities of the spectral element vertices. Furthermore, the trivial work from the projection after remeshing is saved because of the incorporation of the the mesh velocities into the weak formulation of the governing equations, which is usually not avoidable for other algorithms.

5.5 Non-dimensionalization for the Problem of Droplet Deformation

The efficient analysis of the two-phase problem of droplet deformation requires a suitable non-dimensionalization of the governing equations.

Let the two fluids be contained in a domain $\Omega = \bigcup_{el} \Omega_{el}$, $el = 1, \cdots, K$,

where K is the number of the spectral elements. The region occupied by fluid k is Ω_k, $k = 1, 2$. Since the fluids are assumed to be immiscible we have $\Omega = \bigcup_k \Omega_k$. Let $\partial\Omega$ denote the interface between the two fluids. Let $\mathbf{n}$ denote the unit normal to $\partial\Omega$ and $\mathbf{t}$ the unit tangent to $\partial\Omega$. Then equations (2.11)-(2.13) can be written in the following form:

$$\nabla \cdot \mathbf{u}_k = 0 \ , \tag{5.30}$$

$$\rho_k \left(\frac{\partial \mathbf{u}_k}{\partial t} + \mathbf{u}_k \cdot \nabla \mathbf{u}_k \right) = -\nabla p + \nabla \cdot \mathbf{T}_k \ , \tag{5.31}$$

where $\mathbf{u}_k$ is the velocity field, ρ_k is the density, p is the pressure, and $\mathbf{T}_k$ is the extra-stress tensor (viscous) associated with fluid k. The Cauchy stress tensor is defined by

$$\boldsymbol{\sigma}_k = -p\,\mathbf{I} + \mathbf{T}_k \ .$$

The conditions along the interface are the continuity of the normal and tangential velocities are

$$\mathbf{u}_1 \cdot \mathbf{n} = \mathbf{u}_2 \cdot \mathbf{n} \ , \tag{5.32}$$

$$\mathbf{u}_1 \cdot \mathbf{t} = \mathbf{u}_2 \cdot \mathbf{t} \ , \tag{5.33}$$

and the force balance at the interface

$$(\boldsymbol{\sigma}_2 - \boldsymbol{\sigma}_1) \cdot \mathbf{n} = \sigma \kappa \mathbf{n} \ , \tag{5.34}$$

where σ is the surface tension coefficient and κ is the local radius of curvature of the interface. The local radius of curvature can be written in the form

$$\kappa = \left(\frac{1}{R_1} + \frac{1}{R_2} \right) \ , \tag{5.35}$$

where R_1 and R_2 are the principal radii of curvature. Without loss of generality, if the centre of curvature lies in fluid 1 then we let $\mathbf{n}$ point into Ω_1 and the radius of curvature be positive.

Now consider flow of a gas (g) past a liquid droplet (d). The governing equations are made dimensionless by scaling length by L, velocity by U, time by L/U and pressure and extra-stress by $\eta_g U/L$. The dimensionless momentum equation in the gas then becomes

$$Re\left(\frac{\partial \mathbf{u}_g}{\partial t} + \mathbf{u}_g \cdot \nabla \mathbf{u}_g\right) = -\nabla p + \nabla \cdot \mathbf{T}_g \ , \tag{5.36}$$

where the Reynolds number is defined by

$$Re = \frac{\rho_g U L}{\eta_g} \ .$$

The dimensionless momentum equation in the liquid region is

$$\bar{\rho} Re\left(\frac{\partial \mathbf{u}_d}{\partial t} + \mathbf{u}_d \cdot \nabla \mathbf{u}_d\right) = -\nabla p + \nabla \cdot \mathbf{T}_d \ , \tag{5.37}$$

where the dimensionless density ratio $\bar{\rho} = \rho_d/\rho_g$. The extra-stress tensors in the two fluids are

$$\mathbf{T}_g = 2\mathbf{d_g}, \quad \mathbf{T}_d = 2\bar{\eta}\mathbf{d}_d \ , \tag{5.38}$$

where $\bar{\eta}$ is defined as the dimensionless viscosity ratio defined by $\bar{\eta} = \eta_d/\eta_g$. The dimensionless form of the force balance at the interface is

$$\left(\frac{\eta_g U}{L}\right)(\boldsymbol{\sigma}_d - \boldsymbol{\sigma}_g) \cdot \mathbf{n} = \frac{\sigma}{L}\kappa \mathbf{n} \ . \tag{5.39}$$

On rearrangement this becomes

$$(\boldsymbol{\sigma}_d - \boldsymbol{\sigma}_g) \cdot \mathbf{n} = \left(\frac{\sigma}{\eta_g U}\right)\kappa \mathbf{n} \ . \tag{5.40}$$

Now we can write

$$\frac{\sigma}{\eta_g U} = \left(\frac{\rho_g U L}{\eta_g}\right)\left(\frac{\sigma}{\rho_g U^2 L}\right) \ .$$

Finally, if we define the Weber number by

$$We = \frac{\rho_g U^2 L}{\sigma} \ ,$$

the dimensionless form of the force balance across the interface becomes

$$(\boldsymbol{\sigma}_d - \boldsymbol{\sigma}_g) \cdot \mathbf{n} = \left(\frac{Re}{We}\right) \kappa \mathbf{n} \ . \tag{5.41}$$

The Weber number represents the ratio of the external aerodynamic or inertia forces to the surface tension force. Thus the Weber number provides a relative measure of the influence of the inertia and surface tension forces and their effects on droplet deformation. If the Weber number is small, then this implies that surface tension effects are important. The surface tension force at an interface between two fluids depends on the curvature of the interface. In general, for an arbitrarily shaped surface, the principal radii of curvature R_1, R_2 are difficult to determine either theoretically or numerically. In the present work where we deal with an axisymmetric surface the principal radii of curvature can be determined relatively easily. Let the interface be described parametrically by the curve $z = z(s)$, $r = r(s)$, where s is measured along the interface. Then the radii of curvature for the axisymmetric surface that were given in Section 2.5 may be rewritten as

$$\frac{1}{R_1} = \frac{z'r'' - r'z''}{[(z')^2 + (r')^2]^{3/2}}, \quad \frac{1}{R_2} = \frac{z'}{r[(z')^2 + (r')^2]^{1/2}}, \tag{5.42}$$

where the primes denote differentiation with respect to s. Since an isoparametric representation of the boundary along an interface is used within the spectral element discretization, a polynomial expression for the curve $(z(s), r(s))$ exists and can be differentiated easily.

The discrete matrix formulation of equations (5.30)-(5.31) is almost the same as equations (5.23)-(5.25) except that some constant coefficients in the matrices such as M, E, F, $\mathbf{f}$ need to be replaced by $\bar{\eta}$, $\bar{\rho}$, Re and We or their combinations.

5.6 Validation of Drop Deformation

As discussed in detail in chapter 4, the problem of flow over a sphere may be viewed as a test case for the flow over a deformable droplet since in the limit of large $\bar{\eta}$ and small Weber number the behavior of a liquid droplet is almost the same as that of a solid sphere. To validate the ALE scheme and to test the two-fluid aspects of the formulation, in this section we calculate a transient solution for a moving liquid drop in an uniform ambient gas flow.

The droplet is placed in the middle of the computational domain, the geometry of which is the same as that used in Section 4.6. The domain is divided into two parts Ω_m and Ω_f, where Ω_m is allowed to move and Ω_f is fixed as shown in Fig. 5.1. The mesh structure of the gas region Ω_g is also the same as that shown in Fig. 4.19, which is constructed using 20 spectral elements, whereas the mesh for the droplet, as described in Fig. 5.2, includes 6 spectral elements.

The boundary conditions given in Section 4.6 are used here, i.e. the uniform distributions of axial velocity for inlet and outlet, the slip wall condition for both top and bottom sides, zero radial velocity for the axisymmetric axis etc. The simulation of drop deformation starts from a developed Navier-Stokes flow over a solid sphere of the same size as that of the droplet. The liquid to gas density and viscosity ratios are $\bar{\rho} = 100$ and $\bar{\eta} = 100$. The Reynolds number based on the gas properties is 600 which is comparable to the Reynolds number 60 in the previous work (Helenbrook 2001) because the radius of the whole region is taken as the length scale, and the Weber number of the drop is 4.

This case is very similar to the previous work down by Helenbrook (2001)

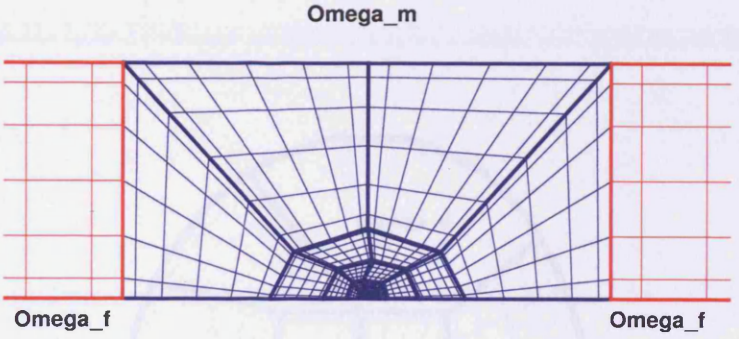

Figure 5.1: Domain divided into two parts: the moving part Ω_m (blue) and the fixed part Ω_f (red).

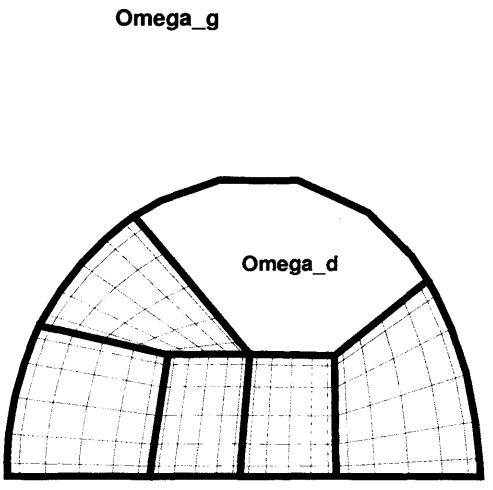

Figure 5.2: Ω_g and Ω_d and mesh structure of the droplet area.

and Dandy and Leal (1989), respectively. In these previous calculations, a falling liquid drop in a gaseous environment is simulated, in which the droplet deformation is driven by the reaction force to the gravity of the drop and the surface tension, while in our case the deformation is driven by the surface tension and an uniform axial velocity field around the drop. Furthermore, the viscous interfacial condition is applied for both cases, that means a continuous velocity field across the interface, and the relative velocity field about the droplet is also similar.

The calculations are performed with $N = 4$ and $N = 6$ as well as a number of values for the time step. The same criteria as that used for the solid sphere problems are taken for the convergence of the Uzawa and Helmholtz operators although more iterations are needed.

From the process of the numerical simulation, it is observed that the droplet starts to move and deform smoothly from the front whilst the rear part of the droplet close to the symmetry axis remains stationary initially, and then accelerating and translating with the gas flow. Then the droplet reduces in axial direction and extends in the radial direction. As the drop translates its peak moves downstream relative to its centre and forms a typical cup-like shape deformation. The droplet shape at $t = 0.24$ is shown in Fig. 5.3. Here the time unit is non-dimensional and $\Delta t = 10^{-3}$ and $N = 6$. Fig. 5.3 also shows the radial velocity contours. The droplet shape seems to stablilize after this time.

The results are comparable to previous work. From this calculation, the ratio of deformation along the symmetric axis is 0.821 and the ratio of change on the height of drop is 1.150, whereas the same data from the previous simulation (Helenbrook 2001) are 0.793 and 1.152. Since the reaction force comes

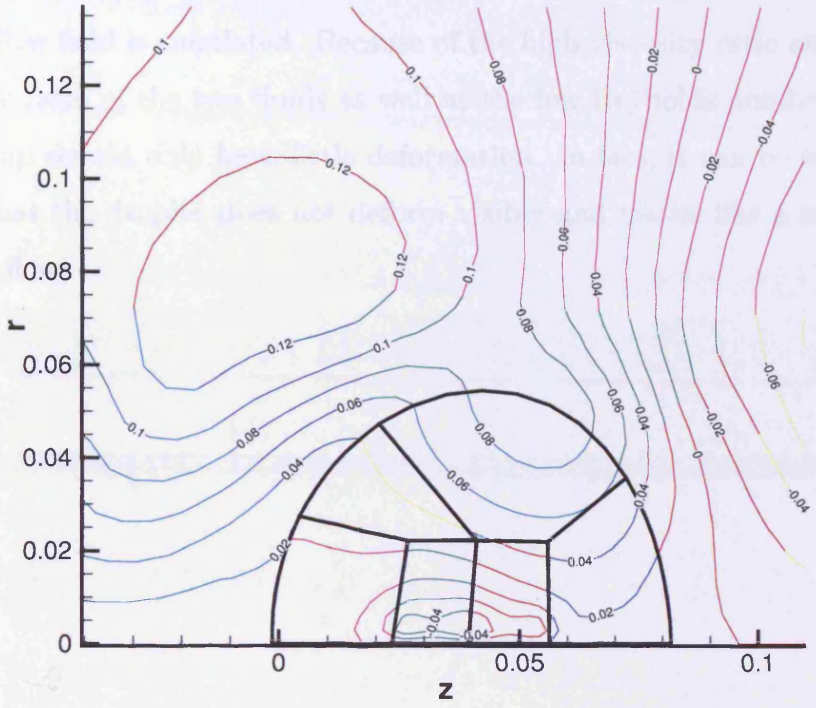

Figure 5.3: Droplet shape and radial velocity contours at $t = 0.24$ for the test case with $Re = 60$ and $We = 4$.

from the direction that acts against the the moving drop in the falling droplet problem and the flow field in our case drives the drop move forward, the drops flatten in opposite ways as shown in Fig. 5.3 and Helebrook (2001). We also note that with the low Reynolds number and moderate Weber number, our mesh moving scheme worked well and performed easily and satisfactorily.

Although there are differences in flow circumstances between the problem presented here and previous work, one can see that the ALE scheme employed is successfully validated. One more calculation, which may be consid-

ered as a further validation of the algorithm will be presented in Chapter 6 and shown in Fig. 6.23, where the deformation of a vegetable oil droplet in a gas flow field is simulated. Because of the high viscosity ratio and the high density ratio of the two fluids as well as the low Reynolds number adopted, the drop should only have little deformation. In fact, it can be seen in Fig. 6.23 that the droplet does not deform visibly and moves like a solid sphere in the flow.

Chapter 6

The Prediction of Droplet Deformation Using the Spectral ALE Method

6.1 Introduction

Deformation of fluid elements in a flow stream of a secondary fluid is a precursor to fluid breakup, and a highly influential and fundamental process in heat and mass transfer and atomisation problems. These problems occur in a diverse range of applications both in industry and nature, from the efficient utilisation of liquid fuel in internal combustion and gas turbine engines to the atomisation of blood particles in criminology cases. A typical image of a water droplet deforming and breaking up in a gas stream is presented in Fig. 6.1.

In this chapter, various direct simulation results produced by the numerical model using the spectral ALE scheme for the deformation of Newtonian

Figure 6.1: Photo image of a water drop deforming in a gas flow.

drops possessing different physical properties in different flow circumstances are presented. This begins, in Section 6.2, by presenting the results for a variety of computational experiments, and investigating the influence of the 4 dimensionless groups, i.e. Reynolds and Weber number, density and viscosity ratios. Results are mainly presented in terms of droplet boundary deformation, flow field contours and streamlines for qualitative trends. Although the properties of the selected benchmark droplet are close to those of common engine fuels, some other practical applications such as the deformation of a vegetable oil droplet in air flow are also given, which show the significant difference in the deformation processes. In section 6.3, some further results are discussed in the context of applications, including the investigation of problems of gas flows over a hexane droplet, in which a quantitative analysis of the selected kinematic variables for the droplet deformation is given with details. The dimensionless values are also used in this section to analyse the

effects of changes in the properties of fluids and the gas flow conditions.

6.2 Qualitative Study of Droplet Deformation for Various Fluid and Flow Conditions

To investigate droplet deformation and develop a fundamental understanding of a range of practical problems, numerical experiments are undertaken through varying the four non-dimensionalised groups mentioned in section 6.1. Varying each of these groups independently can be related to a physical problem or various empirical findings in the literature. The Weber numbers presented are specifically chosen to represent the region usually associated with droplet breakup, namely $1 \leq We \leq 15$. As a temporal, quasi-3D, moving boundary problem, the results may be compared and quantified in various ways. Here, the following qualitative and quantitative measures have been chosen to compare and contrast deformations resulting from different dimensionless parameters.

6.2.1 Prediction of Traditional Droplet Deformation/Flow Characteristics

Figs. 6.2 -6.6 show the transient development of boundary deformation of a Newtonian drop in a gas flow with the non-dimensionless parameters chosen as $We = 15, Re = 1000, \bar{\eta} = 15$ and $\bar{\rho} = 500$. The transient process starts at $t = 0$ in the initial field of axial Stokes flow past a solid sphere that has the same size as the droplet and is also positioned at $z = 0$ and $r = 0$, consistent with the initial droplet position.

From the time sequence, one can see that the droplet starts accelerating with the flow due to the drag force from the gas, and also smoothly starts to deform, reducing its horizontal diameter from the side facing the direction of flow, whilst elongating in the vertical direction. As the droplet translates, its summit moves in the direction of the flow, and relatively to the nominal center of the moving, deforming droplet. A schematic diagram illustrating the key quantitative measurements associated with the translation and deformation of the droplet is given in Fig. 6.10.

Fig. 6.6 gives the shape of the drop at $t = 0.33$. Here, the onset of one of the traditional modes of breakup may be recognised, with the droplet Y value (see Fig 6.10) increasing (i.e. the appearance of the so-called bag shape) and the peak of the drop moving in the direction of flow relative to the the 'centre' of the droplet, giving a positive k value (see Fig. 6.10). In time, droplet fragmentation would occur first at the leading edge of the drop in the direction of flow. We take this case as the benchmark problem for the calculations in this chapter due to its established characteristic feature.

The deformed drop shown in Figs. 6.2-6.6 is calculated using $N = 6$ and $\Delta t = 10^{-3}s$. To balance the cost and accuracy of the calculation, the benchmark case has been calculated using different polynomial orders and time step values. The average time spent for one time step calculation with different N and Δt on one of our PC workstations equipped for this research is listed in Table 6.1, where the unit represents one minute of real time taken for the calculation.

Although faster convergence is achieved with smaller Δt, the least total time is spent with largest Δt. We also notice that the droplet boundary is tracked more accurately with $N = 6$ than with lower orders, whereas higher or-

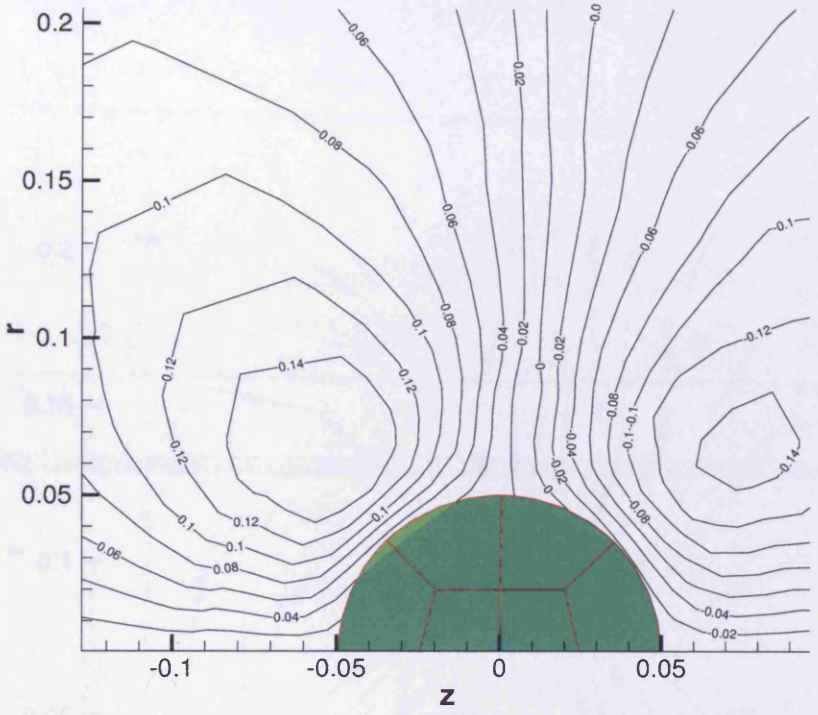

Figure 6.2: Predicted droplet shape with radial velocity magnitude contours at $t = 0.03$ in the deformation and translation for the benchmark Newtonian problem.

Δt	3×10^{-3}	1×10^{-3}	3×10^{-4}
$N = 4$	7.5	4.8	2.0
$N = 6$	27.1	18.9	6.7
$N = 8$	69.3	15.9	–

Table 6.1: Time taken for one step of time marching vs N and Δt, where the unit time is a minute.

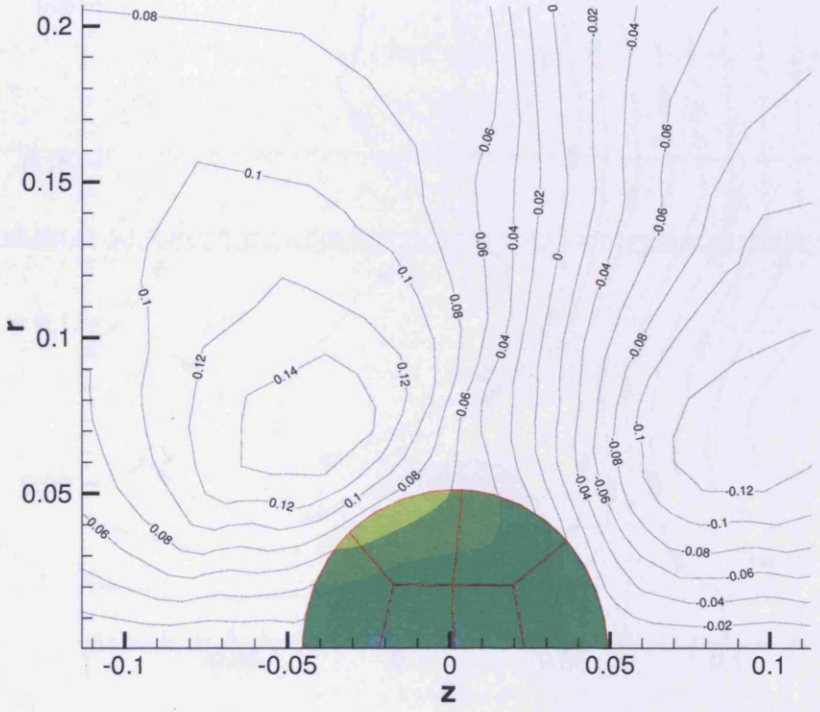

Figure 6.3: Predicted droplet shape with radial velocity magnitude contours at $t = 0.06$ in the deformation and translation for the benchmark Newtonian problem.

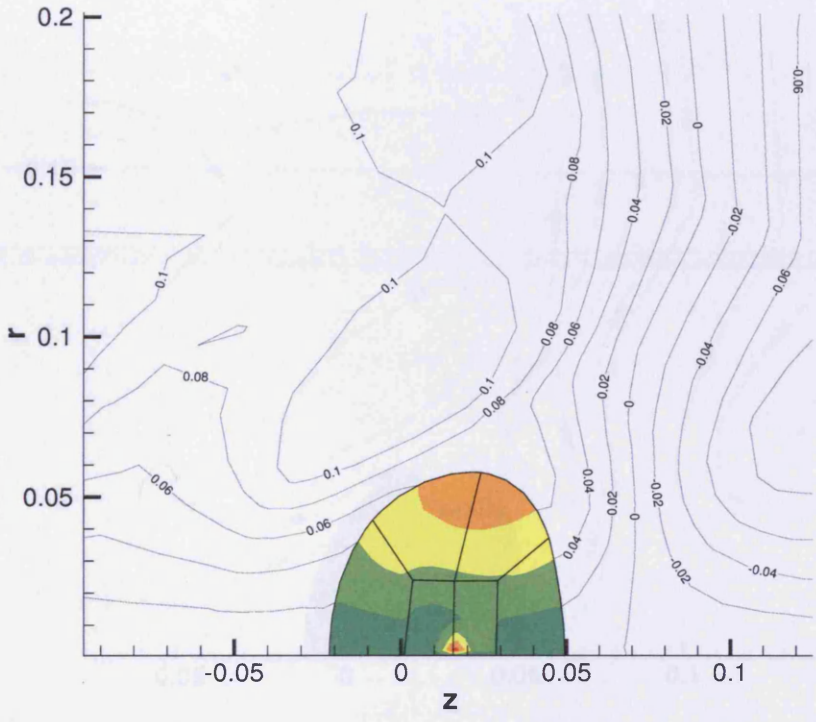

Figure 6.4: Predicted droplet shape with radial velocity magnitude contours at $t = 0.15$ in the deformation and translation for the benchmark Newtonian problem.

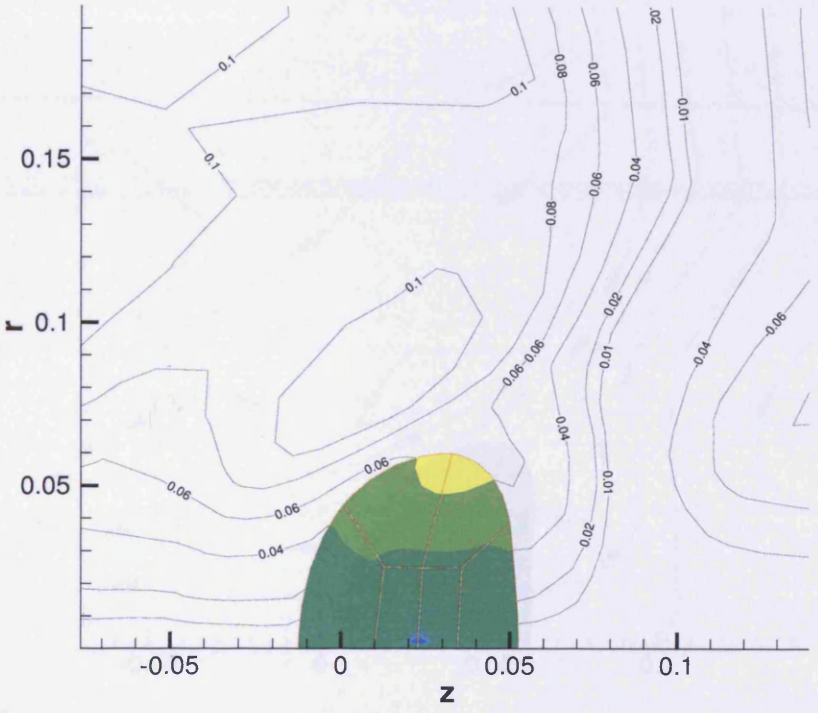

Figure 6.5: Predicted droplet shape with radial velocity magnitude contours at $t = 0.27$ in the deformation and translation for the benchmark Newtonian problem.

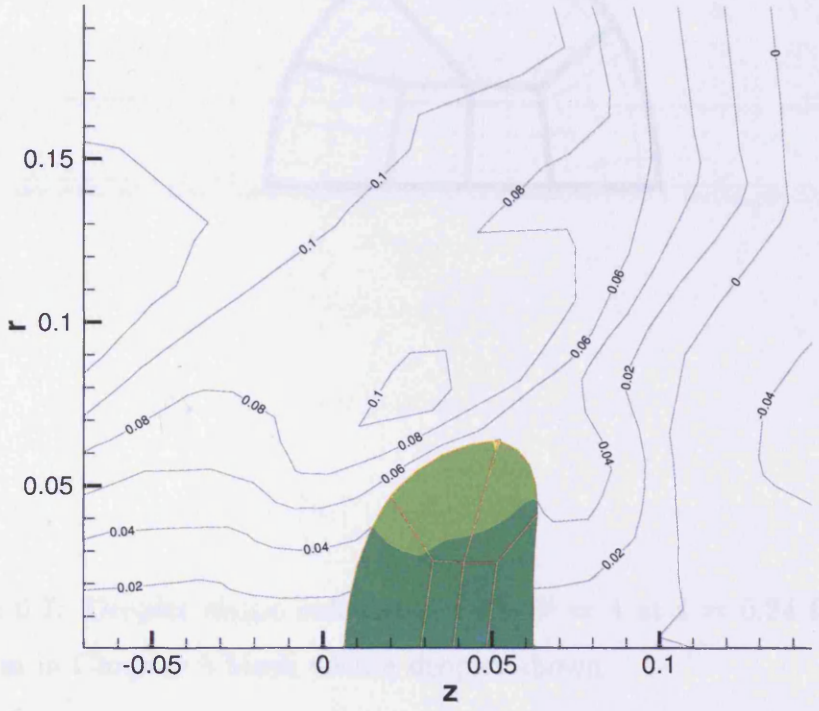

Figure 6.6: Predicted droplet shape with radial velocity magnitude contours at $t = 0.33$ in the deformation and translation for the benchmark Newtonian problem.

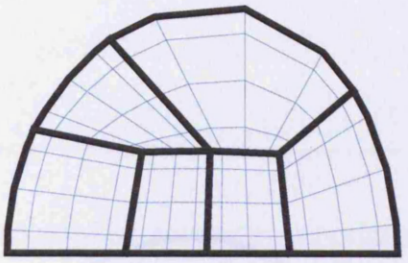

Figure 6.7: Droplet shape calculated with $N = 4$ at $t = 0.24$ for the test problem in Chapter 5.Mesh within droplet shown

der ($N > 6$) simulations may not improve the accuracy significantly. This is shown in Figs. 6.7-6.9. Therefore, the calculations with $N = 6$ and $\Delta t = 10^{-3}$ usually provide accurate information of droplet boundary translation, and keep the cost at a reasonable level, whereas $N = 4$ and $\Delta t = 3{\times}10^{-3}$ are often used in numerical experiments to analyse the trend of droplet deformation.

Whilst the qualitative representation is interesting to identify trends in global variations, it is informative to quantify the geometrical transformation oc-

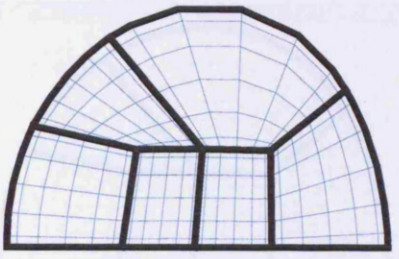

Figure 6.8: Droplet shape calculated with $N = 6$ at $t = 0.24$ for the test problem in Chapter 5.

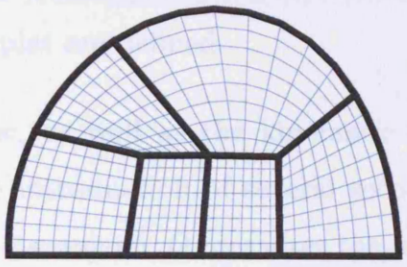

Figure 6.9: Droplet shape calculated with $N = 8$ at $t = 0.24$ for the test problem in Chapter 5.

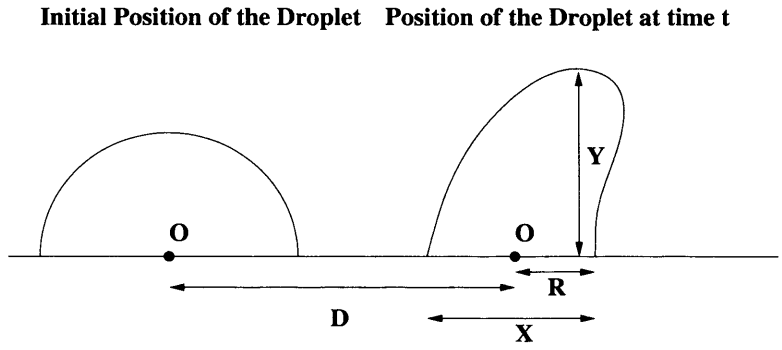

Figure 6.10: Schematic diagram illustrating the deformation of a liquid droplet. Key quantitative measurements associated with the translation and deformation of the droplet are defined.

curring within the flow, as well as the kinematic characteristics. This is facilitated through the introduction of several secondary variables, defined in Fig. 6.10. Here, the parameter D measures the translation of the droplet and is defined to be the distance of the nominal center, o, of the droplet at time t from the initial center of the droplet. The parameter X measures the axial width of the droplet at time t, and k is the axial distance between the centre and the peak of the drop. When $t = 0$, k is 0 and X is just the diameter of the droplet. The parameter Y measures the maximum extension of the droplet in the vertical direction. When $t = 0$, Y is the radius of the droplet.

Figs. 6.11 and 6.12 show the droplet deformation in time with low Weber number ($We = 3$) and other parameters unchanged compared with the benchmark case. Here the interesting behavior is that the drop first expands in the direction of the flow from $t = 0.03$ to $t = 0.12$ before distinctly increasing its Y value with a corresponding decrease in the meridian direction. The fact that the drop is not held in the flow by a body force, as prescribed in

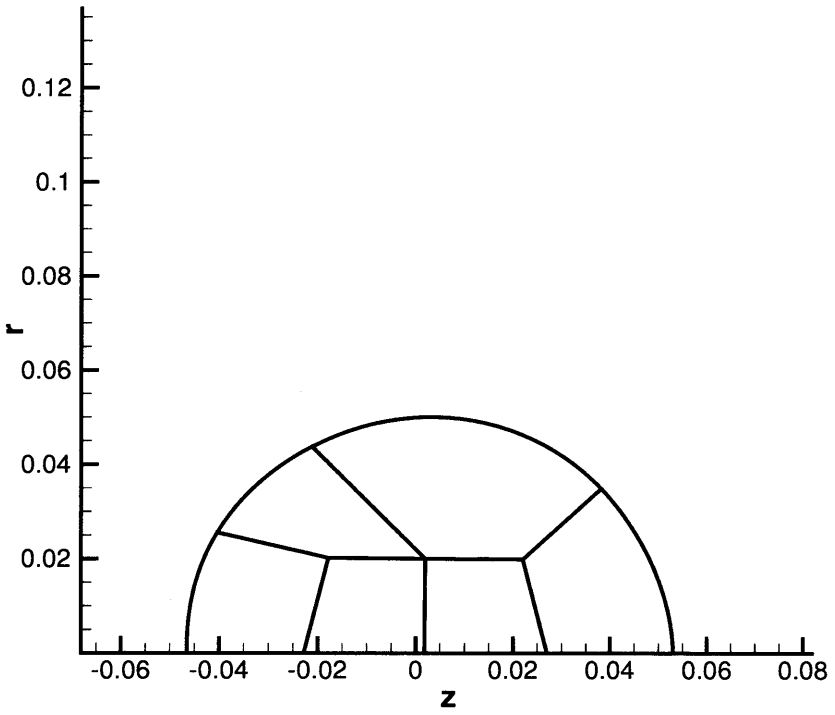

Figure 6.11: Droplet shape calculated for low Weber number case $We = 3$ at $t = 0.09$.

some previous work, is noted by the translation of the droplet in the downstream direction, having moved from the origin to approximately $x = 0.0155$ by $t = 0.21$. This contrasts considerably with the photographic evidence provided in Fig. 6.1, which is consistent with model predictions for higher Weber number.

The suppression of the leading edge curvature is likely to lead to delayed onset of droplet breakup, which is consistent with the model predictions associated with increasing the Weber number (in our case, from 1 to 15).

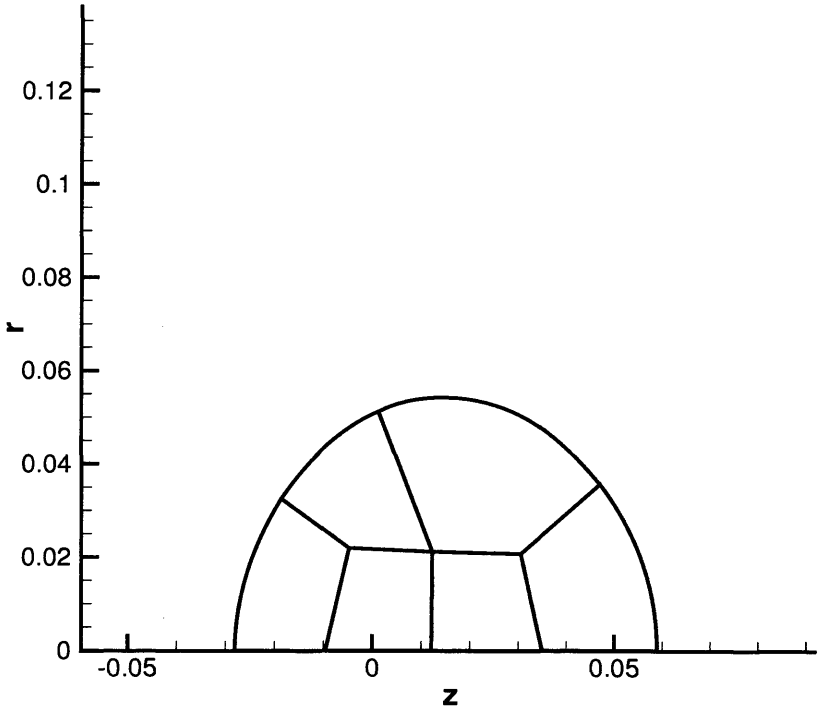

Figure 6.12: Droplet shape calculated for low Weber number case $We = 3$ at $t = 0.18$.

There is an interdependence of interface deformation with internal and external flow fields, and hence an indirect link between internal flow structures and droplet fragmentation. It is informative to explore both internal and external flow qualitatively to investigate regions of vorticity. At this stage, it should be noted that it is difficult to precisely define streamlines between the two fluids due to the droplet translating within the flowstream, i.e. the movement relative to the driven flow field, as well as flowing within its boundary. Figure 6.13 shows the internal liquid (the fluid of drop) flow field relative to the moving drop in an attempt to highlight regions of recirculation within the droplet, which may otherwise be masked by the translation of the drop itself. This is not a trivial task and has been undertaken numerically by subtracting the averaged velocity of the droplet from the droplet velocity on all the mesh nodes.

The streamlines presented in Fig. 6.14 are enlightening, in the sense that there is strong evidence of the leading toroidal vortex (rotated round the axis of symmetry) creating the droplet cusp that subsequently leads to fragmentation at the leading edge. The vorticity in the external flow behind the droplet is characteristic of flow behind a bluff body such as a sphere. This shows obviously the evidence of the interdependence of the internal and the external flows in the local region of the droplet, which gives rise to the deformation of the interface (or the drop boundary) and subsequent breakup.

6.2.2 Effect of Variation in Initial Weber Number

As the droplet is free to move in the mathematical formulation, the droplet is predicted to translate along the flow direction. In practice, of course, this means that the true Weber number based on the relative velocity between driven flow and drop is also time-dependent. However what is used here is

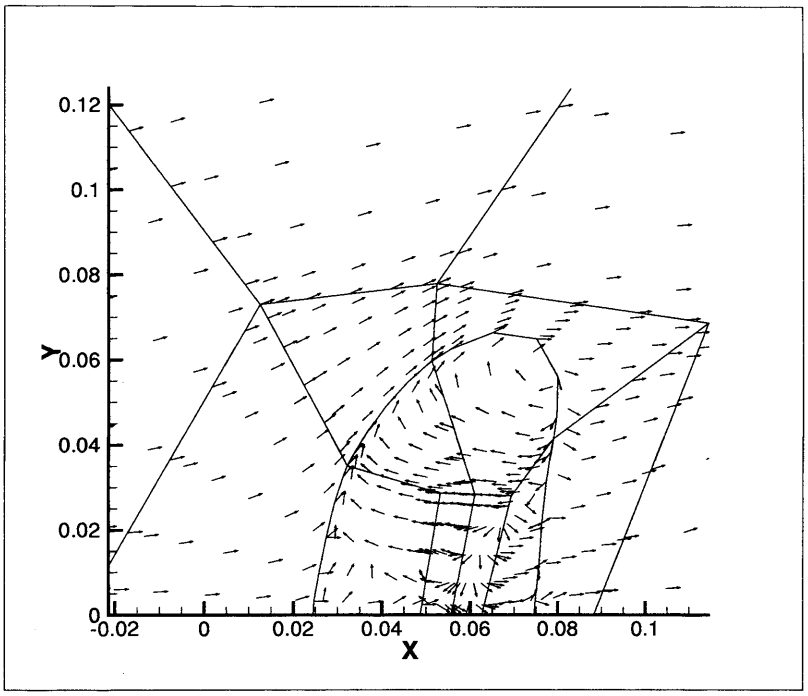

Figure 6.13: Vector representation within droplet during deformation for the benchmark case at $t = 0.35$, the coordinates X and Y corresponding to axial and radial directions repectively.

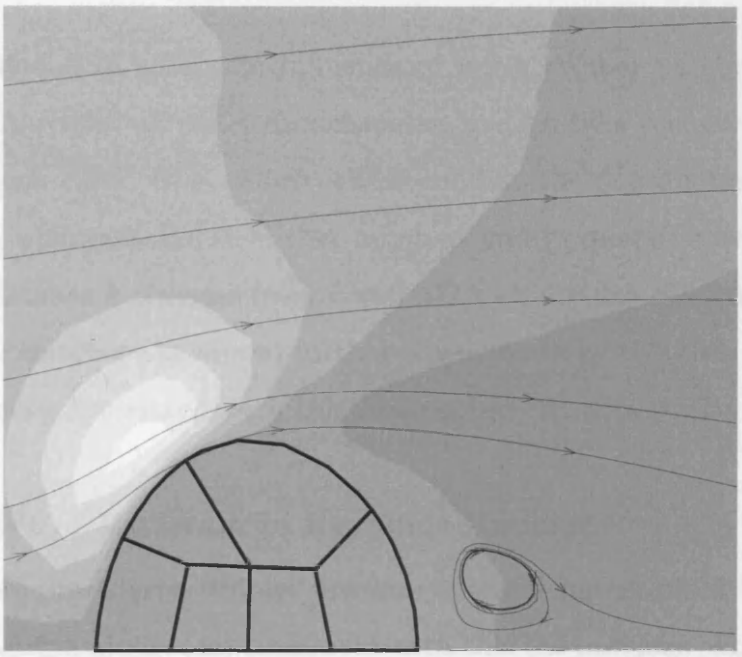

Figure 6.14: Streamlines of a gas flow over a drop with the contours of velocity magnitude, and the flow structure behind the droplet.

the Weber number at the initial moment.

This Weber number is used in submodels embedded within many generalised CFD codes as the sole indicator of droplet breakup, due to its representation of the competition between the surface tension and aerodynamic 'stripping' forces. Therefore, one expects a strong influence of droplet Weber number in the droplet deformation process.

Figs. 6.15 and 6.16 show the influence of initial Weber number variation when $t = 0.3$, whilst all other dimensionless groups take the same values as the benchmark case. It is clearly observed that the deformation increases significantly with increase in Weber number, and in quantifiable terms, the peak drift distance k changes from $k = 0.002$ to $k = 0.018$. The droplet with larger Weber number has moved further downstream by this time, due to the increase in drag associated with the larger projected area of the droplet.

6.2.3 Effect of Variation in Reynolds Number

As mentioned previously, droplet breakup is often characterised by a Weber number condition alone, and consistent with this the previous subsection has shown the significant influence that Weber number has upon droplet deformation. Unlike the experimental studies, with the mathematical formulation derived in the previous chapter and adopted for the numerical tests within this chapter, it is straightforward to decouple the influence of initial Weber and Reynolds numbers.

Fig. 6.17 shows the variation in droplet shape as Reynolds number is varied by an order of magnitude less than the standard case. At $t = 0.3$, the most noticeable effect is the reduction in Y by over 50 percent compared to the benchmark shape given in Fig. 6.16.

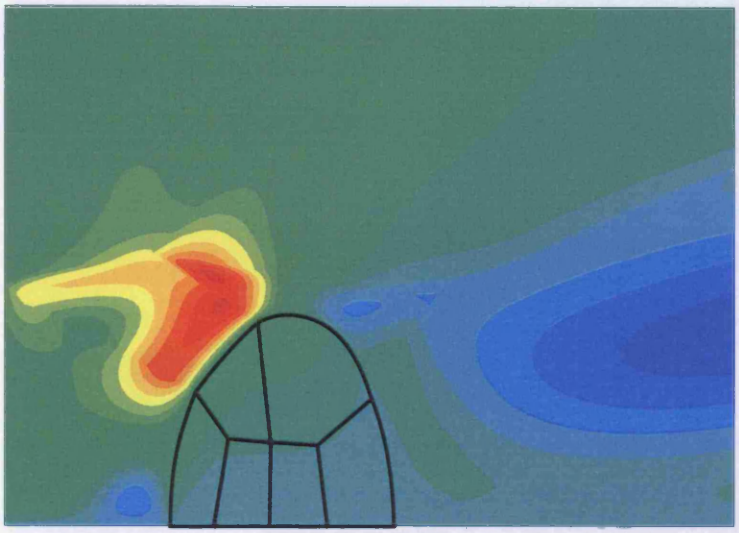

Figure 6.15: Deformed droplet with $We = 3$ at $t = 0.3$ and the radial velocity contours.

Figure 6.16: Deformed droplet with $We = 15$ at $t = 0.3$ and the radial velocity contours.

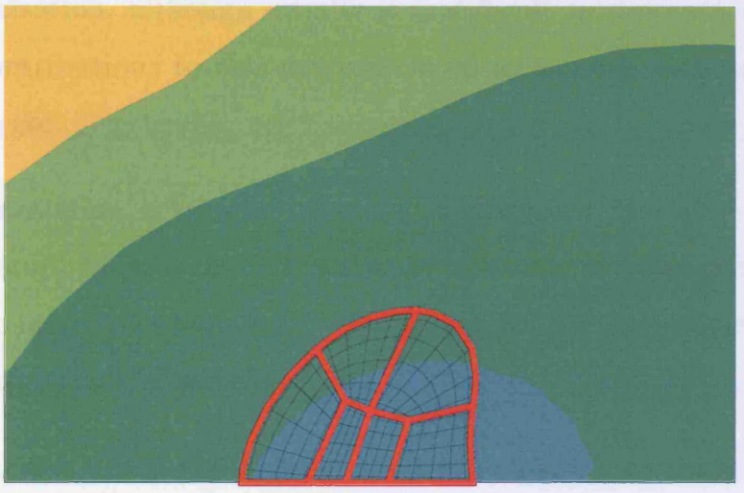

Figure 6.17: Deformed droplet with $Re = 100$ at $t = 0.3$ and the axial velocity contours.

6.2.4 Variation in Density Ratio

Increasing the density ratio between the two fluids may be related to the practical problem of atomisation under elevated ambient conditions, as associated with combustion chamber conditions in automotive IC engines or gas turbine engines, for example. In previous experimental studies, an increase in ambient density, represented here as decrease in density ratio, results in poorer atomisation, although usually it is difficult to decouple the various potential contributions to this decrease in spray quality, such as enhanced coalescence, etc.

Droplet deformation is usually viewed as a precursor indicator of primary droplet breakup. Figs. 6.18 - 6.21 show the dramatic effect of decreasing the density ratio on droplet boundary deformation, for the drop shape calculated using the benchmark $\bar{\rho}$, see Fig. 6.16.

In the numerical tests the density ratio is increased systematically from $\bar{\rho} = 100$ to the benchmark case of $\bar{\rho} = 500$, whilst all other dimensionless groups remain constant. Practically, for example, this relative change in density ratio is similar to that associated with the increase of the ambient density at time of fuel ignition within a gasoline direct injection engine under typical operation conditions. In this context, significant changes in spray diagnostics have been identified with decrease in density ratio, including a reduction in spray penetration and increase in mean droplet size (Morris, 2003), etc.

The predictions in this study provide early diagnostics of some of these global trends. Fig. 6.13 shows the significant variation in droplet deformation as the density ratio is varied systematically. At lower density ratios, the droplet deformation completely reverses compared to the benchmark case, indicated

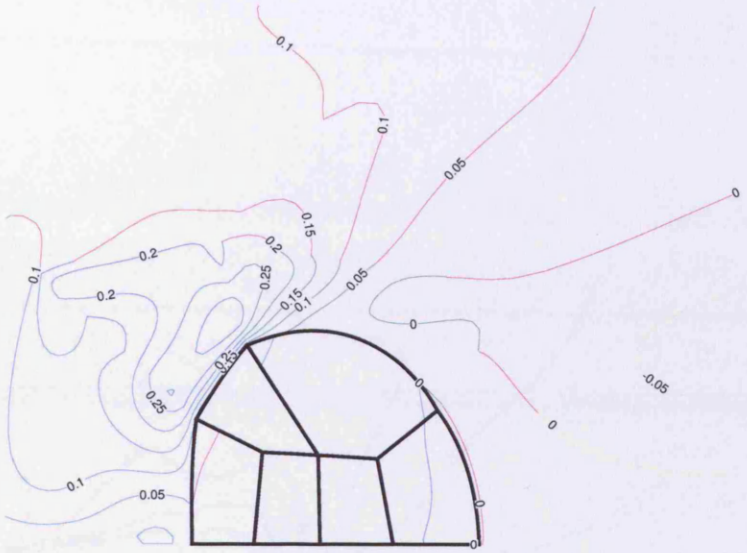

Figure 6.18: Deformed droplet with $\bar{\rho} = 100$ at $t = 0.3$ and the radial velocity contours.

by a negative k value. For the case $\bar{\rho} = 150$ (Fig. 6.19), the drop shape is almost symmetrical and ellipsoidal with no preferential direction of deformation, that means k is close to zero. For $\bar{\rho} = 400$ (Fig. 6.21), the traditional droplet deformation characteristic returns, with k taking a positive value once more.

As expected, the downstream translation reduces with the decrease in density ratio due to the increased drag, corresponding to the five-fold reduction in density ratio from 500 to 100.

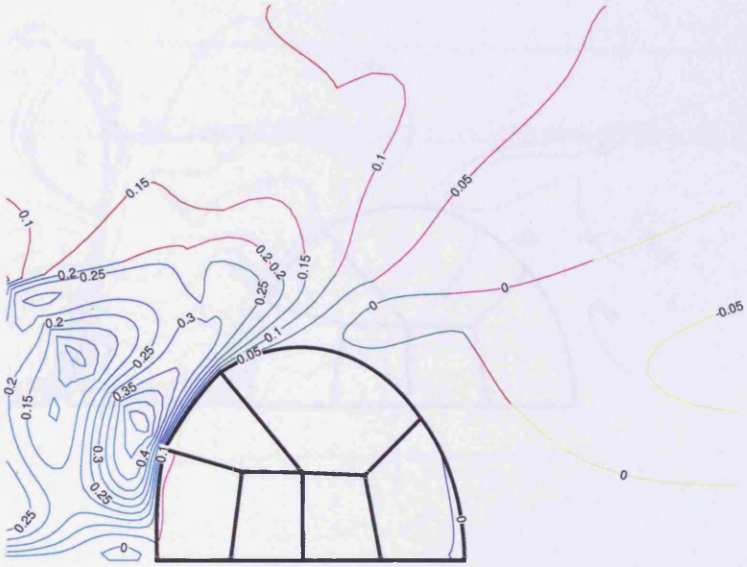

Figure 6.19: Deformed droplet with $\bar{\rho} = 150$ at $t = 0.3$ and the radial velocity contours.

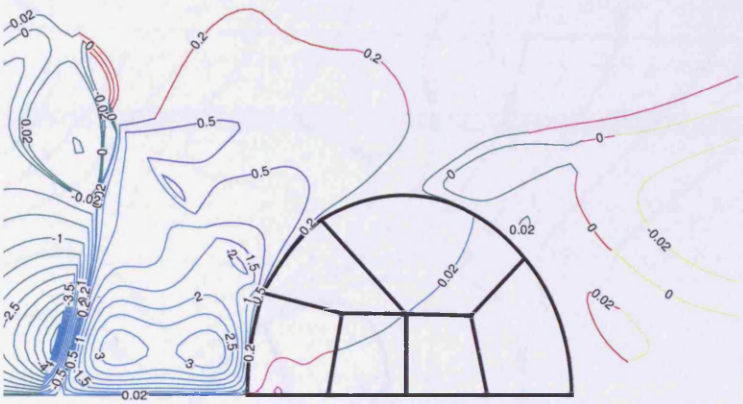

Figure 6.20: Deformed droplet with $\bar{\rho} = 250$ at $t = 0.3$ and the radial velocity contours.

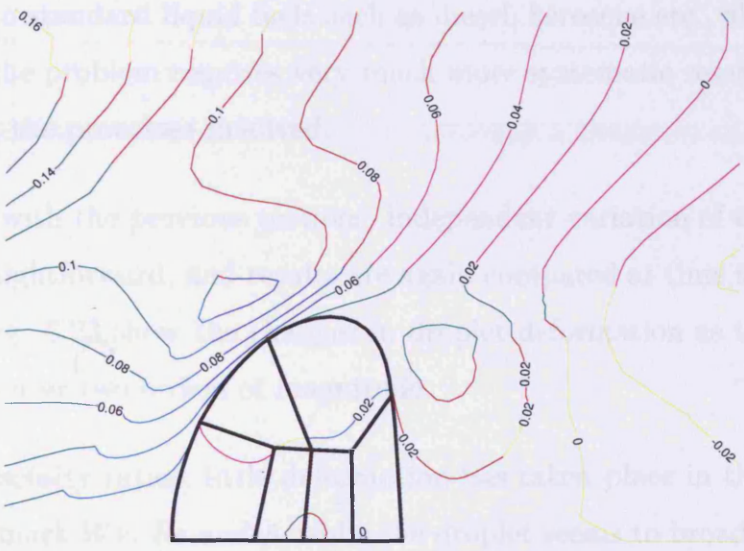

Figure 6.21: Deformed droplet with $\bar{\rho} = 400$ at $t = 0.3$ and the radial velocity contours.

6.2.4 Variation in Viscosity Ratio

Large changes in viscosity ratio have a very pertinent practical application, namely the proposed utilisation of liquid biofuel for power-generation applications (automotive, gas turbines, etc.). Biofuel has a reputation for enhanced sooting and coking, which is usually associated with inefficient atomisation. The poor atomisation is always attributed to the very high shear viscosity compared to standard liquid fuels such as diesel, kerosene etc., although it is clear that the problem requires very much more systematic research to fully understand the processes involved.

Consistent with the previous sections, independent variation of the viscosity ratio is straightforward, and results are again compared at time $t = 0.3$. Fig. 6.22 and Fig. 6.23 show the changes in droplet deformation as the viscosity ratio varies over two orders of magnitude.

For high viscosity ratios, little deformation has taken place in the condition with benchmark We, Re and $\bar{\rho}$, while the droplet seems to broadly maintain its spherical shape. This droplet is considerably further away from breakup conditions. A decrease in viscosity ratio appears to enhance deformation as expected, with increase in maximum deformation observed. Hence, these diagnostics are consistent with issues associated with efficient atomisation and combustion of pure liquid fuels.

6.3 Deformation and Kinematics of a Hexane Droplet

The deformation and kinematic characteristics of a hexane droplet in a gas flow field is considered in this section. In the simulations, the properties cor-

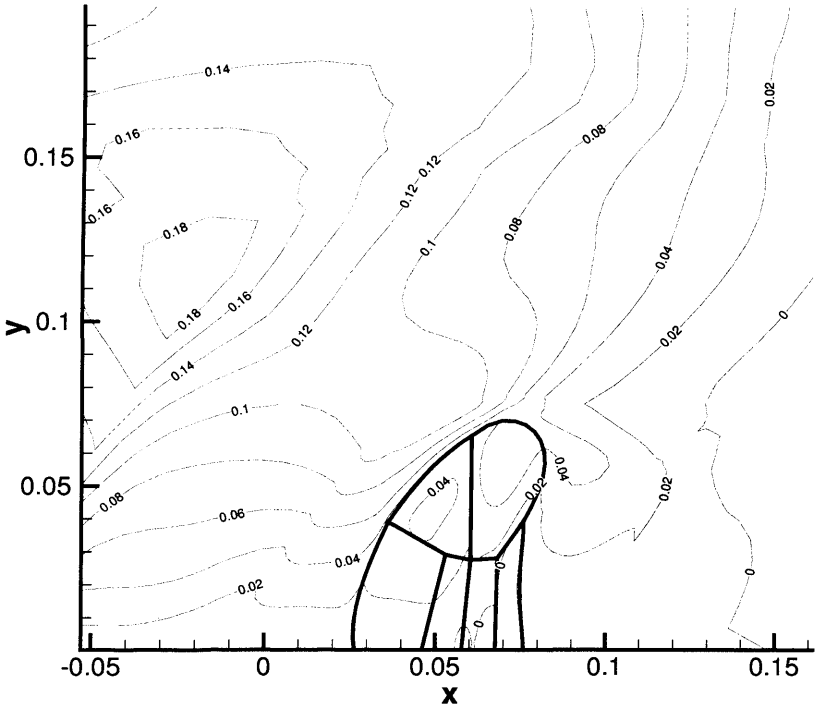

Figure 6.22: Deformed droplet with $\bar{\eta} = 0.5$ at $t = 0.3$. Note that x, y corresponding to z, r.

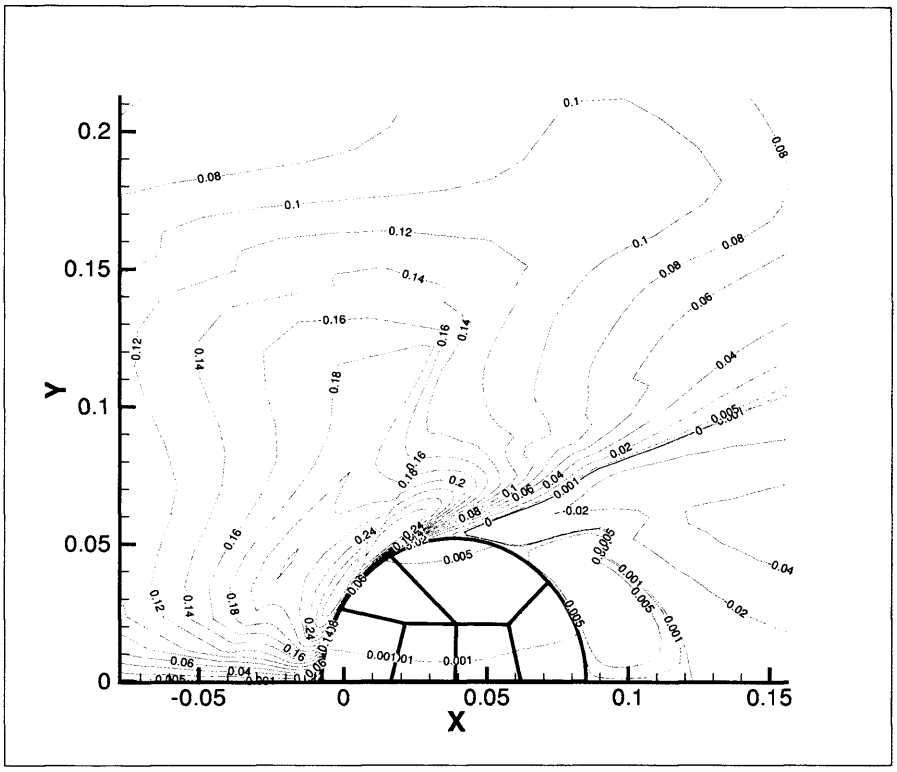

Figure 6.23: Deformed droplet with $\bar{\eta} = 160$ at $t = 0.3$, x,y corresponding to z,r.

responding to a hexane droplet in air at one atmosphere are chosen. In this case the liquid to gas density ratio is $\bar{\rho} = 564.66$ due to the densities of hexane and air at typical ambient conditions are 655 and 1.16 kg/m^3respectively. The viscosity ratio $\bar{\eta} = 2.97 \times 10^{-4}/1.85 \times 10^{-5} \approx 16.05$. The surface tension coefficient of hexane is $\sigma = 1.84 \times 10^{-2} kg/s^2$. The default values of the Reynolds and Weber numbers used in the simulations are $Re = 1000$ and $We = 15$. Although the influence of these dimensionless groups on the characteristics of the droplet deformation is investigated by considering departures from the default values, in particular the pairings $Re = 1000$ and $We = 1$ and $Re = 100$ and $We = 15$ are also considered.

It is customary in droplet deformation studies to examine the steady drag on a drop in a uniform flow. This is achieved by applying a body force to the drop at each time step. The application of the body force, of equal magnitude to the drag force, serves to ensure that the droplet remains stationary for all time. In this thesis, the physical problem is modeled by allowing the droplet to translate as well as deform in response to the external gas flow field.

The initial conditions for the problem are as follows. The droplet is assumed to be at rest initially. Then the flow field around the droplet is computed by the Stokes solver assuming that the droplet is a solid sphere. Starting with the converged solution for the Stokes problem, computations are performed over 5-10 time steps with the appropriate Reynolds number for the problem before the droplet is released. At this moment the flow field is close to the Navier-Stokes flow over a fixed sphere of the same size as the initial droplet.

In our simulations a body force is not applied. This means that the droplet

does not remain fixed in space. Instead it is allowed to accelerate until it reaches the free-stream velocity. Note that as time progresses, the relative velocity between the droplet and the external gas field decreases as the droplet decelerates, thus effectively decreasing the Reynolds number. Therefore, the droplet may not deform to the extent shown in the figures in practice. In this way of simulation, the flow field around the deformed droplet may have some obvious change due to the relative velocity being smaller in practice.

Firstly, the deformation of the droplet is investigated for the default values of the Reynolds and Weber numbers ($Re = 1000$, $We = 15$). We note that the droplet initially accelerates with the flow due to the drag force. As the droplet translates it also starts to deform relatively smoothly, reducing its axial extent or 'waist' whilst extending in the vertical direction, which is normal to the external gas flow. As time proceeds the rear of the droplet becomes flattened (see Fig. 6.24). At a later time the onset of a parachute-type breakup is observed as the droplet forms a shroud extending along the direction of the external gas flow (see Fig. 6.25). The maximum tangential velocity on the interface is 34% of the free stream velocity. At this Weber number the droplet can no longer be considered as a solid sphere and surface tension effects are important.

When the Weber number is decreased to $We = 1$ while maintaining a Reynolds number of $Re = 1000$ the extent of the deformation of the droplet normal to the external gas flow field is reduced. The droplet surface does not flatten in the downstream region as for the default set of parameters. In fact the droplet maintains an almost symmetrical shape about the vertical line passing through the centre of the droplet. The maximum tangential velocity along the interface is now 21% of the free stream velocity. This is shown in

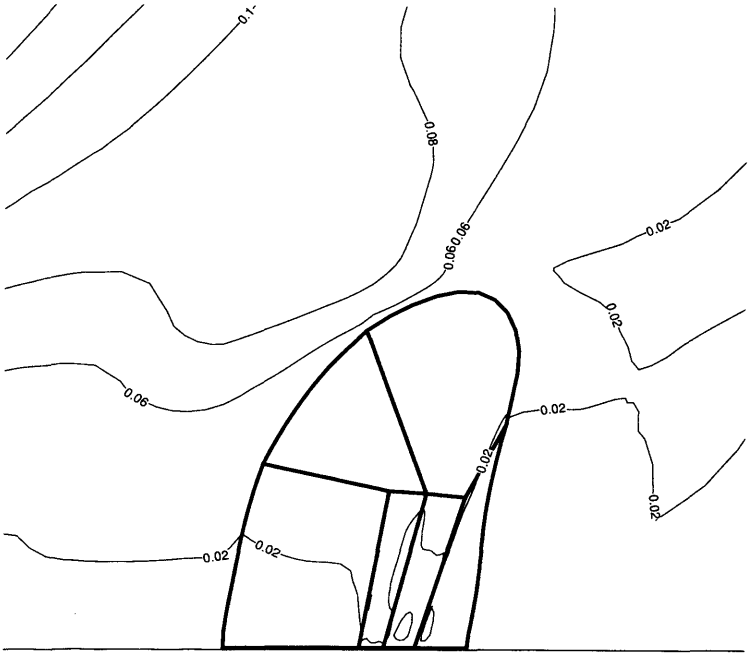

Figure 6.24: Droplet deformation and contours of the radial velocity for $Re = 1000$ and $We = 15$ at time $t = 0.35$.

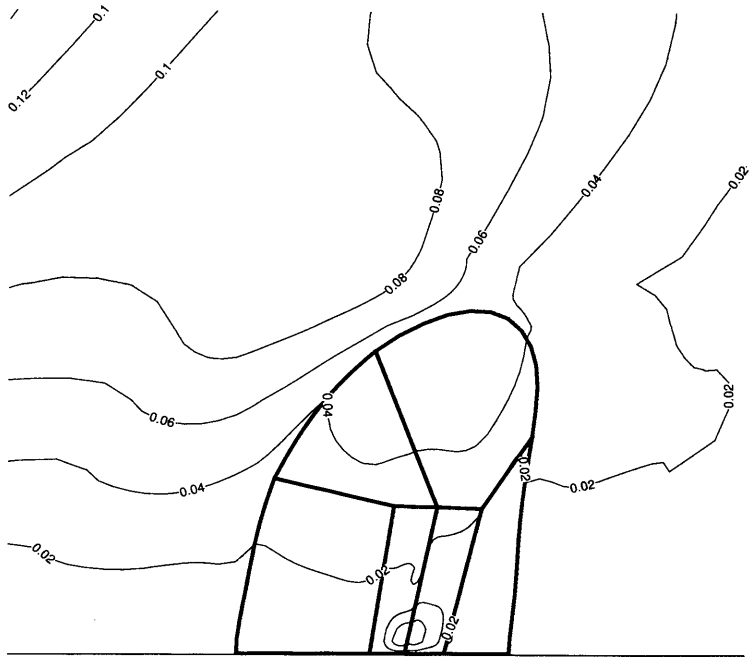

Figure 6.25: Droplet deformation and contours of the radial velocity for $Re = 1000$ and $We = 15$ at time $t = 0.3$.

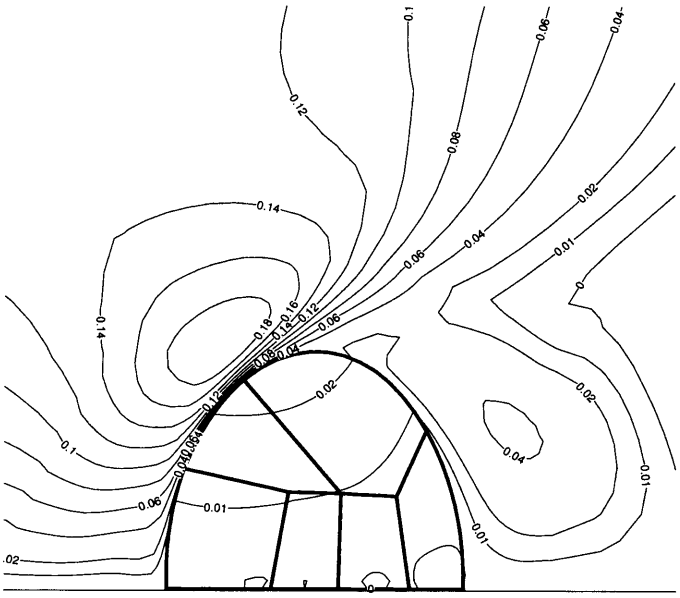

Figure 6.26: Droplet deformation and contours of the velocity magnitude for $Re = 1000$ and $We = 1$ at time $t = 0.35$.

Fig. 6.26.

When the Reynolds number is decreased to $Re = 100$ while maintaining a Weber number of $We = 15$ the deformation is quite different, which can be seen in Fig. 6.27. Although the droplet extends in the direction normal to the external gas flow field, the rear of the droplet becomes flattened.

We now explore the characteristics of the droplet deformation using the quantitative descriptors defined in Fig. 6.10. In the first set of figures the dynamics of the droplet motion are described. In Fig. 6.28 the distance, D, moved by the centre of the droplet is plotted as a function of time for the

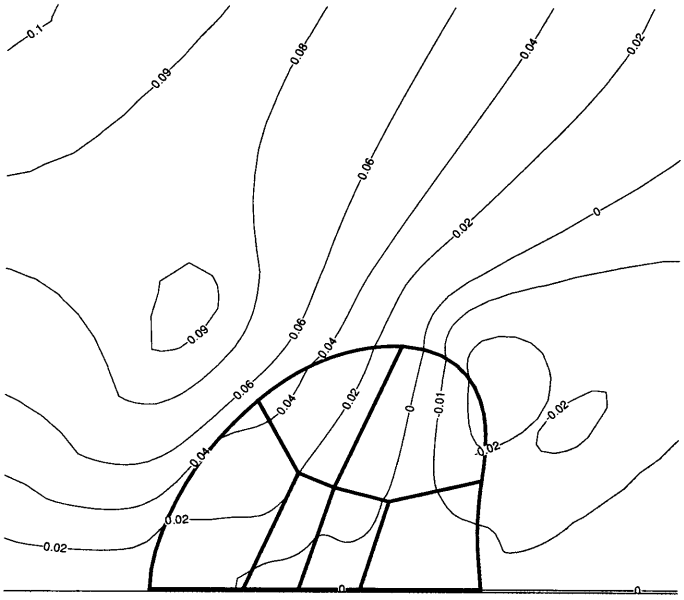

Figure 6.27: Droplet deformation and contours of the velocity magnitude for $Re = 100$ and $We = 15$ at time $t = 0.35$.

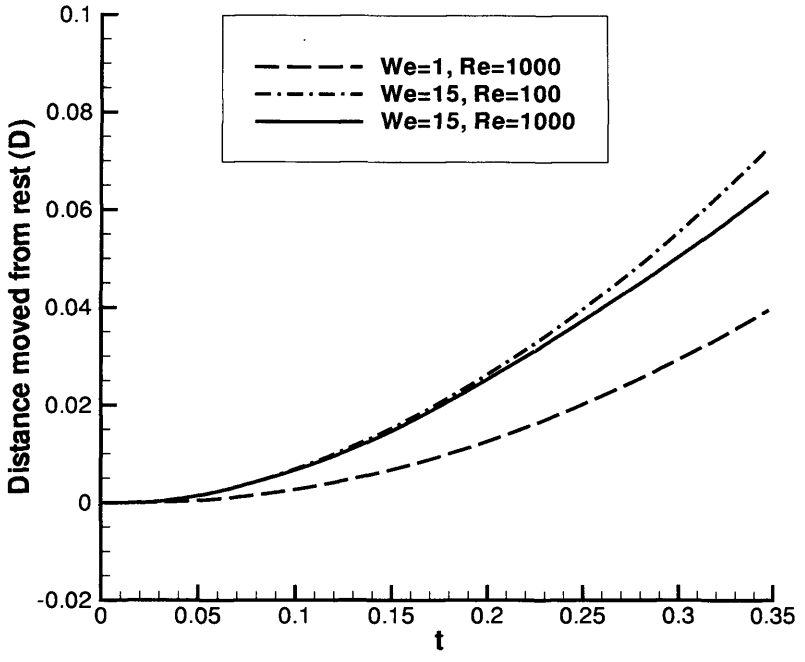

Figure 6.28: Distance travelled by the centre of the droplet from its rest position as a function of t.

three combinations of We and Re considered earlier. At the higher value of the Weber number, $We = 15$, the droplet moves considerably further downstream than for $We = 1$ during the time period considered. The droplet moves from rest and in each case the speed of the droplet increases smoothly and monotonically (see Fig. 6.29).

In the next set of figures the quantitative descriptors that provide information about the deformation of the droplet are described. In Fig. 6.30 the transient behavior of the 'waist' or axial extent of the droplet in the streamwise direction, X, is plotted as a function of time. Since the initial

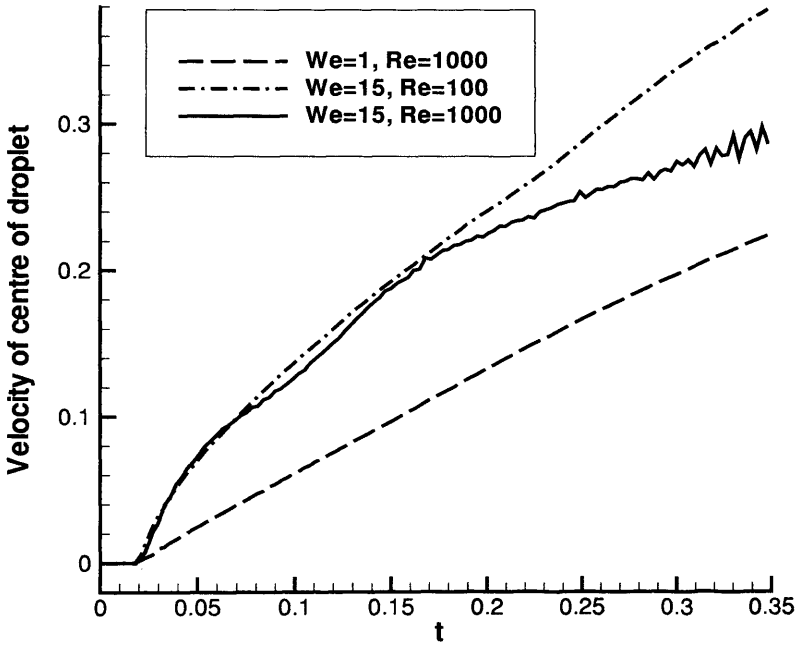

Figure 6.29: Transient behaviour of the velocity of the centre of the droplet.

diameter of the droplet is 0.1, a decrease in this value represents compression in the direction of flow. This provides one measure of the deformation of the droplet. In the case when $We = 15$ and $Re = 1000$, there is substantial deformation of the droplet in the axial direction with the diameter of the droplet diminishing by more than 50% of its initial value. This is reinforced by the information contained in Fig. 6.31 which displays information about the maximum cross-sectional radius of the droplet measured from the axis. An interesting feature in this figure is the way in which the curves corresponding to $We = 15$, $Re = 100$, and $We = 1$, $Re = 1000$, cross over. This information is combined in Fig. 6.32 in which the quantity $2Y/X$ is plotted as a function of time. This is a ratio of the maximum spanwise diameter of the droplet to its axial streamwise diameter, which measures the nature of the deformation. The departure is from its initial value, which is one. An increase in the value of $2Y/X$ corresponds to deformation normal to the flow direction while a value less than one corresponds to deformation in the flow direction. This figure shows that significant deformation normal to the flow direction is predicted for the default parameter values ($We = 15$, $Re = 1000$) with $2Y/X \to 3$ as $t \to 0.35$. The deformation is not as much as this in the other two cases.

Finally, in Fig. 6.33 we plot the horizontal distance of the maximum extent of the surface of the droplet from the axis to the centre of the droplet. A positive value corresponds to a maximum downstream shift of the droplet centre while a negative value corresponds to a maximum upstream shift of the droplet centre. This figure shows that the extremities of the deformed droplet can reverse its direction of motion relative to the 'nominal' centre of the moving, deforming droplet. For low Weber number ($We = 1$) the nominal centre of the droplet first moves away from the centre in the upstream

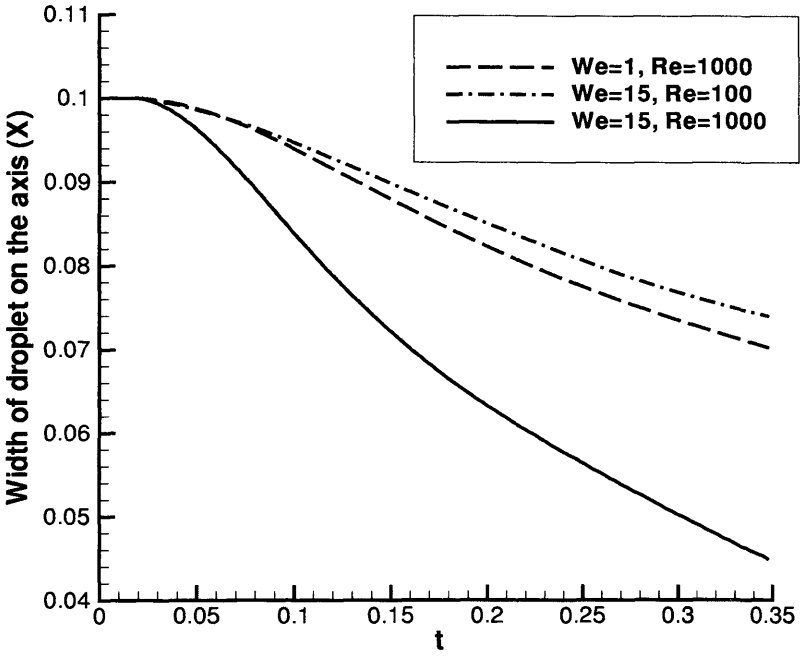

Figure 6.30: Axial extent of the droplet as a function of t. The initial diameter of the droplet is 0.1.

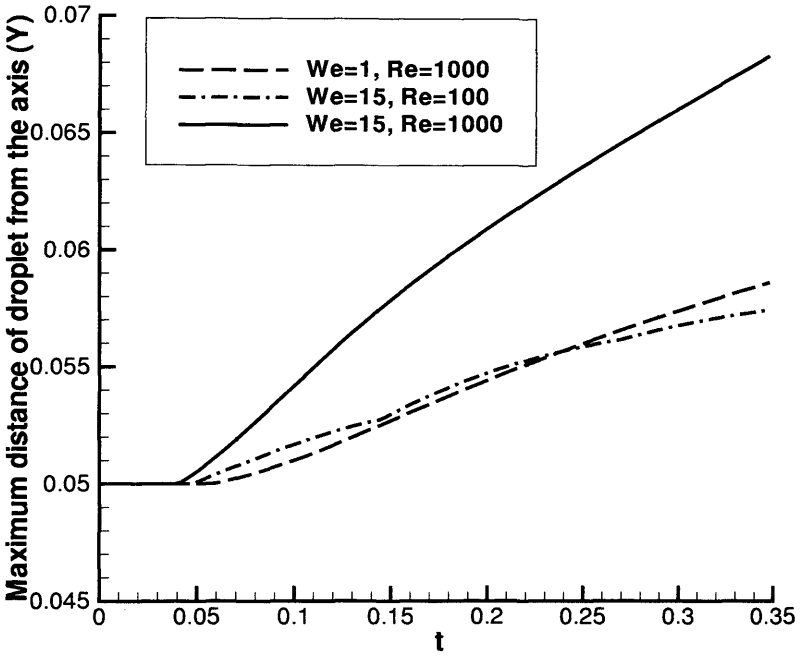

Figure 6.31: Maximum vertical extent of the droplet from the axis as a function of t.

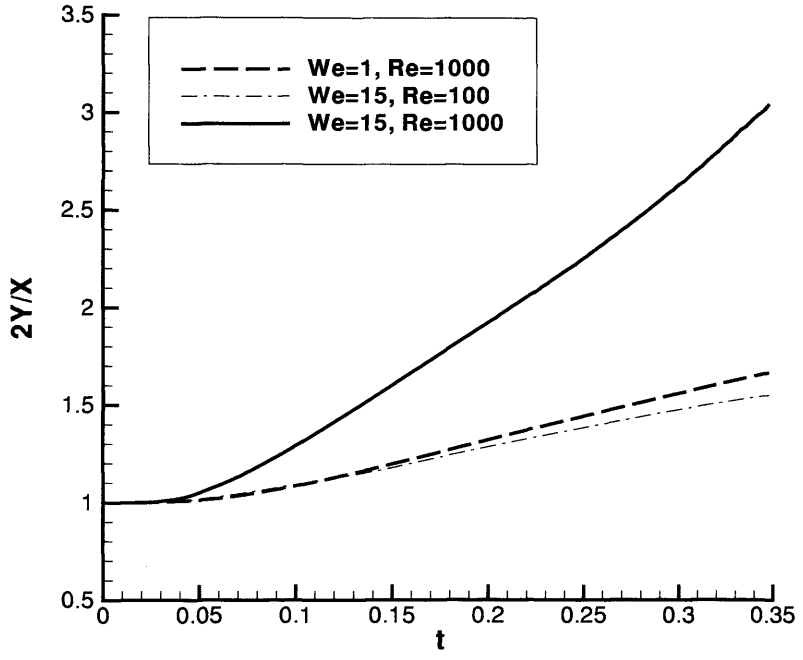

Figure 6.32: Transient behaviour of $2Y/X$.

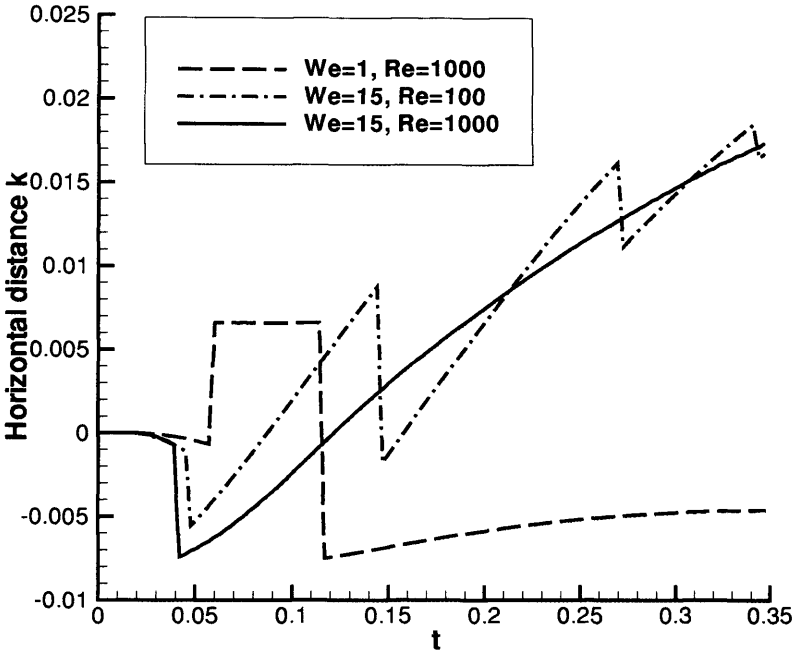

Figure 6.33: Horizontal distance of the point of maximum vertical extent from the axis to the centre of the droplet as a function of t.

direction, then moves in the downstream direction before relaxing and seemingly approaching a constant deformation in the upstream direction. This can be associated with the increased influence of surface tension for low Weber number. In contrast for higher Weber number ($We = 15$), the nominal centre of the droplet again moves initially in the upstream direction, before reversing and continuing to deform in the downstream direction with time, due to less resistance to shape change as a result of reduced surface tension forces.

For higher Weber number ($We = 15$) and lower Reynolds number ($Re =$

100), the droplet oscillates during the dominant period of oscillation in the downstream direction. This may explain the mechanism by which satellite droplets are formed from the parent droplet. The oscillations appear to dampen out for higher Reynolds number as the deformation process becomes more stable due to the influence of inertia dominates over viscous forces.

Chapter 7

Deformation of Non-Newtonian Fluid Droplet

7.1 Introduction

The fluids that have been studied in this thesis until now have been Newtonian fluids, for which the stress tensor in the Navier-Stokes equations can be expressed as a linear, isotropic function of the velocity gradient (Owens and Phillips, 2002). Nevertheless, in our daily lives, many fluids are non-Newtonian, for instance, blood, egg white, and in artificial products such as ketchup, toothpaste, solvent, polymer solution, and so on. Therefore, the extension of the droplet/flow model, developed in the previous chapters, to include non-Newtonian effects is of particular interest, giving the range of practical problems involving fluids that exhibit non-Newtonian characteristics, and the potential influence of non-Newtonian parameters in droplet deformation, which, in fact, have only been given very limited consideration hitherto.

A numerical prediction for the deformation of a blood droplet in air flows is conducted in this chapter, which may be applied to the evidence analysis in criminality because of the interdependence among the blood drop shape, the speed of its movement, as well as the moving direction. The inclusion of non-Newtonian effects is known generally to increase the difficulty of obtaining converged numerical solutions, and so a gradual increase in model complexity is proposed. At this primary stage of development, neither the elasticity of the fluid nor the differential constitutive equations in the mathematical modelling is considered. In the context of this chapter, the constitutive modelling for the viscosity of blood droplet is given in section 7.2, and the incorporation of the viscosity modelling into the spectral element formulation is discussed in section 7.3, finally the numerical simulation results are presented in section 7.4.

7.2 Non-Newtonian Model

The key difference in fluid properties between Newtonian and non-Newtonian fluids is that the viscosity of non-Newtonian fluids is no longer a constant and the stress tensor in the Navier-Stokes equations becomes a nonlinear function of the velocity gradient. Methods recently developed to compute the stress tensor is to integrate the tensor rate, which take stresses as dependent variables and construct extra constitutive equations, such as upper-convected Maxwell model and Oldroyd B model (Owens and Phillips, 2002), to be solved together with the mass and momentum conservation equations. However, this may be expensive to implement with standard computing facilities for the problem of droplet deformation and makes the cost rise due to complex geometry as well as the added complication caused by the moving mesh.

Furthermore, the convergence of the numerical solutions using the PCG iterative method discussed earlier is unpredictable because little previous work has been done for this problem. Hence, simpler and more straightforward models for the viscosity ought to be considered first.

Whilst the simplest non-Newonian viscosity comprise two-parameters, e.g. the power law model, or three-parameters, e.g. Herschel-Buckley model (Sankar and Hemalatha 2005), here the four-parameter Cross viscosity model (Cross and Colloid 1965) is utilised in the interest of generality. These are examples of so-called shear-rate dependent viscosity model without the consideration for particular non-Newtonian materials. The common two and three parameter models referenced are in fact special cases of the Cross model. The Cross model has been utilised previously to describe a broad range of non-Newtonian fluids, including polymer solutions and melts, particulate suspensions, yoghurt, soy protein suspensions, hair shampoo, and blood.

The Cross law as a function of shear-rate is given in the following mathematical form:

$$\frac{\eta(\dot{\gamma}) - \eta_\infty}{\eta_0 - \eta_\infty} = \frac{1}{(1 + K\dot{\gamma})^m} , \tag{7.1}$$

or

$$\eta(\dot{\gamma}) = \eta_\infty + \frac{\eta_0 - \eta_\infty}{(1 + K\dot{\gamma})^m} , \tag{7.2}$$

where $\dot{\gamma}$ is the generalised shear-rate defined by

$$\dot{\gamma} = \sqrt{2\left(\frac{\partial u}{\partial z}\right)^2 + 2\left(\frac{\partial v}{\partial r}\right)^2 + \left(\frac{\partial u}{\partial z} + \frac{\partial v}{\partial r}\right)^2} . \tag{7.3}$$

In the above equations, the four parameters are η_0: the zero shear-rate viscosity, η_∞: the high shear-rate viscosity asymptote, K and m: coefficients

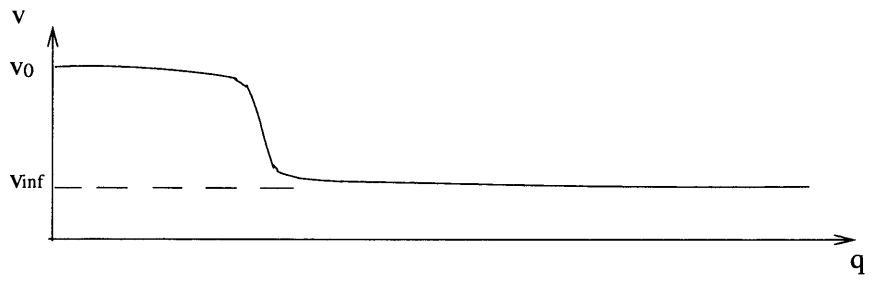

Figure 7.1: η_∞ vs $\dot{\gamma}$.

that vary as fluid changes, where K has dimension of time and m is dimensionless.

Figure 7.1 shows the variation of viscosity as the shear-rate increases from zero to infinity according to the Cross model, where v, q represent η and $\dot{\gamma}$ respectively.

7.3 Formulation and Approximation of the Problem

The problem of flow with a non-Newtonian droplet is still governed by the equations (5.30), (5.36) and (5.37). The only difference in the mathematical formulation is that the dimensionless viscosity ratio in the expression of viscous stresses for the liquid phase:

$$\mathbf{T}_d = 2\bar{\eta}\mathbf{d}_d$$

is no longer a constant, which, by considering the Cross model, may be written as:

$$\bar{\eta} = \frac{\eta_d}{\eta_g} = \frac{\eta_\infty}{\eta_g} + \frac{\eta_0 - \eta_\infty}{(1 + K\dot{\gamma})^m \eta_g}, \tag{7.4}$$

where note that both η_0 and η_∞ correspond to properties of the liquid phase. Corresponding to this, the diffusion term $E\mathbf{u}$ in the discretized momentum equation (5.11) needs to be replaced by

$$E_d\mathbf{u} = \begin{pmatrix} E_z^d & 0 \\ 0 & E_r^d + E_v^d \end{pmatrix} \begin{pmatrix} \mathbf{u}_z \\ \mathbf{u}_r \end{pmatrix} , \tag{7.5}$$

where E_d represents the diffusive matrix for the droplet phase, and E_z^d etc. are its sub-matrices.

Similar to that $E\mathbf{u}$ is the summation of a number of integrations, each of which is represented by a matrix such as E_ξ times a variable vector, as shown in equations (3.64)-(3.70), E_d consist of similar matrices. For instance, E_z^d and E_r^d may be expressed as

$$E_z^d = E_r^d = E_\xi^d + E_\eta^d + E_{\xi\eta}^d + E_{\eta\xi}^d , \tag{7.6}$$

where, for example, E_ξ^d is obtained by incorporating the viscosity ratio into E_ξ in equation (3.65). The element of $E_\xi^d \vec{u}$ may be written as

$$e_{kl,ij}^{\xi} = \sum_{p=0}^{N} \sum_{q=0}^{N} u_{ij} h_i'(\xi_p) h_j(\eta_q) h_k'(\xi_p) h_l(\eta_q) w_p w_q \frac{|J_{pq}|}{Re} G_1^{pq} \bar{\eta}_{pq} , \tag{7.7}$$

where $\bar{\eta}_{pq}$ is a function of position and considered as already known since it is calculated using information from the previous time step. Equation (7.4) is used to calculate $\bar{\eta}_{pq}$, in which

$$\dot{\gamma}_{pq} = \left\{ 2 \left(\frac{\partial u^n}{\partial z} \right)_{pq}^2 + 2 \left(\frac{\partial v^n}{\partial r} \right)_{pq}^2 + \left[\left(\frac{\partial u^n}{\partial z} \right)_{pq} + \left(\frac{\partial v^n}{\partial r} \right)_{pq} \right]^2 \right\}^{0.5} , \tag{7.8}$$

where

$$\left(\frac{\partial u^n}{\partial z} \right)_{pq} = \left(\frac{\partial u^n}{\partial \xi} \frac{\partial r}{\partial \eta} - \frac{\partial u^n}{\partial \eta} \frac{\partial r}{\partial \xi} \right)_{pq} \frac{1}{J_{pq}}$$

$$= \frac{1}{J_{pq}}\left(\frac{\partial r}{\partial \eta}\right)_{pq} \sum_{m=0}^{N}\sum_{n=0}^{N} u_{mn}^{n} h_{m}^{'}(\xi_p) h_n(\eta_q)$$

$$- \frac{1}{J_{pq}}\left(\frac{\partial r}{\partial \xi}\right)_{pq} \sum_{m=0}^{N}\sum_{n=0}^{N} u_{mn}^{n} h_{m}(\xi_p) h_{n}^{'}(\eta_q) \qquad (7.9)$$

and

$$\left(\frac{\partial v^n}{\partial r}\right)_{pq} = \left(\frac{\partial v^n}{\partial \eta}\frac{\partial z}{\partial \xi} - \frac{\partial v^n}{\partial \xi}\frac{\partial z}{\partial \eta}\right)_{pq} \frac{1}{\mathbf{J}_{pq}}$$

$$= \frac{1}{J_{pq}}\left(\frac{\partial z}{\partial \xi}\right)_{pq} \sum_{m=0}^{N}\sum_{n=0}^{N} v_{mn}^{n} h_{m}(\xi_p) h_{n}^{'}(\eta_q)$$

$$- \frac{1}{J_{pq}}\left(\frac{\partial z}{\partial \eta}\right)_{pq} \sum_{m=0}^{N}\sum_{n=0}^{N} v_{mn}^{n} h_{m}^{'}(\xi_p) h_{n}(\eta_q) \qquad (7.10)$$

Other matrices in equation (7.6), as well as E_v^d, can be constructed in the same way.

7.4 Numerical Prediction of Blood Droplet Deformation

In terms of pratical relevance, the Cross model fluid parameters have been chosen to represent a nominal sample of blood (Barnes, Hutton and Walters 1989), though it is appreciated that blood requires more sophisticated visco-elastic modelling for more realistic prodictions in complex flows (Owens 2006).

The benchmark conditions such as $Re = 1000$, $We = 15$, air density and viscosity, are considered again, but with the four additional parameters required for the Cross model taken from Barnes, Hutton and Walter (1989) for blood to be $\eta_0 = 125mP.s$, $\eta_\infty = 5mP.s$, $K = 52.5s$, and $m = 0.715$. The degree of shear-thinning is represented by the value of m, where m approching

zero tends towards the Newtonian fluid, whilst m approaching 1 indicates the most shear-thinning fluids. Hence, in this model blood is considered to exhibit shear-thinning characterisics. Atomisation of blood has been known to be influential in homicide legal cases, where differences in blood spray at the scene require differentiating in terms of the atomisation source, e.g. spray due to impact, involuntary oral spray release due to releasing blood collecting in bodily air passages.

Significant variation in deformation topology from the Newtonian cases is visible in Fig. 7.2, as the droplet now extends laterally, in the direction of flow, rather than orthogonal to the flow, and the peak of the drop moves away from the droplet 'centre' towards the coming flow. From the observation of the simulation development we also noticed that the droplet starts to deform much later than that in the Newtonian cases and deforming more slowly, it reaches the shape shown in Fig. 7.2 by the time $t = 0.6$. It seems that the fragmentation might happen when the drop elongates further in the axial direction with a flow which has a higher Reynolds number.

Fig. 7.3 shows the same droplet deformation with the contours of radial velocity magnitude and streamlines, from which it can be seen that the range of wake disturbance is larger than that in the Newtonian cases.

The findings in the blood drop deformation show significantly different topologies and require considerable further investigation in the future. The results presented here are part of a preliminary study.

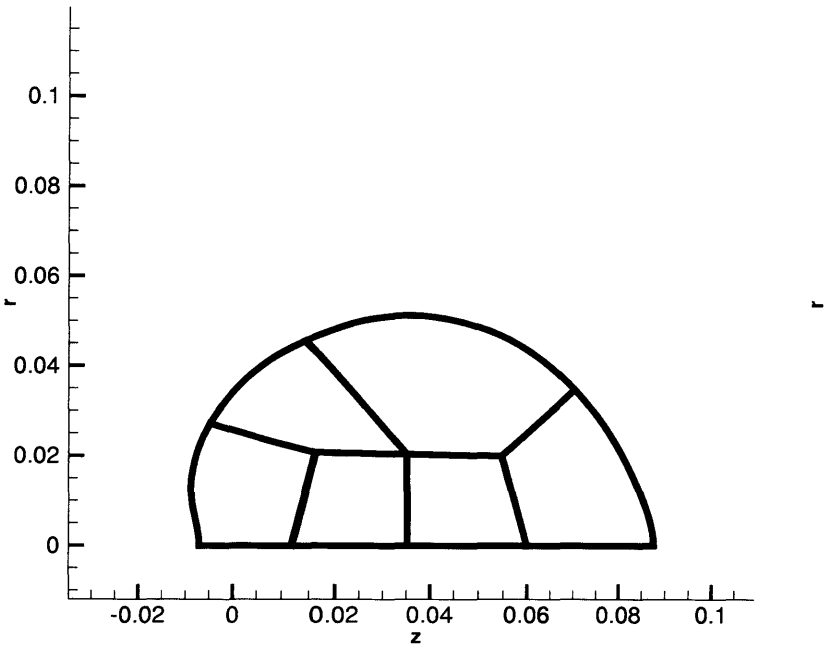

Figure 7.2: Deformation of a blood droplet represented by the shear-thinning model of Cross.

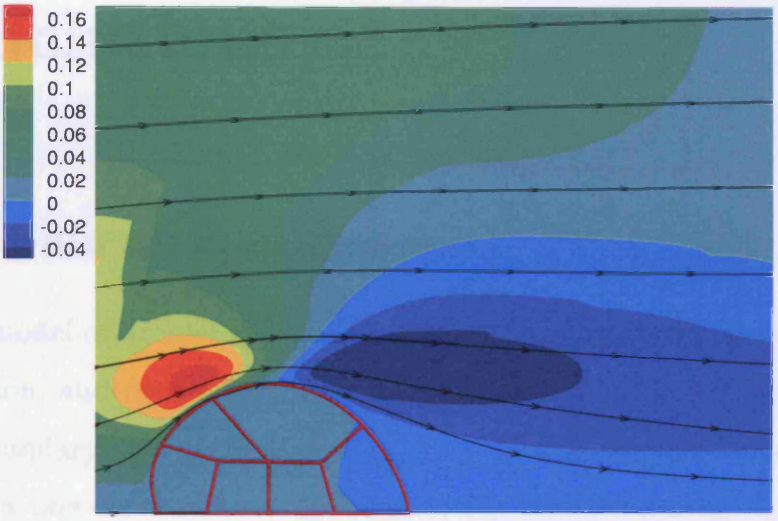

Figure 7.3: Deformed blood droplet with the contours of v-component velocity and sreamlines.

Chapter 8

Conclusions

8.1 Salient Features

A new model of droplet deformation based on a spectral element spatial discretization, and coupled with an ALE algorithm to track the freely moving drop boundary, has facilitated the study of a single Newtonian droplet, as well as a non-Newtonian drop, translating and deforming in a Newtonian medium. In the spectral element method used in the study, Lagrange nodal expansions constructed with the Legendre polynomials, and collocated on the Legendre-Gause-Lobatto points, enables the droplet to be tracked accurately and efficiently.

In the numerical model, the surface tension on the interface between the droplet and the surrounding gas is treated implicitly and naturally within the weak formulation of the problem. The mesh movement, to trace the drop shape that varies in time, is also incorporated into the weak formulation of the governing equations. In addition to the movement of the mesh, the computation associated with each time step comprises an explicit treatment of the convection term and an implicit treatment of the linear terms.

All of these have made the model work successfully.

The two-fluid equations which govern the problem have been neatly nondimensionalised to express the problem in terms of four dimensionless variables, each of practical relevance. Hence, it has been possible to undertake numerical studies for each of the variables independently.

Apart from the fact that all the simulations show excellent converge properties with the PCG iterative scheme, the numerical model has been successfully coded and tested step by step with the benchmark case of steady Stokes and Navier-Stokes channel flows and ambient flows over a solid sphere. The ALE technique, as well as the skills of blending linear and higher order mappings to conform the arbitrary interfacial geometry between the two fluids, is validated by comparison with previous work.

8.2 Concluding Remarks

The numerical predictions of the new spectral element model for multiphase flow problems have provided a unique insight into the precursory two-fluid interaction processes which give rise to liquid droplet deformation, and ultimately breakup. The model has been utilised to show significant differences in deformation processes for fluid models of practical liquids such as hydrocarbons (e.g. hexane) as well as differences occurring due to practical operating conditions. These liquid droplets deform in significantly different ways, giving rise to interface shapes which contrast considerably from the commonly accepted models such as bag-breakup.

The non-dimensionalisation of the underlying governing two-fluid equations facilitates decoupling of the four governing groups (We, Re, $\bar{\rho}$, $\bar{\eta}$), which has

allowed parametric numerical experiments to be undertaken to explore the relative influence of these groupings. Hence, the physical bases for 'black-box' empirical relationships (e.g. Weber number condition) currently found in the literature can be explored, and traced back to fundamental fluid mechanics causes. Moreover, the unique feature of having modelled a droplet deforming whilst in translation has allowed transient features of the different processes to be ascertained for the first time. In terms of practical problems, these detailed numerical investigations allow insights into the root causes of some very important contemporary two-phase power generation problems e.g. reduced atomisation quality for liquid biofuel, giving rise to increased emissions and 'coking' in engines; the significant variations in atomisation quality for direct fuel injection into 'elevated' engine environments; droplet breakup in water-based explosion suppression systems.

The techniques utilised for this two-phase free-boundary problem demonstrate the effectiveness of the spectral element DNS approach. High-order spectral discretizations have been used to predict complex two-phase flow behaviour for the first time. The weak formulation of an ALE description of the problem has been carefully constructed using test functions that are independent of time and incorporating the force balance across the interface between the phases implicitly.

The development of this multiphase spectral element method should lead to improved predictive capability for industrial sprays, with benefits primarily in terms of improved fuel economy and reduced environmental emissions. Similarly, better understanding of water-based explosion mitigation systems will lead in the longer term to improved understanding of mitigation mechanisms, with the consequence of improved health and safety practice.

8.3 Suggestions for Future Work

The models developed within this study naturally lend themselves to multiple droplet phenomena, which also contribute to liquid-fuel power-generation problems. The methodology described here will be modified and extended to allow for an investigation of multiple droplet problems. Typical processes include: coalescence, for which there are a number of databases available, which show spatial variations in droplet size distributions that cannot be predicted with contemporary modelling approaches; impingement, which occurs as droplets within sprays impact upon solid surfaces or liquid films, as applied in direct injection gasoline engines, or hazardous liquid releases. As was the case for droplet breakup studies, contemporary empirical modelling approaches are immature, and would benefit by complementary fundamental analysis and interpretation, as offered by the spectral element approach described in this paper.

Other viscosity models such as power law etc. and various non-Newtonian droplet scenarios should also be calculated. Different tendencies of non-Newtonian drop deformation and the causes of breakup may be explored by the numerical simulations. This may give new ideas to the sub-grid modelling for the secondary atomisation.

The techniques of mesh adaptation and optimization (Frey and George 2000) may be introduced into the ALE scheme to handle the more complex geometry of the droplet boundary, allowing for the drop to deform further towards breakup. Since the operation of remeshing is independent of the main stream of the calculation, any complication from it may not cause an obvious rise in cost. However, an interpolation of the variables (after a time step) from the moved mesh (from the previous time step) to the mesh modified through

adaptation or optimization, is needed for this case.

As the environment of atomisation flows are predominantly transitional or turbulent, 3-dimensional numerical models are needed to simulate these flows as long as computer hardware is powerful enough. In the case of extending the two and half dimensional models developed in this study to 3D to calculate turbulent flows, Large Eddy Simulation (LES) is considered the most suitable technique for the problem of droplet deformation. This is because it smears the small eddies and retains the large eddies. It is the large eddies that cause the drop to deform. LES techniques have worked well with the spectral element method for some simulations of air flows (see Karniadakis and Sherwin 1999) and the modified PCG method may be applied to non-axisymmetric 3D problems. Note that turbulence models are only needed for the gas phase, whilst the flow within the droplet is conventionally considered as laminar.

Bibliography

[1] Achenbach, E. *Vortex shedding from spheres*, J. Fluid Mech., Vol. 62, pp 209-221, 1974.

[2] Aggarwal, S.K. and Sirignano, W.A. *Unsteady spray flame propagation in a closed volume*, Combustion and Flame, Vol. 62, pp 69-84, 1985.

[3] Ali, A.N.H. *Characterisation of droplet break-up processes for explosion mitigaton by water sprays*, MSc. Thesis, University of Wales, Cardiff, 1995.

[4] Ashgriz, N. and Poo, J.Y. *FLAIR: Flux line-segment model for convection and interface reconstruction*, J. Comp. Phys., Vol. 93, pp449-468, 1991.

[5] Babuska, I. and Suri, M. *The p and h-p versions of finite element method, basic principles and properties*, SIAM REview, Vol. 36, No. 4, 1994.

[6] Barnes, H.A., Hutton, J.F. and Walters, K. *An Introduction to Rheology*, Elsevier, Amsterdam, 1989.

[7] Behr, M. and Tezduyar, T.E. *Finite element solution strategies for large-scale flow simulation*, Comput. Meth. Appl. Mech. Engrg., Vol. 112, pp 3-24, 1994.

[8] Belytschko, T., Kennedy, J.M. and Schoeberie, D.F. *Quasi-Eulerian finite element formulation for fluid structure interactions*, ASME, J. Pressure Vessel Technol., Vol. 102, pp 62-69, 1980.

[9] Berthoumieu, P., Carentz, H., Villedieu, P. and Lavergne, G. *Contributions to droplet breakup analysis*, J. Heat and Fluid Flow, Vol. 20, pp 492-498, 1999.

[10] Bowen, P.J. *A study of swirling flow using spectral methods*, PhD Thesis, University of Wales, Aberystwyth, 1990.

[11] Bowen, P.J., Bull, D.C., Prothero, A. and Rowson, J.J. *Deflagration of hydrocarbon aerosol fuels*, Combust. Sci. and Tech., Vol. 130, pp 25-47, 1997.

[12] Bowen, P.J., Phillips, T.N. and Zheng, Y. *Direct numerical simulation of non-Newtonian droplet deformation*, Paper A3-09-185, 10th International Conference on Liquid Atomisation and Spray Systems (ICLASS 2006), Kyoto, Japan, ISBN 4-9902774-1-4, Sept. 2006.

[13] Bowen, P.J., Phillips, T.N. and Zheng, Y. *The prediction of droplet deformation using a spectral ALE method*, submitted to J. Comp. Phys., 2006.

[14] Bowen, P.J. and Cameron, L.J. *Hydrocarbon aerosol explosions: a review*, Trans. IChemE, Vol. 77, part B, pp 22-30, 1999.

[15] Bowen, P.J. and Shirvill, L.C. *Combustion hazards posed by the pressurised atomisation of high-flashpoint liquids*, Jnl. Loss Prevention Process Ind, Vol. 7, No. 3, pp 233-241, 1994.

[16] Brackbill, J.U., Kothe, D.B. and Zemack, C. *A continuum method for modelling surface tension*, J. Comp. Phys., Vol. 100, pp 335-354, 1992.

[17] Canuto, M.Y., Hussaini, A.Q. and Zang, T. *Spectral methods in fluid dynamics*, Springer-Verlag, 1987.

[18] Catlin, C.A., Gregory, C.A.J., Johnson, D.M. and Walter, D.G. *Explosion mitigation in offshore modules by general area deluge*, Trans. IChemE, Vol. 71, part B, May 1993.

[19] Chan, R.K.C. and Street, R.I. *A computer study of finite amplitude water waves*, J. Comp. Phys., Vol. 62, pp 4579-4585, 1970.

[20] Chandler, R.E. *A spetral method for estimatiing parameters in rainfall models*, Bernoulli Journal of Mathematical Statistics and Probability, Vol. 3, No. 3, pp 301-322, 1997.

[21] Chen, M.M. *Thermocapillary convection in materials processing*, Interdisciplinary Issues in Materials Processing and Manufacturing, Vol. 2, pp 541-558, ASME, New York, 1987.

[22] Constantinescu, G. and Squires, K. *Numerical investigations of flow over a sphere in subcritical and supercritical flows*, Physics of Fluids, Vol. 16, No. 5, 2004.

[23] Comer, M.A. *Transient G-DI fuel spray characterisation*, PhD Thesis, Cardiff University, 1999.

[24] Comer, M.A., Bowen, P.J., Bates, C.J., Sapsford, S.M. and Johns, R.J.R. *Transient 3D analysis of a DI gasoline engine injector spray*, Atomisation and Spray, Vol. 9(5), pp 467-482, 1999.

[25] Comer, M.A., Bowen, P.J., Sapsford, S.M. and Kwon, S.J. *A parametric sensitivity study of gdi spray charasteristics using a 3D transient model*, Int. J. Automotive Technology, 2005.

[26] Continillo, G. and Sirignino, W.A. *Numerical study of multi-component fuel spray flame propagation in a spherical closed volume*, Proceedings of the 22th Symposium on combustion, pp 1941-1949, 1991.

[27] Daly, B.J. *A technique for including surface tension in hydrodynamic calculations*, J. Comp. Phys., Vol. 4, pp 97-117, 1969.

[28] Dandy, D.S. and Leal, L.G. *Buoyancy-driven motion of a deformable drop through a quiescent liquid at intermediate Reynolds numbers*, J. Fluid Mech., Vol. 208, pp161-192, 1989.

[29] Deng, Z.T. and Demg S.M. *Numerical simulation of droplet deformation in convection flows*, AIAA Journal, Vol. 30, pp 1290-1297, 1992.

[30] Donea, J., Giuliani, S. and Halleux, J.P. *An arbitrary Lagrangian-Eulerian finite element method for transient dynamic fluid-structure interactions*, Comput. Mech. Appl. Mech. Engrg., Vol. 33, pp 689-723, 1982.

[31] Drew, D. and Lahey, R.T. *Mathemetical modelling in two-phase flow*, Ann. Rev. Fluid Mech., Vol. 15, 1983, pp 261-291

[32] Faeth, G.M. *Spray Combustion Phenomena*, Proceeding of the 26th Symposium (International) on Combustion, pp 1593-1613, Naples, 1996.

[33] Feigl, K., Kaufmann, S.F.M., Fischer, P. and Winfhab E.J. *A numerical procedure for calculating droplet deformation dispersing flows and ex-*

perimental verification, Chemical Engineering Science, Vol. 58, pp 2351-2363, 2003.

[34] Ferziger, J.H. and Peric, M. *Computational methods for fluid dynamics*, Springer Verlag, 1999.

[35] Fox, R.W. and McDonald, A.T. *Introduction of Fluid Dynamics*, fourth edition, John Wiley and Sons, New York, 1992.

[36] Frey, P.J. and George, P.L. *Mesh Generation: application to finite element*, HERMES Science, Oxford, 2000.

[37] Fyfe, D.E., Oran, E.S. and Fritts, M.J. *Numerical simulation of droplet oscillation, breakup and distortion*, Technical Report 87-0539, AIAA, 1987.

[38] Fyfe, D.E., Oran, E.S. and Fritts, M.J. *Surface tension and viscosity with Lagrangian hydrodynamics on a triangular mesh*, J. Comp. Phys. Vol. 76, pp 349-384, 1987.

[39] Gerrard, J.J. *The mechanics of the formation region of vortices behind bluff bodies*, J. Fluid Mech., Vol. 190, pp 265-298, 1974.

[40] Gerritsma, M.I. and Phillips, T.N. *Spectral element methods for axisymmetric Stokes problems*, J. Comp. Phy., Vol. 164, pp 81-103, 2000.

[41] Givi, P. *Spectral and random vertex method in turbulent reactig flows*, 8, pp 475-573, Turbulent Reactive Flows, Academic Press, 1994.

[42] Glowinski,R., Pan T.W., Hesla, T.I. and Joseph, D.D. *A distributed Lagrangian multiplier/fictitious domain method for particulateflows*, Int. J. Multiphase Flow, Vol. 25, pp 755-704, 1999.

[43] Gordon, W.J. and Hall, C.A. *Constructions od curvilinear coordinate systems and application to mesh generation*, Int. J. Numer. Methods Engrg, Vol. 7 pp 461-477, 1973.

[44] Gordon W.J., and Thiel, L.C. *Transfinite mappings and their application to grid generation*, In J. F. Thompson, editor, Numerical Grid Generation, pp 171-192, Amsterdam, 1982.

[45] Harlow, F.H. and Welch, J.E. *Numerical calculation of time-dependent viscous incompressible flow of fluid with free surface*, Phys. Fluids, Vol. 8, pp 2182-2189, 1965.

[46] Helenbrook, B.T. *A two-fluid spectral-element method*, Comput. Meth. Appl. Mech. Engrg., Vol. 191, pp 273-294, 2001.

[47] Helenbrook, B.T. and Edwards, C.F. *A two-fluid spctral element method with application to drops*, Eighth International Conference on Liquid Atomisation and Spray Systerms, Pasadena, CA, USA, July 2000.

[48] Patera, A.T. *Finite element approximation of the non-stationary Navier-Stokes problem. Part 2: Stability of solutions and error estimates uniform in time*, SIAM J. Numer. Anal., Vol. 23, pp 750-777, 1986.

[49] Hirt, C.W. and Nichols, B.D. *Volume of fluid (VOF) method for the dynamics of free boundaries*, J. Comp. Phys., Vol. 39, pp 201-205 1981.

[50] Hirt, C.W., Amsden, A.A. and Cook, J.L. *An arbitrary Langrange-Eulerian computing method for all flow speeds*, J. Comp. Phys., Vol. 14, pp 227-253 1974.

[51] Ho, L.W. and Patera, A.T. *A Legendre spectral element method for simulation of unsteady incompressible viscous free-surface flows*, Comput. Meth. Appl. Mech. Engrg., Vol. 80, pp 355-366, 1990.

[52] Ho, L.W. and Patera, A.T. *Variational formulation of three-dimensional viscous free-surface flows: Natural imposition of surface tension boundary conditions*, Int. J. Numer. Meth. Fluids,, Vol. 13, pp 691-698, 1991.

[53] Hu, H.H. *Direct simulation of flows of solid-liquid mixture*, Int. J. Multiphase Flow, Vol. 22, pp 335-352 1996.

[54] Hu, H.H., Joseph, D.D. and Crochet, M.J. *Direct simulation of fluid particle motions*, Theor. Comput. Fluid Dyn., Vol. 3, pp 285-306 1992.

[55] Hu, H.H., Patankar, N.A. and Zhu, M.Y. *Direct numerical simulation using the arbitrary Lagrangian-Eulerian technique*, J. Comp. Phys., Vol. 169, pp 427-462 2001.

[56] Huang, L.L., and Riggs, H.R. *Development of a new interfacing strategy for fluid-structure interaction*, Proceedings of Institution of Mechanical Engineers, part M: Journal of Engineering for Maritime Environment, vol. 219, No. 3, pp 131-148, 2005.

[57] Ishii, M. *Thermal fluid dynamic theory of two-phase flow*, Paris, 1975

[58] Joseph, D.D., Belanger, J. and Beavers, G.S. *Breakup of a liquid drop suddenly exposed to high-speed air stream*, Int. J. Multiphase flow, Vol. 25, pp 1263-1303, 1999.

[59] Johnson, T.A. *Numerical and experimental investigation of flow past a sphere up to Reynolds number of 300*, PhD Thesis, University of Iowa, 1996.

[60] Johnson, T.A. and Patel, V.C. *Flow past a sphere upto Reynolds number of 300*, J. Fluid Mech., Vol. 378, pp 19-70, 1999.

[61] Jones, A. and Thomas, G.O. *The action of water sprays on fires and explosion*, Trans. IChemE, Vol. 71, part B, 1993.

[62] Karniadakis, G.E. and Sherwin S.J. *Spectral/hp element methods for CFD*, Oxford University Press, 1999.

[63] Korczak, K.Z. and Patera, A.T. *Isoparametric spectral elemetm method for solution of the Navier-Stokes equations in complex geometry*, J. Comp. Phys., Vol. 62, pp 361-382, 1986.

[64] Liang, P.Y., Eastes, T.W. and Gharakhari, A. *Computer simulation of drop deformation and drop breakup*, Technical Report88 3142, AIAA, 1988.

[65] Luo, K.H. *Combustion effects on turbulence in a partially premixed supersonic diffusion flame*, Combustion and Flame, Vol. 119, pp 417-445, 1999.

[66] Maday, Y. and Patera A.T. *Spectral element methods for Navier-Stokes equations*, in A.K. Noor and J.T. Oden, editors, State-of-the-Art Serveys in Computational Mechanics, chapter 3, ASME, 1989.

[67] Magarvey, R.H. and Bishop, R.L. *Transition ranges from three dimensional wakes*, Cac. J. Phy., Vol. 39, pp 1418-1422, 1961.

[68] Maxworthy, T. *Experimental studies in megneto-fluid dynamics: flow over a sphere with a cylindrical afterbody*, J. Fluid Mech., Vol. 35, pp 411-416, 1969.

[69] Morris, D.W. *Temporal characterisation of various G-DI fuel injector concepts*, PhD Thesis, Cardiff University, UK, 2003.

[70] Natarajan, R. and Acrivos, A. *The instability of the steady flow past spheres and disks*, J. Fluid Mech., Vol. 254, pp 323-344, 1993.

[71] Norton, C.M. *An experimental study of droplet combustion at high pressures*, MSc Thesis, University of Tennessee Space Institute, Tullahoma, USA, 1990.

[72] Noh, W.F. *A time-dependent two-space dimensional coupled Eulerian-Lagrangian code*, in B. Adler, S. Fernbach and M. Rotenberg, editors, *Methods in Computational Physics 3*, Academic Press, New York, 1964.

[73] Oden, J.T. *Optimal hp-finite element methods*, Technical Report, TICOM Report 92-09, University of Texas at Austin, 1992.

[74] Owens, R.G. *A new microstructure-based constitutive model for human blood*, J. Non-Newtonian Fluid Mech., Vol. 140, Issue 1-3 pp 57-70, 2006.

[75] Owens, R.G. and Phillips, T.N. *Computational Rheology*, Imperial College Press, London, 2002.

[76] Patera, A.T. *A spctral method for fluid dynamics: Laminar flow in channel expansion*, J. Comp. Phy., Vol. 54, p468, 1984.

[77] Phillips, R.M. *Spectral element methods for simulating the flow past a confined cylinder*, MPhil Thesis, University of Wales, Aberystwyth, 2001.

[78] Phillips, T.N. and Roberts, G.W. *The treatment of spurious pressure modes in spectral impressible flow calculation*, J. Comp. Phy., Vol. 105, pp 150-164, 1993.

[79] Pilch, M. and Erdman, C.A. *Use of breakup time data and velocity history data to predict the maximum size of stable fragments for acceleration-induced breakup of a liquid drop*, Int. J. Multiphase Flow, Vol. 13, pp 741-757, 1987.

[80] Prippacher, H.R., Le. Clair, B.P. and Hamiliec, A.E. *Some relations between drag and flow pattern of viscous flow past a sphere and a cylinder at low and intermediate Reynolds numbers* , J. Fluid Mech., Vol. 44, p781, 1970.

[81] Reading, R.J. *Flow past a sphere in an elastic liquid*, PhD Thesis, University of Wales, Aberystwyth, 1995.

[82] Roache, P.J. *Computational Fluid Dynamics*, Hermosa Publishers, 1982.

[83] Ronquist, E.M. *Convection treatment using spectral elements of different order*, Int. J. Num. Meth. Fluids, 1996.

[84] Roos, F.W. and Willmarth, W.W. *Some experimental results on sphere and disk drag*, AIAA J., Vol. 9, pp 285-291, 1971.

[85] Sankar, D.S. and Hemalatha, K. *A non-Newtonian fluid model for blood flow through a catheterized artery–Steady flow*, Applied Mathematical Modelling, vol. 31, Issue 9, pp 1847-1864, 2007.

[86] Schlichting, H. *Boundary-Layer Theory*, seventh edition, McGraw-Hill, New York, 1979.

[87] Schneidesch C.R. and Deville, M.O. *Chebyshev collocation method and multidomain decomposition for Navier-Stokes equations in complex curved geometries*, J. Comp. Phy., Vol. 106, pp 234-257, 1993.

[88] Schumack, M.R., Schults, W.W. and Boyd, J.P. *Spectral method solution of the Stokes equations on non-staggered grids*, J. Comp. Phy., Vol. 94, pp 30-58, 1991.

[89] Shraiber, A.A., Podvysotsky, A.M. and Dubrovsky, V.V. *Deformation and breakup of drops by aerodynamic forces*, Atomization and Spray, Vol. 6, pp 667-692, 1996.

[90] Shyy, W., Udaykumar, H.S., Rao, M.M. and Smith, R.W. *Computational Fluid Dynamics with Moving Boundaries*, Taylor and Francis, 1996.

[91] Szabo, B. and Babuska, I. *Finite Element Analysis*, John Wiley and Sons, 1991.

[92] Succi, S. *The Lattice Boltzmann Equation*, Oxford University Press, Oxford, 2001.

[93] Achenbach, E. *Experimental investigation of the wake behind a sphere at low Reynolds numbers*, J. Phy. Soc., Japan, Vol. 11, pp 1104-1108, 1974.

[94] Tomboulides, A.G. *Direct and large eddy simulation of wake flows: flow past a sphere*, PhD Thesis, Princeton University, 1993.

[95] Tomboulides, A.G., Orszag, S.A. and Karniadakis, G.E. *Direct and large eddy simulation of axisymmetric wakes*, AIAA paper 93-0546, 1993.

[96] Vicelli, J.A. *A method for including arbitrary external boundaries in the MAC incompressible fluid computing technique*, J. Comp. Phys., pp 543-551, 1969.

[97] Vicelli, Hoppe *Higher order polynomial elements with isoparametric mapping*, Int. J. Numer. Meth. Engrg., Vol. 15, pp 1747-1769, 1980.

[98] Wannaborworn, S., Mackley, M.R. and Renardy, Y. *Experimenal observation and watching numerical simulation for the deformation and dreakup of immiscible drops in oscillatory shear*, J. Rheol, Vol. 46, pp 1279-1293, 2002.

[99] Wu, H.C., Hwang, W.S. and Lin, H.J. *Development of a three-dimensional simulation system for micro-inkjet and its experimental verification*, Material Science and Engineering, Vol. A373, pp 268-278, 2004.